UNIVERSITEIT VAN PRETORIA
UNIVERSITY OF PRETORIA
YUNIBESITHI YA PRETORIA

Failure Assessment of Boiler Tubes under Localized External Erosion to Support Maintenance Decisions

By

Ifeanyi Emmanuel Kalu

A THESIS SUBMITTED IN PARTIAL FULFILMENT OF THE REQUIREMENTS FOR THE DEGREE

Philosophiae Doctor in Mechanics

TO THE FACULTY OF ENGINEERING, BUILT ENVIRONMENT AND
INFORMATION TECHNOLOGY,
UNIVERSITY OF PRETORIA

February 2020

Abstract

Title : Failure Assessment of Boiler Tubes under Localized External Erosion to Support Maintenance Decisions

Author : Ifeanyi Emmanuel Kalu

Supervisors : Dr. Helen M. Inglis and Prof. Schalk Kok

Department : Mechanical and Aeronautical Engineering

Degree : Philosophiae Doctor (Mechanics)

Boiler tubes used in power plants and manufacturing industries are susceptible to numerous failures due to the harsh environment in which they operate, usually involving high temperature, pressure and erosive-corrosive environment. Among the wide range of failures associated with the tubes, localized external erosion is prevalent. In spite of efforts made over the years to solve this problem, localized erosion of boiler tubes continues to be a leading cause of tube leakages and unscheduled boiler outages in power plants and other utilities. There is, therefore, a need to approach this problem systematically and engage in rigorous studies that will allow improved management of this persistent problem.

In this thesis, comprehensive studies were first carried out on modelled variants of localized external eroded boiler tubes with conceptualized flaw geometries, such as could be seen in real situations. The outcome of these investigations provided insights into the factors that influence the failure of these tubes while in use. The stress concentration, plasticity and flaw geometry all play critical roles in influencing the failure of tubes. Also, the failure pressures of the modelled tubes were analyzed in relation with several other failure criteria, to determine which failure criteria will be most suitable for the failure assessment of the localized tubes. Based on the result of the analysis, plastic strain in the range 5%-7% is recommended as a compromise between the extreme benchmark failure criterion of 20%, and the overly conservative 2%.

The insights gained from the studies carried out on conceptualized variants of localized thinned tubes were extended to real localized external eroded tubes obtained from the industry and used to develop an improved and efficient failure assessment methodology framework for heat resistant seamless tubes while in service. This was done by treating the tubes as an inverse problem and using an optimization technique to obtain the flaw geometric properties of the tubes so as to effectively replicate them on the conceptualized geometries. Using two Material Properties Council (MPC) models generated based on the properties of the tubes as a function of their operating temperatures, comprehensive nonlinear finite element analyses (NLFEA) were conducted on the 160 finite element models. These tubes were assessed based on the maximum equivalent plastic strain and Von Mises stress produced at the deepest point of the flaw area within each of the tubes when subjected to their respective operating pressures at which they failed. The failure assessment outcome revealed that most of the heat resistant tubes while in service will remain intact and not fail if their remaining tube thicknesses were within (0.7 t_{min} to t_{min}), where t_{min} is the minimum remaining thickness of the tube based on allowable stress. In addition, a 5% plastic strain ($P_{5\%}$) and equivalent Von Mises stress criteria of 0.8 σ_{uts} were deduced as failure criteria to guard against the failure of these tubes while in service, and also avoid their early replacement. The developed methodology framework was checked and compared with the API-ASME FFS standard and found to be in good agreement with it, also more efficient and with reduced conservatism.

Finally, sensitive studies were conducted based on the developed methodology to examine how the combination of the flaw geometry and material factors could possibly influence the failure of the tubes while in use. The study outcome shows that there were no appreciable changes in the normalized Von-Mises stress ratios and the plastic strain response for the normalized remaining thickness of the tubes. The proposed $P_{5\%}$ and 0.8 σ_{uts} limits accurately predicted the failure for all the tubes and were reasonably safe limit for the tubes. Insights gained from the strain hardenability of the tubes studied will also provide guidance with taking proactive measures for the maintenance of the tubes.

In summary, all the insights gained from this research and the developed failure assessment methodology framework will be helpful in categorizing the severity of localized external erosion on tubes while in use, and also support maintenance decisions on these critical assets.

Keywords: Boiler tubes, localized external erosion, plastic deformation, stress concentration, flaw geometry, failure criteria, plastic strain, conceptualized finite element models, nonlinear finite-element analysis, equivalent Von Mises stress, API-ASME FFS Standard.

Dedication

To the Almighty God, who gave me life, wisdom and sustained me through this journey of contributing knowledge to the benefit of humanity.

In loving memory of my late mother, Ada Uduma Kalu, who sadly passed away during the course of my studies on the 25th day of February 2017.

Acknowledgements

I am foremost very grateful to God for seeing me through the ups and downs of this PhD journey and also granting me grace to successfully pull through to the end.

I would like to sincerely appreciate the Department of Research and Innovation (DRI), University of Pretoria for funding my PhD program through the UP Commonwealth Scholarship. I am really honored to have been one of your prestigious scholars.

My deepest appreciation goes to my highly esteemed supervisors, Dr. Helen M. Inglis and Prof. Schalk Kok, for their deep commitment to me and this research, as well as the technical and moral support, guidance, and insight they offered during the course of this program. I am also grateful for all the review sessions I had with them, they were very enlightening and inspiring. Thank you so much for your great mentorship during the course of this study and in my academic career.

I want to equally appreciate Prof. Stephan Heyns, the Director of the Centre for Asset Integrity Management (C-AIM) in the Department of Mechanical and Aeronautical Engineering, University of Pretoria, for all the support and other assistance he provided during the course of this research. I am also indeed grateful to Ms. Bonolo Mokola, the Centre's administrative staff member, for being so efficient with her duties, who graciously assisted me with all the office things and other support I needed during my program.

My special thanks also goes to Prof. Nico Wilke, Dr. Stephan Schmidt and Isaac Setshedi, who at different times in the course of this program motivated and encouraged me to keep pressing forward.

I will not fail to appreciate Dr. Jannie Pretorius, who was always there to offer any technical assistance with ANSYS licenses and the server. He was of a tremendous support to me and I am indeed grateful to him. Likewise, I also appreciate QFINSOFT Support Team, for helping to resolve some of the issues I had with my simulations.

My profound thanks goes to the DG, Directors and all the entire staff of the Sheda Science and Technology Complex (SHESTCO), Abuja, Nigeria for granting me the leave of absence to undertake this program. In the same vein, I would like to further extend my sincere gratitude to Engr. Dr. (Mrs.) Edith Ishidi, Gabriel Oyerinde, and Atinuke Ominisi, for their support and kind assistance at various times during my studies.

I will like to wholeheartedly appreciate all my post graduate colleagues and friends, who were my support system, providing encouragement and assistance to me at different times during the course of this program; Andre Van der Walt, Femi Olatunji, Ernest Ejeh, Samson Aasa, Gareth Howard, Bright Edward, Craig Nitzsche, Martin Ekeh, Amanda Momoza, Joachim Gidiagba, Tosin Igbayiloye, Aiki Istiphanus, Dele Bayode, Emmanuel Nwosu, Steve Essi, Uche Ahiwe, Emeka Esomonu, Oluchukwu Ulasi, Chioma Okeke, Titilayo Mewojuaye, Ibukun Adetula, Stephen Adegbile, Jude Ahana, Chinonso Nwanevu, Joy Uba, Naomie Kabimba, Justice Medzani, Josiah Taru, Chinenye Okoro, Femi Ajiboye, Dr. Tunde Oloruntoba, Dr. Adedapo and Dr.(Mrs.) Adejoke Adeyinka, Dr. Obioma Emereole, Dr. Henry and Mrs Esther Ekeh, Dr. Akeem Bello, and Dr. Damilola Momodu.

Worth mentioning are my highly esteemed pastors and disciplers, with their families (Rev. Sunday Asokere, Pst. Martin Igboanugo, Pst Tony Olajide, Pst. Gospel Azutalam, Pst. Peter Laniya, Pst. Austen Ayo, Pst. Toye Abioye, Pst. Bode Olaonipekun, Pst. Charles Olonitola, Pst. Ezekiel Arowosafe, Pst. Thapelo Lesola, Pst. Wonder Mutuwa, Pst. Sunday Adeyemo and Uncle Gugu Zilwa) for their prayers and providing spiritual and other forms of support to me within this period.

I would also like to specially appreciate Mr. Ugochukwu Okoroafor, Mrs. Chika Nkemjika, Prof. Edwin and Dr. (Mrs.) Anne Ijeoma, Prof. Wole and Mrs. Morenike Soboyejo, Mr. Chinedum and Mrs. Irene Isiguzo for the key roles they have played in my life, especially during the time of my study. I deeply treasure them for their love and care.

My final appreciation goes to my Aunties, Uncles, and beloved sister (Ugo Grace Kalu) who have been there for me at all times. I am immensely grateful to them all.

Table of Contents

List of Figures

List of Tables

Nomenclature

a	Horizontal Dimension of the Elliptical Surface
b	Vertical Dimension of Elliptical Surface
API	The American Petroleum Institute
ASME	The American Society of Mechanical Engineers
ASTM	ASTM International Standard
BS	British Standard
DIN	Deutsches Institut Fur Normung (The German Institute for Standardization)
EN	European Standard
CAE	Computer-Aided Engineering
D_o	Outer Diameter of the Tube [mm]
E	Elastic Modulus [GPa]
E_o	Elongation in Percentage [%]
EPFEA	Elastic Plastic Finite Element Analysis
f_l	Flaw Length [mm]
f_w	Flaw Width [mm]
f_d	Flaw Width [mm]
H	Plane Height from the Centre Line of the Tube [mm]
FEA	Finite Element Analysis
FFS	Fitness-for-Service
GTA	Groove-like Local Thin Area
l	Length of the Tube [mm]
LRFD	Load and Resistance Factor Design
LTA	Local Thin Area
m_2	Strain Hardening Exponent

$M_{5\%}$	5% Plastic Strain Hardening Model
$M_{20\%}$	20% Plastic Strain Hardening Model
$MAWP$	Maximum Allowable Working Pressure of the Flawed Component [MPa]
$MAWP_o$	Maximum Allowable Working Pressure of the Unflawed Component [MPa]
MPC	The Materials Research Council
$MSUTS$	Minimum Specific Ultimate Tensile Strength [MPa]
$MSYS$	Minimum Specific Yield Strength [MPa]
NLFEA	Nonlinear Finite Element Analysis
P	Operating Pressure [MPa]
P_a	Applied Internal Pressure [MPa]
P_{pc}	Plastic Collapse Pressure [MPa]
P_{max}	Internal Maximum Allowable Working Pressure [MPa]
$P_{2\%}$	2% Plastic Strain
$P_{5\%}$	5% Plastic Strain
$P_{7.5\%}$	7.5% Plastic Strain
$P_{10\%}$	10% Plastic Strain
$P_{15\%}$	15% Plastic Strain
$P_{20\%}$	20% Plastic Strain
$PP_{5\%}$	Pressure at 5% Plastic Strain
R	Radius of the Cutting Plane from the Plane Axis [mm]
R_o	Ratio of the Minimum Yield Strength to Tensile Strength (i.e. σ_y/σ_{uts})
RA	Reduction in Area in Percentage [%]
RTA	Round Local Thin Area
r_i	Inner Radius of the Tube [mm]
r_o	Outer Radius of the Tube [mm]
RSF	Remaining Strength Factor

RSF_a	Allowable Remaining Strength Factor
SCF	Elastic Stress Concentration Factor
t	Thickness of the Tube [mm]
t_{min}	Minimum remaining thickness of the tube based on allowable stress [mm]
t_{rem}	Tube Remaining Thickness Ratio (t_r/t)
t_r	Remaining Thickness of the Tube [mm]
T	Temperature [℃]
T_{rt}	Temperature at Room Temperature [℃]
T_{ot}	Temperature at Operating Temperature (℃)
z	Offset Height from the Centre Line of the Tube [mm]

Greek Letters

α	Coefficient of Thermal Expansion [$℃^{-1}$]
α_{mf}	Material Factor for Multiaxial Strain Limit
β	Load Factor Coefficient
ε	Engineering Strain
ε_{cf}	Forming Strain
ε_{lt}	Limiting Triaxial Strain,
ε_{ps}	Total Equivalent Plastic Strain
ε_t	True Strain
$\varepsilon_{t,uts}$	True Ultimate Tensile Strain
ε_u	Uniaxial Strain Limit
θ	Angular Difference
λ	Ratio of Ultimate Tensile Strength to Yield Strength (i.e. σ_{uts}/σ_y)
v	Poisson’s Ratio
ρ	Density [Kgm^{-3}]

σ	Engineering Stress [MPa]
$\sigma_1, \sigma_{2,} \sigma_3$	Maximum, Median and Minimum Principal Stresses
σ_a	Allowable Stress [MPa]
σ_e	Equivalent Von Mises Stress
σ_f	Flow Strength [MPa]
σ_{uts}	Ultimate Tensile Stress/Strength or Tensile Strength [MPa]
σ_y	Yield Strength [MPa]
σ_t	True Stress
$\sigma_{t,uts}$	True Ultimate Tensile Stress/Strength [MPa]
σ_{uts}^{rt}	*MSUTS* value at Room Temperature [MPa]
σ_y^{rt}	*MSYS* value at Room Temperature [MPa]
$\sigma_{uts}^{T_{min}}$	Specified σ_{uts} value at the Minimum Temperature Limit [MPa]
$\sigma_y^{T_{min}}$	Specified σ_y value at the Minimum Temperature Limit [MPa]

Articles from this Thesis

Published full-length conference papers

1 **I.E. Kalu**, H. Inglis, S. Kok, **Non-Linear Finite Element Analysis of Boiler Tubes under Localized Thinning Caused by Wall Loss Mechanisms** (2018), *Proceedings of the 11th South African Conference on Computational and Applied Mechanics (SACAM), Paper no. 2121, pp. 280–290, Vanderbijlpark, South Africa, 17–19 September 2018. ISBN: 978-1-77012-143-0.*

2 **I.E. Kalu**, H.M. Inglis, S. Kok, **Effect of Defect Geometry of Localized External Erosion on Failure of Boiler Tubes** (2018), *Proceedings of the ASME Pressure Vessels and Piping Conference (Proc. ASME.51630); Volume 3B: Design and Analysis, Paper no. PVP2018-84787, pp. V03BT03A037 (9 pages), Prague, Czech Republic 15–20 July 2018. ISBN: 978-0-7918-5163-0.*

Publications in peer-reviewed/refereed journals

1. **Ifeanyi Emmanuel Kalu**, Helen Mary Inglis, Schalk Kok (2020). **Failure Assessment Methodology For Boiler Tubes With Localized Erosion Defects,** *International Journal of Pressure Vessels and Piping*. *(Submitted* - IPVP-D-20-00031*).*
2. **Ifeanyi Emmanuel Kalu**, Helen Mary Inglis, Schalk Kok (2020). **Failure Analysis of Boiler Tubes with Elliptical Localized Erosion Flaws,** *Engineering Failure Analysis (Submitted* - EFA_2020_218).
3. **Ifeanyi Emmanuel Kalu**, Helen Mary Inglis, Schalk Kok (2020). **Sensitivity study on developed failure assessment methodology for boiler tubes with localized erosion defects,** *International Journal of Pressure Vessels and Piping*. *(To be submitted).*

1 INTRODUCTION

1.1 Background and Motivation

Boiler tubes are long cylindrical metallic vessels that are vital components in boilers used for steam production in power plants and process industries. The steam produced is usually delivered to a turbine for electric power generation in power plants, or used to run machinery, in the manufacturing or process industries. There are two main types of boilers where these tubes are used, which are the water tube boilers and fire tube boilers. The boilers usually have combustion chambers, where fossil fuels are burnt to produce hot gases, which are then released to heat up water contained in the boilers. In the case of the water tube boiler, the tubes convey the boiler water through the hot gases and in the process convert the water into high pressure superheated steam at the point of their discharge from the boiler. For the fire tube boiler, the tubes convey the hot gases from the combustion chamber through the boiler, while being submerged within the boiler water and in the process transfer the heat from the hot gases into the water before they exit the boiler [1,2]. Figure 1.1 shows a typical water tube boiler and Figure 1.2 shows the schematic set-up of a coal fired power plant demonstrating where the boiler tubes are used within the plant.

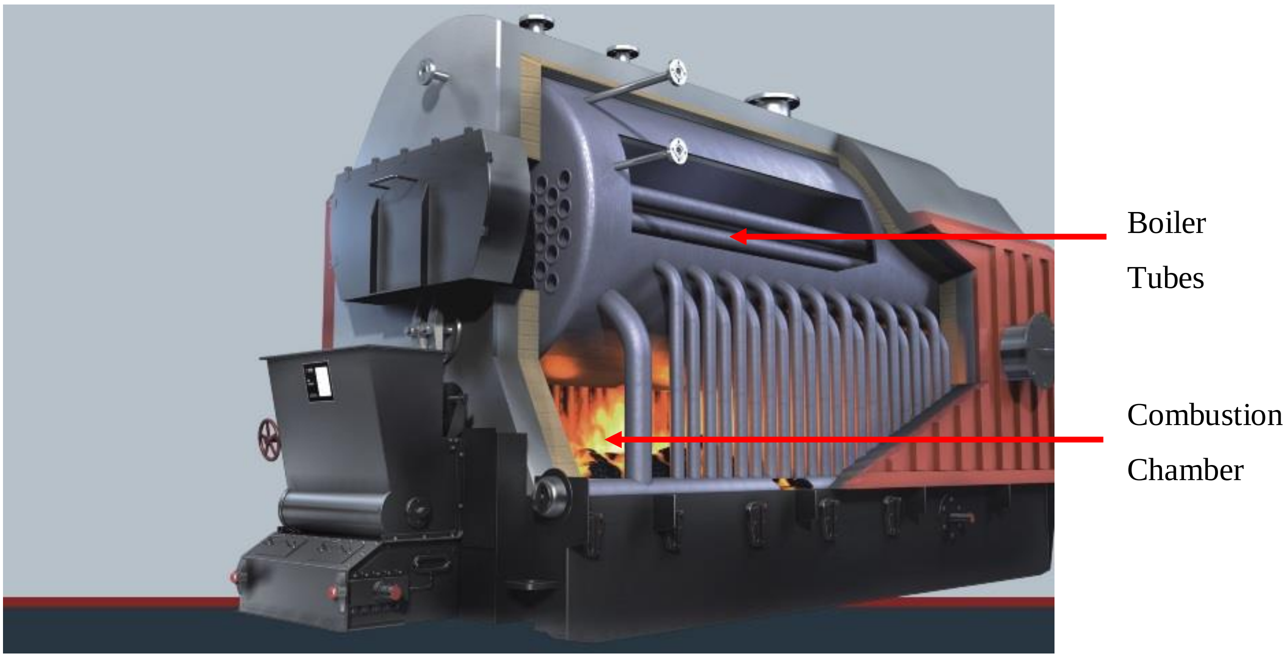

Figure 1.1: A typical water tube boiler [3]

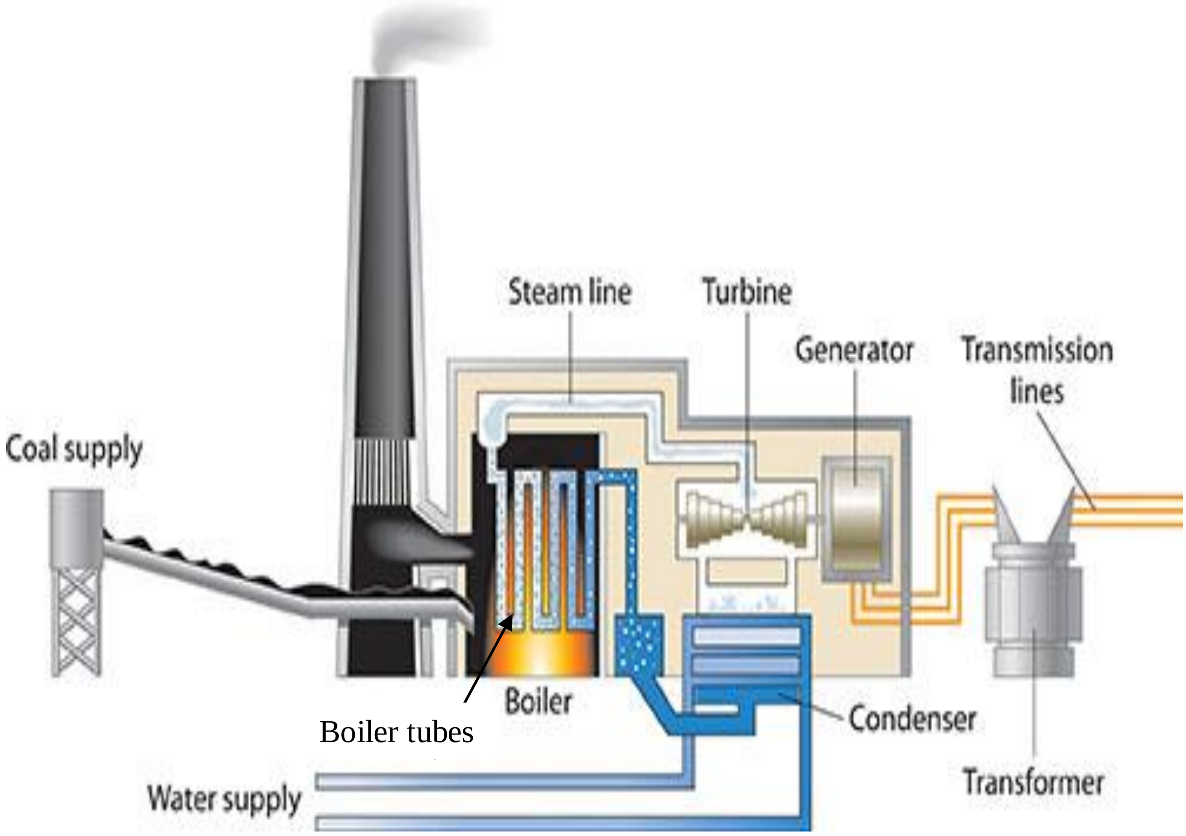

Figure 1.2: Schematic set-up of a coal-fired power plant [4].

Due to the complex conditions in which boiler tubes operate, which involve high temperature, pressure and erosive-corrosive environments, these tubes experience a wide variety of failures involving one or more mechanisms while in service, leading to formation of cracks, pits or gouges, and the bulging, thinning, deformation and eventual bursting of the tube [5–12]. Occurrence of these tube failures have been reported to be one of the major causes of availability loss in boilers [7,13–15] and also the leading cause of unscheduled or forced boiler outages in power plants and manufacturing industries, resulting in loss of production and costly emergency repairs [8–11,15–19]. The cost due to electricity power loss as a result of boiler tube failures leading to unplanned outages exceeds billions of dollars annually [11]. This presents a critical need for more focused attention to be given to these failure problems so as to improve the profitability of these industries

Over the years, localized external erosion, a form of localized thinning or metal loss, has been one of the most common tube failures in the power plant industry [6–9,12–16]. The Electric Power Research Institute report states that approximately 25% of all tube failures in fossil fuel-fired boilers are caused by fly ash erosion [20], making this failure mechanism a matter of serious concern. As a result of localized external erosion, the tube undergoes a significant localized reduction in its wall thickness, becomes susceptible to gross plastic deformation, and ultimately ruptures. This type of failure is driven by wall loss mechanisms, occurring when the tube surfaces are subjected to steady impact by abrasive components from the boiler's combustion chamber (commonly fly ash, coal particles, and falling slag) or as a result of a misaligned soot blower misdirecting a high-velocity jet of air saturated with condensed water droplets or steam to directly impinge on the surfaces of the tube [7–9,19,21–23]. Localized erosion could also occur as a result of steam cutting from neighbouring tubes, i.e., when a failed tube ruptures and steam flows out with a high momentum to impinge on adjacent tubes, which causes those tubes to fail [11,19,23]. Figure 1.3 shows an example of a boiler tube which has failed due to localized external erosion.

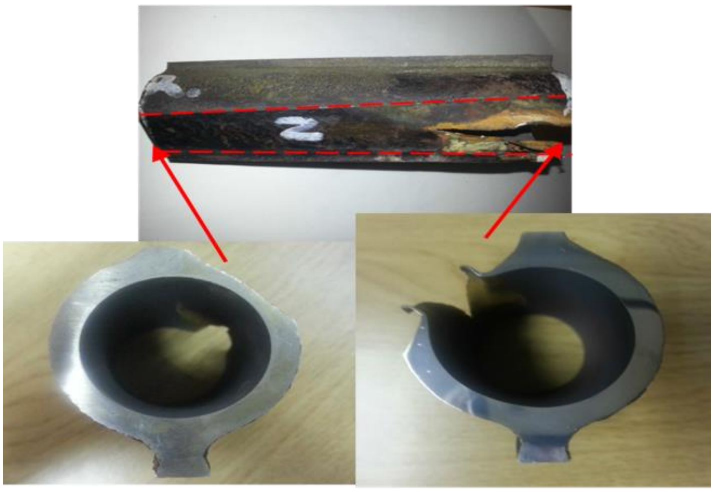

Figure 1.3: Soot blower erosion of boiler tubes showing localized thinning [24].

Through the years, failure assessment of boiler tubes have focused primarily on metallurgical failure investigations and root cause analyses, involving tube visual examinations, wall thickness measurements, chemical composition and microstructural analyses using scanning electron microscope (SEM), x-ray diffraction (XRD), etc., to find the cause of failure by identifying the failure mechanisms involved and, in a few cases, also provide suggestions for preventive measures [1,5–9,17,25–30]. Efforts have been made to predict the tube remaining life [12,16,27,31,32], provide certain guidelines to control characteristics of the erosive particles (type, size, shape, flow rates) and propose the use of flow control screens to redistribute the erosive particles, reduce gas velocities and subsequently lower the erosion rates [13,18,20,22,23]. These have all helped to provide some relief, but still the problem of localized erosion of boiler tubes continues to be the leading cause of tube leakages and unscheduled boiler outages, in power plants and other utilities [6–9,13–16,20].

In the last two decades, the American Petroleum Institute (API) and the American Society of Mechanical Engineers (ASME) have made efforts to develop a standard document to provide guidance towards conducting quantitative engineering assessments of pressurized vessels and their components, containing damage or a flaw while in use [33–35]. These efforts have also not been without challenges, which have been outlined in this thesis in Section 2.2.5. These include: the assessments requiring a detailed inspection and many input details; cumbersome finite element analysis (FEA) simulation required for the highest level of assessment, which could only be considered reasonable for severe flaw assessment; and also the concept of factored loads that possibly may lead to replacing tubes that could still be safe for continued operation.

Based on all the aforementioned, there is, therefore, a need for more detailed research to be carried out to develop improved and efficient solutions to this prevalent issue in the industry.

1.2 Challenges with Detecting Tube Leakages in the Industry

When a tube has leaked, the boiler is shut down and a forced cooling of the boiler is carried out using a forced draft fan at a safe rate, after which the boiler is tested to ensure there are no dangerous gas within it. When this has been ascertained, the inspection team gets into the boiler to try to locate the flawed tube. Since a typical boiler contains hundreds of tubes stacked upwards to heights as far as 30 meters, the location of the damaged area could be inaccessible, hence, a scaffold will have to be built to ensure a safe access to it. Upon inspection of the tubes to identify the flawed tube(s), a failure assessment team gets into the boiler to carry out an investigation to determine the root cause of the flaw and its failure mechanism. Inspectors also carry out ultrasonic thickness measurement on all tubes to determine which tubes have experienced external erosion and should be either repaired or replaced. The maintenance team will then commence fixing the tubes once the scope of work has been finalized. In some cases, the location of the affected tubes may not be directly accessible and as such, the surrounding good tubes will have to be cut out in order to gain access to them. Once the tubes have been fixed, the cut out tubes are rewelded and each weld is x-rayed and certified to be defect free.

This whole process could take can up to 60 hours and more, leading to production and consequent financial loss for the industry. Beyond this, there are challenges of erecting scaffolds to access the tubes and availability of skilled engineers onsite to measure all suspected flawed tubes and prioritize their replacement or repairs, with regards to if they will survive the next shut down or not. In order to ameliorate the rigors involved in this whole process, there will be a need to have a rapid decision-making tool to help to prioritize the maintenance, repair or replacement of these tubes while in service.

1.3 Research Objectives

During a forced shut down due to tube leakages or routine maintenance activities, in an ideal scenario (i.e., with unlimited time and budget), all flawed tubes would be repaired or replaced. But, with limited time during the shutdown, it is usually not possible to repair all flawed tubes. Further, in a constrained economic environment and with ageing infrastructure, it is not financially wise to replace flawed tubes that could still be safe for continued operation. On the other hand, if critically flawed tubes are not repaired or replaced, it could lead to unexpected failures, loss of production, costly emergency repairs, and consequently forced or unplanned outages. In essence, the tubes that have to be repaired or replaced in order to last till the next shut down are prioritized ahead of the tubes that are flawed but which will be able to last till the next scheduled shutdown. Hence, there is a need to find a prognostic solution to this predicament, through the development of a rapid decision-making tool, supported by rigorous research.

Comprehensive investigations are needed to determine which factors are responsible for gross plastic deformation of eroded tubes. Investigations will be carried out on real examples of failed tubes obtained from the power plant in order to develop a failure assessment methodology that can guide in categorizing the severity of the localized external erosion on the tubes. Based on extensive nonlinear finite element analysis (NLFEA) of flawed tubes, a simplified assessment criterion should be defined, which will allow non-expert users to make quick and accurate decisions. This framework will help support the maintenance decisions on these critical assets during their service time.

The specific objectives this research seeks to achieve are as follows:

1 To model conceptualized variants of real localized thinned flawed tubes that could possibly occur in practical scenarios and then carry out comprehensive investigations through a series of nonlinear finite element analyses (NLFEA) on the models to determine the factors that influence the failure of the tubes under localized thinning.

2 To conduct a detailed assessment on the strength and physical properties of commonly used heat resistant tubes while in operation (under high temperature and pressure environment) and then generate realistic material models that account for temperature, which can easily be used in scenarios of limited material data.

3 To develop a new, easy-to-use, less expensive and efficient fitness-for-service framework for tubes under localized external erosion based on the outcome of studies 1 and 2, while using real localized thinned tubes as case studies. This framework is to include a methodology and failure criteria that will guide in categorizing the severity of the flawed tubes while in service. This developed methodology is to be checked and compared with the API-ASME fitness-for-service (FFS) standard.

4 The sensitivity of the developed framework with regards to the flaw geometry and tube materials is to be investigated.

1.4 Scope of the Research

This is a Computer-Aided Engineering (CAE) research project that involves the use of FEA commercial software tool – ANSYS® Academic Research to develop conceptualized geometric models in line with research objectives. One of the mechanical design platforms of ANSYS (DesignModeler) was used to run thousands of FEA simulations on the ANSYS mechanical analysis platform to carry out all the investigations as outlined in the research objectives.

The research also includes a thorough investigation of the material properties of the localized tubes while in operation, using real failed tubes as case studies. The outcomes from all the investigations conducted in this study (as outlined in the research objectives) are used to develop a holistic framework that fulfills the aim of this research. This is checked by comparison with existing FFS standards. Finally, the sensitivity of the developed methodology to material geometric parameters is explored.

The post processing of all the results obtained from this work, geometric plots of the conceptualized modelled flaws and the optimization technique used to extract the geometric properties of the real failed tubes so as to model them correctly, were all done using a numerical computing tool – MATLAB®.

It should be noted that this study excludes other failure problems associated with boiler tubes like creep, fracture, fatigue, etc. The intent of this research is to focus on carrying out detailed research to develop improved and efficient solutions for one major problem (plastic collapse as a result of localized external erosion) that has been a leading cause of tube leakages in fossil fuel-fired boilers. Also, there were no experimental studies done but strictly numerical studies, which were validated with real failed tubes and API-ASME FFS Standard.

1.5 Layout of the Thesis

The rest of the thesis is laid out as explained below:

Chapter 2 reviews the literature on previous studies that have been done starting from a general perspective of failure analysis of pressurized vessels and then narrowing the scope to studies on failure assessments of flawed vessels and those with localized thinned areas (LTAs). The outcome of these research studies, including the proposed failure methodologies and criteria are discussed. In particular, the outcomes from focused studies related to localize thinning in boiler tubes are discussed. The API-ASME fitness-for-service assessment guides and the challenges inherent in them are also discussed.

Chapter 3 presents the modelling of conceptualized variants of real localized thinned flawed tubes that could possibly occur in real scenarios using ANSYS®. Formulation of some geometry functions from these conceptualized models to enable the precise modelling of real localized thinned tubes and aid in their detailed failure assessment is reported. The procedure of replicating real tubes on these developed FEMs is also discussed.

Chapter 4 reports on the outcomes of the comprehensive investigations done through NLFEA on a series of conceptualized models to understand how factors - including the flaw geometry and material parameters influence the failure of the tubes. Using failure criteria from the literature and proposing additional ones, the failure pressures of the modelled tubes are analysed to deduce which criteria could be most suitable for failure assessment of these localized thinned tubes.

Chapter 5 details the realistic material models used for developing a new failure assessment methodology. The outcome of a detailed review of literature on the strength and physical properties commonly used for heat resistant tubes while in operation (under high temperature and pressure environment) is presented. Published material data for typical high temperature materials are compiled. From the outcome of the study, two distinct true stress-strain hardening material models are generated, based on the Material Properties Council (MPC) stress-strain models.

Chapter 6 presents the failure assessment on the real tubes. The outcome of the procedure employed to extract the geometric properties of the real failed tubes so as to effectively replicate them on the earlier developed models was documented. The report on the results from the NLFEA investigations and parametric studies done using these models are discussed. Also, was highlighted in this chapter, the deduced failure criteria from the outcome of the assessment, which will guard against the failure of these tubes while in service and avoid their early replacement, as well as support maintenance decisions on them. The proposed methodology was checked and compared with the API-ASME fitness-for-service (FFS) assessment standard and their outcomes are also discussed.

Chapter 7 reports on the findings of the sensitivity study carried out on the developed models with regards to the flaw geometry and tube materials. The implications from the investigations are discussed.

Chapter 8 closes with a documentation on the general summary of the thesis and the conclusions drawn from the research performed, as well as recommendations for future work.

2

LITERATURE REVIEW ON FAILURE ASSESSMENT OF LOCALIZED THINNING IN PRESSURIZED VESSELS

2.1 Introduction

The concept of localized thinning or metal-loss in pressurized vessels has drawn a lot of attention over the years due to the failure implications associated with these engineering structures. Initial studies were centered on crack growth and propagation in unstiffened cylindrical pressure vessels. Peters and Kuhn [36] in the late 1950s pioneered this research by carrying out internal pressure tests on some cylinders pressurized with air and oil, having pre-cut slits (axial through cracks) in order to examine the effect of the slit curvature and length on the hoop stress formed at the point of the cylinders bursting. From their study, they established a failure criteria to guard against the growth of these cracks in pressurized vessels.

Other early studies followed in the 1960s with authors like Folias [37,38], who studied the effects of axial cracks propagating through cylindrical shells; Duffy [39], who undertook studies on hydrostatic tests and defect behaviour in pipes; Anderson et al. [40], who applied fracture mechanics concepts to predict the burst strength of cylindrical pressure vessels through which a crack has propagated and Kihara et al. [41], who investigated brittle fracture initiation in pipes. These authors further modified the criteria Peters and Kuhn had developed for crack extension in an unstiffened cylindrical pressure vessel. Crichlow and Wells [42] also conducted some experimental tests to determine the crack propagation rate and residual strength of fatigue-cracked cylinders and Hahn et al. [43] developed three closely related criteria that could guard against crack extension in cylindrical pressure vessels containing axial cracks.

These foundational studies were the platform on which authors from the 1970s to date built to develop the various analytical methodologies and criteria that have been used in conducting failure assessment of pressurized vessels. Multiple studies have been done to enhance the structural integrity of pressure vessels such as boiler tubes, pipes and storage tanks. Of particular interest in this thesis are those protecting them against plastic collapse. The failure assessment tools from these studies will be highlighted and those centered on localized thinning will be discussed in this chapter.

2.2 Failure Assessment of Pressurized Vessels

2.2.1 Failure Assessment of Designed and Flawed Pressurized Vessels

A fundamental failure mode associated with pressurized vessels is gross plastic deformation. It occurs when a vessel experiences excessive static load, which leads to its plastic collapse, eventually making the vessel to rupture. The plastic collapse phenomenon takes place due to an overall structural instability within the vessel, such that it loses equilibrium and can no longer stay stable for a small increase in load [34,44]. To guard against the failure of pressurized vessels due to gross plastic deformation or plastic collapse, ASME [34] recommends three types of stress analyses that can be used. These are: Elastic Stress Analysis (ESA), Limit-Load Analysis (LLA) and Elastic-Plastic Stress Analysis (EPSA).

In ESA, stresses are obtained from an elastic analysis and classified into primary, secondary and peak categories, which are then limited to specified allowable values such that plastic collapse will not occur. Usually, this method gives a conservative prediction.

LLA assumes an ideal elastic-perfectly plastic material model and small (first order) deformation theory. The material exhibits linear elasticity up to the yield stress, after which small plastic strain develops followed by an unlimited plastic flow, occurring when it can no longer maintain equilibrium with the externally applied load, as shown in Figure 2.1(a). Accordingly, the limit load is therefore, the highest load that the structure can support before there is a loss or violation of equilibrium between the external and internal forces [44,45]. The allowable load that will prevent the plastic collapse of a vessel is then computed by applying a design factor to the obtained lower bound limit load [34].

However, real engineering vessels (like boiler tubes) may behave differently to the LLA model by exhibiting strain hardening and large deformations. In this situation, EPSA, incorporating an elastic-plastic material model is used to obtain a plastic collapse load on which a design factor is applied to obtain an allowable load that will prevent the onset of plastic collapse in the vessel [34]. Based on this analysis, the material exhibits linear elasticity up to yield stress, after which the stress and strain increase in a nonlinear manner supporting more loads beyond the limit load without violating the vessel equilibrium, as shown in Figure 2.1(b). The plastic load is determined as the load at which gross plastic deformation will occur within the vessel [44].

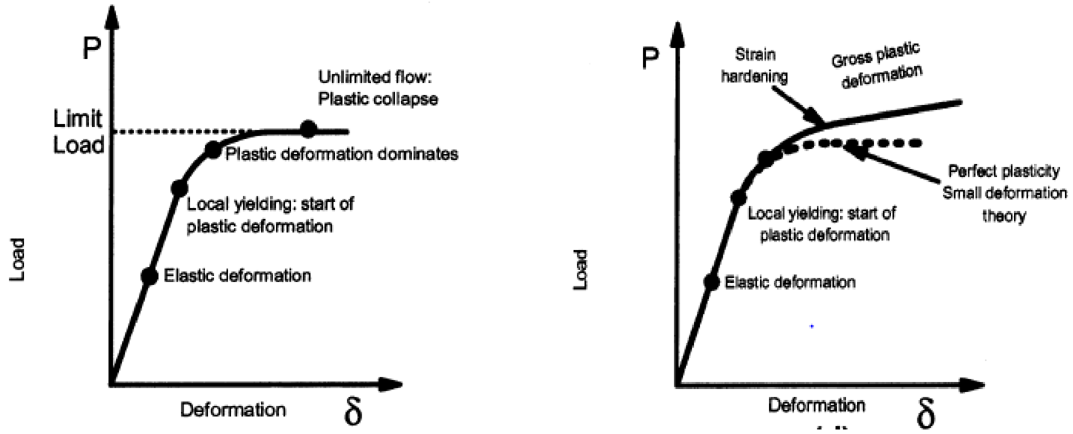

Figure 2.1: Material response for (a) Limit Load Analysis (LLA) and (b) Elastic-Plastic Stress Analysis (EPSA) [44].

Both the LLA and EPSA could be performed through a numerical analysis technique (e.g. finite element method). It is noteworthy to mention that LLA does not consider the effect of large deformations on the structure and the equilibrium analysis is based on the initial geometry of the structure. As such, EPSA will be preferable for numerical analysis of any engineering vessel since it fully incorporates deformation characteristics of the vessel.

Some analytical methods and criteria that can be found in literature have been proposed to be used to determine the limit or plastic collapse loads of engineering vessels. They include:

- 1% Plastic strain [46]
- Tangent intersection [47]
- 0.2% Offset strain [48]
- Proportional limit [48]
- Twice elastic deformation [49]
- Twice elastic slope [50]
- Plastic work [51]
- Plastic work curvature [44]

These were developed to be used in the design, fabrication, and testing of new pressurized vessels (i.e., flaw-free pressure vessels) to guard against their gross plastic deformation when subjected to static loads. But these methods and criteria do not cater for vessels that become flawed or damaged while in operation.

For failure assessment of flawed or degraded components of pressurized vessels while in-service, some standardized methods have been proposed or are recommended to be used, including: ASME B31G criterion [52], a simplified and widely used but conservative method to predict the collapse (or burst) pressure and remaining strength of the vessels; Modified ASME B31G criterion [53,54], an improved version of ASME B31G using a less conservative flow stress, bulging factor and modified defect area; RSTRENG application program [53,55], which computes the flaw area and uses the Modified ASME B31G to predict the failure pressure of the vessels; PCORR [56–58], a finite element program that uses the σ_{uts} and ductile fracture criteria to assess the integrity of the vessels; DNV-RP-F101 [59], an assessment guideline developed from a full-scale experimental test and FEA, and RPA [60], a method for assessing the residual strength of the vessels. Other criteria and models developed by some authors include: Chell limit load analysis [61], Kanninen axisymmetric shell theory model [62], Ritchie and Last corrosion flaw criterion [63]. All these methods, models and criteria were developed primarily to be used for fitness-for-service (FFS) assessment of corroded pipelines.

2.2.2 Failure Assessment of Locally Thinned Pressurized Vessels

For general cases of local metal loss, with reference mostly to internal metal loss, the following assessment methodologies and criteria have been proposed by different authors:

2% Plastic Strain and the RSF Criteria

A parametric study was conducted by Sims et al. [64] using Elastic Plastic Finite Element Analysis (EPFEA) on cylindrical and spherical shells with predominantly pressure loading and containing round local thin areas (RTAs), which were remote from structural discontinuities such as nozzles and head-to-shell junctions**.** An ideal elastic perfectly plastic model and a limit of 2% plastic strain ($P_{2\%}$) was used in this study to obtain a conservative estimate of the collapse pressure**.** The data obtained from the study was used to compute a remaining strength factor (RSF) to aid in the FFS evaluation of round thin areas in pressure vessels, piping and storage tanks. The RSF was defined as:

$$\mathrm{RSF} = \frac{\text{Collapse Pressure of Flawed Component}}{\text{Collapse Pressure of Unflawed Component}} \tag{2.1}$$

An RSF of 0.9 or greater is considered to be acceptable. The study was extended to groove-like local thin areas (GTAs) on spherical and cylindrical shells by Hantz et al. [65] using a bilinear model with the yield stress set at 10% lower than the one used for the RTA case, and the slope of the model set at a value equal to the yield strength at $P_{2\%}$. Results obtained from the EPFEA were used to develop a screening/acceptance criterion for axial and circumferential GTAs on cylinders and meridional GTAs on spheres.

Ultimate Tensile Strength (σ_{uts}) and Ductile Fracture Criteria

Leis and Stephens [56] proposed assessing the integrity of corroded pipelines using the uniaxial σ_{uts} as a reference failure stress. This produced more accurate prediction of failure pressures compared to using the yield stress-based values in ASME B31G and RSTRENG methods, as well as the uniaxial and multiaxial yield stress values. They used the work in [57] to develop an alternative assessment criterion for metal-loss involving complex loadings, complex flaw shapes, sizes and spacing via parametric analyses using a special purpose shell-based finite element code known as PCORR and a ductile fracture criteria, which encapsulates the yield stress (σ_y), σ_{uts} and the fracture toughness of the pipe. Based on internal pressure loading, the assessment method ranked the flaw depth and length as first order factors controlling the failure behaviour of the eroded pipes, while the flaw width was ranked as a second order factor. In another paper [58], the duo did a comparative investigation of the influence of material and geometry factors on the failure pressure of blunt corrosion defects and local thin areas (LTAs) in pipes. By employing existing experimental data, a ductile rupture criterion and parametric FEA, they succeeded in ranking the relative contribution of each variable to the failure pressure from most to least important as follows: Internal pressure, pipe diameter, wall thickness/flaw depth, ultimate strength, flaw length, flaw shape characteristics, yield strength/strain hardening characteristics, flaw width and fracture (Charpy) toughness.

Ultimate Tensile Stress (σ_{uts}) and 95% σ_{uts}

Shim et al. [66,67] performed three dimensional FEA to simulate full-scale pipe tests conducted for various wall-thinning geometries subjected to a combined loading (internal pressure and bending moment). Failure was predicted by obtaining the maximum moment when the equivalent stress in the thinned area reached the σ_{uts}. There was a good agreement when the FEA results were compared with the experimentally generated maximum moment. Using the same criterion, FEA were performed to investigate the effect of the internal pressure, wall-thinned length, depth and angle on the maximum moment.

Fekete and Varga [68] investigated the load carrying capacity of transmission steel pipe lines with external corrosion defects using a bilinear isotropic hardening material model in the nonlinear FEA. The characteristic flaw was modelled as an ellipsoid shape on the surface of the pipe. Burst pressure values were obtained from the analysis at the deepest point of the corrosion defect, where the Von Mises equivalent stresses were equal to the σ_{uts}. These results correlated well with the results obtained from experiment and semi-empirical methods. The effect of the width to length ratio of flaws on the load carrying capacity of the pipes was also examined.

Abdalla Filho and co-authors [69] used FEA to assess the accuracy of some analytical (semi-empirical) models commonly used in the industry to predict the failure pressure of pipelines containing wall reduction and isolated corrosion pit defects. An elastic-plastic model with isotropic hardening and Von Mises yield criterion was used in their work. The pipe was considered to have failed when the stress developed within the flawed area was equal to the pipe σ_{uts} or when local plastic collapse occurred. The corresponding pressure was taken as the failure pressure. The semi-empirical models and finite element shell models were validated by comparing their results to that of experimental data from the literature. The results show that semi-empirical methods are generally conservative when applied on short corrosion defects. The authors concluded that ASME B31G and RPA methods may be recommended for both short and long flaws assessment, RSTRENG 0.85 dL methods for short defects assessment only and the DNV RP-F101 model for long flaws assessment only.

Yeom et al. [70] established a corrosion defect assessment method for API X70 pipe via a full-scale burst test and FEA. The burst pressure results of the FEA were compared with results from popular analytical models used in the industry for different depth to thickness ratios at 25%, 50% and 75%. The failure behavior and burst pressures obtained from the full-scale test and FEA (at the point which the internal pressure reaches 95% of the σ_{uts}) were analyzed and compared, leading to the development of an integrity evaluation regression equation for the defected area.

True Ultimate Tensile Strength ($\sigma_{t,uts}$) and 90 % $\sigma_{t,uts}$

J. W. Kim et al. [71] did a series of tensile tests on notched bar specimens with varied notch radii. This was followed by finite element simulations to evaluate the stress and strain within the notched area of the specimens under internal pressure, which corresponds to their maximum load and final failure. From the results, the authors developed two local failure criteria (stress- and strain-based) that could be used to predict the maximum load carrying capacity and final failure for local wall-thinning in piping components. The stress-based criterion is based on the true ultimate tensile stress($\sigma_{t,uts}$), while the strain-based criterion is a function of stress triaxiality. Both criteria gave similar agreement with the experiment result, but the stress-based criterion was more accurate than the strain-based criterion, which overestimated the failure pressure of the pipes.

Ma et al. [72] carried out an assessment on the failure pressure of high strength pipelines (HSP) with external corrosion defects. First, they developed a theory to deduce the failure pressure of end-capped and unflawed pipes using the Von Mises failure criterion and Ramberg-Osgood hardening stress-strain relationship. They proceeded to do an extensive FEA for different geometrical sizes of the elliptical corrosion defect modelled on the pipe leading to a general solution for assessment of corroded HSP. This was done by considering the variation trend (via regression analysis) of the obtained burst pressure values when the Von Mises equivalent stress reaches $\sigma_{t,uts}$ of the steel. The outcome of their work was a new formula for predicting the failure pressure of corroded HSP. Results from the FEM were validated using 79 burst test samples involving low, mid, and high strength grade steel pipelines. The comparison showed that the predicted failure pressure is much closer to the actual burst pressure in HSP and for the mid-grade strength pipelines, but not reliable for low-grade strength pipelines.

Y.P Kim et al. [73] evaluated an X65 pipe that contained specially machined rectangular corrosion defects via full scale burst tests and FEA. For the simulation, failure was assumed to occur when the Von Mises stress at the defect area reached the reference stress value of 90% of the $\sigma_{t,uts}$. The limit solution for corrosion defects within the girth weld and seam weld of pipe was proposed as a function of corrosion length and depth based on the PCORR criterion by applying regression analysis on the FEA results.

Flow Stress

Kamaya et al. [74] investigated the failure pressure of a straight pipe with wall thinning subjected to internal pressure via 3D elastic-plastic FEA for small and large deformations. Three kinds of materials were considered in the analyses (line pipe steel, carbon steel, and stainless steel) and wall thinning was assumed to be of circumferentially uniform depth inside the pipe. The line pipe steel was observed to have the lowest failure pressure after normalizing its failure pressure by that of the unflawed pipe using flow stress (which is the average of the σ_y and σ_{uts}) as reference. The authors were able to show that with the assessment curves generated for line pipe steel, conservative estimates could be made for carbon steel and stainless steel. In another paper [75], they examined the influence of normalizing the flaw length on the failure pressure of pipes with localized thinning by conducting burst tests and 3D elastic-plastic FEA. The FEA was parameterized for various dimensions of pipes, flaw lengths and depths to study their effects on the failure pressure of the pipe. It was observed that the burst pressure decreases as the flaw length increases and in normalizing the effect of flaw length on failure pressure, it was more appropriate to normalize the flaw length by the pipe mean radius (R) of the unflawed area rather than its shell parameter $\left(\sqrt{Rt}\right)$ with a pipe thickness (t), as is usually done.

Yield, Flow, and Ultimate Tensile Strengths

Choi, et al. [76] proposed limit load solutions for X65 steel-type corroded pipelines by conducting a series of burst tests and finite element simulations. Two types of defect geometries were considered (rectangular and elliptical shapes). Reference stresses were set to:

- Yield Strength, σ_y
- Ultimate Tensile Strength, σ_{uts}
- Flow Strength, $\sigma_f, [\sigma_f = (\sigma_y + \sigma_{uts})/2]$
- 80% and 90% of σ_{uts}

These were all used as failure criteria. Failure was assumed to occur when the Von Mises stress distribution across the defected area reached the reference stress to which the corresponding internal pressure was taken as the failure pressure. Resulting failure pressures were normalized with corresponding experimental burst pressures. The best prediction for the elliptical shaped defect was at the reference stress of 80% of σ_{uts}, and for the rectangular defect, 90% of σ_{uts}. In comparison to the FEA solutions, the modified B31G results gave conservative estimates for shallow and short corrosion flaws but was non-conservative for deep and long flaws.

2.2.3 Boiler Tubes Localized Erosion Failures

It is noteworthy that though failure assessment criteria and methodologies for localized thinning or metal-loss in pressurized vessels have drawn a lot of attention over the years due to the associated failure implications of engineering structures, many of these studies have been focused on internal wall loss mechanisms associated with these vessels [55,62,65,69,76–80]. Only a few studies associated with developing failure criteria or methodology for localized external erosions in boiler tubes have been done. A key contribution in this area has been the scholarship of Zarrabi and colleagues [10,11,16,21].

Zarrabi [10,16,81] first developed a simple method to estimate the life of boiler tubes in fossil-fuel power plants. The method applies in cases where the failure mode is dominated by creep rupture and/or plastic collapse with fracture in the presence of tube thickness loss driven by corrosion and/or erosion processes. He formulated a computation for the plastic collapse, reference stress of the tube, its thinning rate and creep rupture time. He noted that in the absence of creep, the reference stress will be equal to the flow stress, which is the average of σ_y and σ_{uts}. An algorithm for computing the remaining life of the tube was also documented. The author also carried out a comparison with three other boiler tube life prediction methods, of which the method he proposed was better at predicting the tube life.

Zarrabi and Zhang [21] performed an elastic-plastic finite element analyses (EPFEA) to obtain primary stresses in the localized thinned area of a tube. From their study, they came up with a parameter (P^*) that when multiplied with the primary stress in the unflawed area results in the primary stress of the flawed area. P^* was defined as:

$$P^* = \frac{\text{Plastic Collapse Pressure of a Tube with Uniform Thickness}}{\text{Plastic Collapse Pressure of the Tube in the Local Thin Area}} \tag{2.2}$$

It was computed from the EPFEA of a tube with a part-through rectangular slot (flaw) using an elastic-perfectly plastic material model and a Von Mises yield criterion. P^* values were also computed for an elliptical flaw, triangular flaw and a double rectangular flaw. Results from these analyses were compared using their plastic collapse pressures and radial displacements at the deepest point of the flaw area. The triangular flaw had the highest collapse pressure value.

Zarrabi and Zhang [11] also described a method for life and failure thickness assessment of boiler tubes with localized pits and coded the method into a computer program referred to as ‘AUSI-TLI’. With this program, the tube remaining life, critical tube thickness and critical stress were assessed and evaluated.

In the work of Zarrabi and Zhang, the estimated creep and plastic collapse life they computed used a conservative reference failure stress derived from multiplying a semi-empirical non-dimensional parameter to account for the variation of the scar geometry with the Von Mises stresses of an undamaged tube, along with the tube material properties and operating conditions [10,11,81]. This model cannot be relied upon because of its over-conservativeness.

Gong et al. [30] investigated some ruptured titanium tubes that were obtained from a power plant by microscopic analyses and FEA. This was performed to evaluate the effect that stresses from degradation processes (such as clogging, erosion and fretting) exerted on the wall of the tubes. Also, from the result of the FEA, they were able to deduce the extent of degradation of the tubes and suggest some preventive measures.

DePadova et al. [82] performed FEA on the local thin areas (narrow and wide grooves) on two pressure vessels. The FEA results that included strain hardening reasonably predicted the plastic strains associated with the failure of these vessels, which were in good agreement with the test data, while the elastic perfectly plastic FEA results were conservative.

FEA was also used by Kim et al. [83], for the burst failure prediction of a plain seamed tube, a second tube with a weldment, and a third one with a heat affected zone, all made to bulge under combined internal pressure and axial loading. The outcome of their analyses showed some feasibility of predicting an initial fracture initiation and bursting pressures of these tubes.

In a study by Othman et al. [84], superheater tubes were modelled, and the maximum stress induced by the deformed tube was obtained. The results obtained had a good correlation with those obtained from the power plant.

Visual examination and microscopic analyses that includes SEM, EDS and XRD were carried out by Dini et al. [85] on some tubes with oxide scales. Numerical analysis of these tubes under continuous annealing were also carried out to determine the effect of increased temperature on the tube life as well as the extent of damage in the tubes. The result of the analysis indicated the potential of the damaged region in the tubes to be prone to high temperature creep failure.

Purbolaksono et al. [86], carried out failure case studies on SA 213-T22 reheater and superheater steel tubes. They used finite element simulations with iterative methods to estimate the remaining life of the tubes. This was done by tracking the increased temperature and decreased hardness due to cumulative creep damage, i.e., as oxide scales grow on their inner surface of the tubes over a long period. The estimations obtained show some good agreement with the experimental data retrieved from the reports on the failed tubes and could provide forewarning to enable prior action to be taken before failure occurs. In a similar study, Purbolaksono et al [87] used the average growth rate of the oxide scales in some reheater tubes to model 2D axisymmetric geometries using MSC PATRAN/NASTRAN and some measurements obtained from the tube samples. The results from the FEA were reported to be in good agreement with the microscopic inspections carried out on the tubes.

Though the above works have showed some progress in using FEA for failure assessment of boiler tubes, a focused study on which flaws in boiler tubes are most at risk of failure due to plastic collapse has not been done. Detailed studies are needed to able to rank detected flaws from most severe to least severe. This would allow operators to optimize the available maintenance budget and focus attention where necessary, reducing the likelihood of unexpected outages.

2.2.4 API-ASME Fitness-For-Service (FFS) Assessments

As noted earlier for common analytical methods and criteria, design codes and standards for pressurized vessels that have been in existence often provide rules and analyses for the design, manufacturing, inspection, and testing of new pressurized equipment (pressure vessels, pipes and storage tanks) but do not provide rules for evaluating these equipment while they degrade in service or become deficient due to the presence of a flaw or damage. But in recent years, the American Petroleum Institute (API) and the American Society of Mechanical Engineers (ASME) have made efforts to develop a standard document built from previous local thin area (LTA) failure assessment criteria and methodologies that will provide some guidance towards carrying out quantitative engineering assessments to demonstrate the structural integrity of components of pressurized vessels, containing damage or a flaw while in use.

API 579 assessment guide

Anderson and Osage [88] presented an overview of the API Recommended Practice 579 [89], which was the first document for FFS assessment guide for pressurized vessels. API 579 was designed to provide guidance for conducting FFS assessments of a wide range of flaws and damage mechanisms (such as brittle fracture, cracks, metal-loss, pitting corrosion, blisters, weld misalignment, etc.) that usually occur in pressure vessels, piping, and storage tanks encountered in petrochemical and other processing industries. The guidelines provided in API 579 were to enable plant inspectors and engineering personnel to make decisions to rerate, repair, replace or retire the flawed component under assessment. The authors described the organization of the API document, the three levels used in the assessment methodology and the rerating and remaining life calculations. Similarly, Janelle and Osage in 2007 reviewed the technical basis for the fitness-for-service assessment procedures for general and local metal loss in API 579. Validation of the procedures and additional methods developed for analyzing and evaluating LTAs were discussed and recommended to be included in the API 579 standard.

API 579-1/ASME FFS-1 and API 579-2/ASME FFS-2 assessment guides

The methodology and criteria documented in the API 579 Standard document were tailored for structural components used in the refining and petrochemical industries. A few years after, ASME and API jointly came up with one standard document in two parts (referred to as API 579-1/ASME FFS-1 and API 579-2/ASME FFS-2 assessment guides) [90,91] to provide guidelines for FFS assessment for a wide range of in-service structural components used in process, manufacturing, and power generation industries. The first part explains the methodologies to be used for the FFS assessment while the second part documents some practical example problems. A newer edition, which include some modifications and additional assessments was released in 2016 [33].

The standard provides for three levels of assessment for evaluating LTAs, which are Level 1, 2 and 3, just like in the API 579. Generally, each level presents a balance between the information required for the evaluation, conservatism, personnel skill performing the evaluation and the complexity of the assessment being performed. Level 1 is the most conservative. The procedures contained in this level are envisaged to provide conservative assessment criteria that can be performed using a minimum amount of component information and inspection. There is also a limiting flaw size that can be evaluated using this level, which makes it unsuitable for components with complex geometry and/or complex loading. As it is not a detailed analysis, a plant inspector or an engineering personnel could perform this level assessment.

Level 2 assessment procedures are intended to present a more detailed evaluation that produces less conservative outcomes compared to those from Level 1 evaluation. Similar amount of component information and inspection with that of Level 1 assessment are required for this level assessment, as well as more detailed calculations. Flaw geometries that could not be assessed using Level 1 can be evaluated, though would still be limited for complex flaw geometries. The Level 2 assessment is usually performed by plant engineers or engineering specialists that are knowledgeable and experienced in conducting FFS evaluation.

The Level 3 assessment procedures are intended to provide the most accurate evaluation of all the three levels. As the levels increase from 1 through to 3, the amount of conservatism associated with their methodologies decreases, making the Level 3 assessment the most precise. Level 3 assessment requires the most detailed component information and inspection, with the proposed analysis to be based on a numerical technique (such as FEM) or experimental technique if necessary. As such, engineering specialists that are skilled and experienced in conducting FFS evaluation are usually those who would perform this level of assessment. From the API-ASME FFS, protection against plastic collapse is typically a stress analysis method, which could either be a linear or nonlinear stress analysis, similar to the procedures documented in the recent ASME Design Standard [34] as reported earlier in Section 2.2.1, only with additional difference since the analysis is to be carried out on flawed components.

In this case, the LLA employs numerical analysis using small displacement theory and an elastic-perfectly plastic material model set at a specific yield strength of $1.5\sigma_a$. The σ_a is the allowable stress, which is typically a fraction of yield, tensile or rupture stress at room and service temperatures. For the EPSA, an elastic plastic material model, large displacement theory (to account for the effect of nonlinearity) and a true stress-strain hardening material model, which is temperature dependent, are used. This ensures that in the model, the hardening behavior gets up to the true ultimate tensile stress $(\sigma_{t,uts})$. Beyond this, the behaviour is perfectly plastic. The EPSA provides a more accurate FFS assessment, as it considers the redistribution of stress that occurs due to the plastic deformation of the flawed components, and their deformation characteristics.

For the FFS assessment using nonlinear analysis, the concept of Load and Resistance Factor Design (LRFD) is suggested as an alternative to be used instead of determining the plastic collapse load of the vessel [33]. For the LRFD, different factored load combinations, based on the loads the vessel is subjected to, are used for the numerical analysis. For the case of internal or external pressure only, the required factored load combinations are given as follows:

$$\text{Factored Load for Limit Load Analysis} = 1.5.P_{max}.RSF_a \tag{2.3}$$

$$\text{Factored Load for Elastic Plastic Analysis} = \beta.P_{max} \tag{2.4}$$

where P_{max} is the Internal or External Maximum Allowable Working Pressure, RSF_a is the Allowable Remaining Strength Factor with a recommended value of 0.9 (the value can be more or less conservative depending on the design codes used for the vessel construction, type of loading and/or consequence of failure), and β is the Load Factor Coefficient based on the factor applied to the σ_{uts} to obtain a design allowable stress, (the value varies for different construction codes). For pressure vessels designed using ASME Section VIII, Division 2 prior to the 2007 edition, $\beta = 3.RSF_a$. Based on these guidelines, the factored load combinations to be used for the limit load analysis becomes $1.35.P_{max}$ and that of the Elastic Plastic Analysis is $2.7.P_{max}$.

The analyses are to be performed using these factored loads and if convergence is attained, that indicates the component being analysed is stable under the applied load. If not, its thickness shall be modified or the applied loads reduced, and the analysis is repeated until convergence is attained.

Another approach described in the document for evaluating LTAs is using the Remaining Strength Factor, *RSF*, which was first proposed by Sims [64]. This was expressed as:

$$RSF = \frac{\text{Limit or Plastic Collapse Load of the Flawed Component}}{\text{Limit or Plastic Collapse Load of the Unflawed Component}} \tag{2.5}$$

Based on the outcome of the RSF, the component analysed can be recommended to continue to be used as it is or to be repaired or the Maximum Allowable Working Pressure of the Flawed Component (*MAWP*) evaluated and altered or rerated using the Maximum Allowable Working Pressure of the Unflawed Component ($MAWP_o$). These quantities are as expressed [33]:

$$MAWP = MAWP_o\left(\frac{\mathrm{RSF}}{\mathrm{RSF_a}}\right) \text{ for } RSF < RSF_a \tag{2.6}$$

$$MAWP = MAWP_o\left(\frac{\mathrm{RSF}}{\mathrm{RSF_a}}\right) \text{ for } RSF \geq RSF_a \tag{2.7}$$

A decision can also be made to retire the analysed tube if the *RSF* outcome is too low.

2.2.5 Challenges with the API 579 and ASME FFS Assessment Guides

Though the elastic-plastic analysis method as proposed in the FFS document is the most reliable guide for localized thinning evaluation, it still presents some challenges. First, detailed inspection and component information is required before doing the analysis, not only for level 3 assessment but for the other two levels as well. Second, cumbersome FEA simulation is required each and every time you need to do an assessment for a particular flaw, which must be performed by an experienced engineering specialist. In fact, before the level 3 assessment will be performed, the detected localized flaw on the vessel would have undergone the rigors of level 1 and 2 assessments and certified to have failed to meet their acceptability criteria. These challenges are time consuming and financially expensive to cater for.

Also, with the concept of LRFD as suggested to be used for the FEA, there is still the rigor of setting up and running a detailed FEA for each localized flaw to be assessed in this level. To avoid computing plastic collapse loads, which could consume computational resources and time, the factored loads that were proposed as reasonable estimates are empirical and as such, has the capability to still give relatively conservative plastic collapse results.

Based on the above issues, there is, therefore, a need to develop a new, less complex and less expensive methodology that could be used to rapidly categorize the severity of localized external erosion flaws in boiler tubes and guide maintenance decisions on these critical assets.

2.3 Summary and Conclusions

In this chapter, the initial studies that led to the development of various criteria and methodologies for assessing failures in pressure vessels were discussed. Previous studies from a general perspective of failure analysis of pressurized vessels to studies on failure assessments of flawed pressure vessels, as well as assessment of localized thinned vessels were all discussed in details. The chapter also reviewed methodologies and criteria proposed by various authors that could be used for evaluating pressurized vessels and guard against their plastic collapse while in use. These criteria include:

- 2% Plastic strain
- RSF Criteria
- σ_{uts}
- 95% σ_{uts}
- 90% σ_{uts}
- 80% σ_{uts}
- Ductile Fracture Criteria
- $\sigma_{t,uts}$
- 90 % $\sigma_{t,uts}$
- σ_y
- Flow Stress, σ_f.

Numerical studies that have been carried out on localized thinning in boiler tubes were discussed. Though these finite element studies were performed to determine the root cause of these failures and provide some preventive measures to avoid their reoccurrence, yet more detailed study is needed to provide a rapid decision-making tool to guide in categorizing the severity of these defects. The API-ASME fitness-for-service assessment guides recently proposed to be used were also discussed and the challenges inherent in them were highlighted.

From the review, it is apparent that more detailed studies are needed to avoid replacing tubes that could still be safe for continued operation, while also guarding against the failure of the tubes, their emergency costly repairs and forced outages. The next chapter presents the modeling procedures for some conceptualized flawed tubes, the geometric definition of the modelled flaws and the technique that can be used to replicate real flawed tubes on these conceptualized models.

3 MODELLING OF LOCALIZED THINNED TUBES AND GEOMETRIC DEFINITIONS OF THE FLAWS

3.1 Introduction

The first procedure to carrying out a detailed investigation on localized external eroded tubes is to create geometric models in a way that is sufficiently flexible and could reasonably capture real flaw geometries that exist in practical scenarios. In this chapter, the modeling of some conceptualized variants of tubes having geometrical shapes of localized external erosion that could possibly occur in real scenarios is presented. The formulation of geometry functions from these conceptualized models to enable the accurate modelling of real localized thinned tubes and aid in their detailed failure assessment is documented. The process of replicating real tubes on these developed geometries is also discussed.

3.2 Modelling of Conceptualized Flawed Tubes

Previous FEA studies on boiler tubes were done using flaw geometries such as: elliptical scar, triangular scar, rectangular scar, double rectangular scar and part-through rectangular scar [11,21,81] as can be seen in Figure 3.1. These flaw geometries do not resemble practical scenarios of localized external erosion. Other defects modelled on erosion of titanium tubes in heat exchangers [30] and as corrosion defects on pipes [68] were more suitable as seen in Figure 3.2.

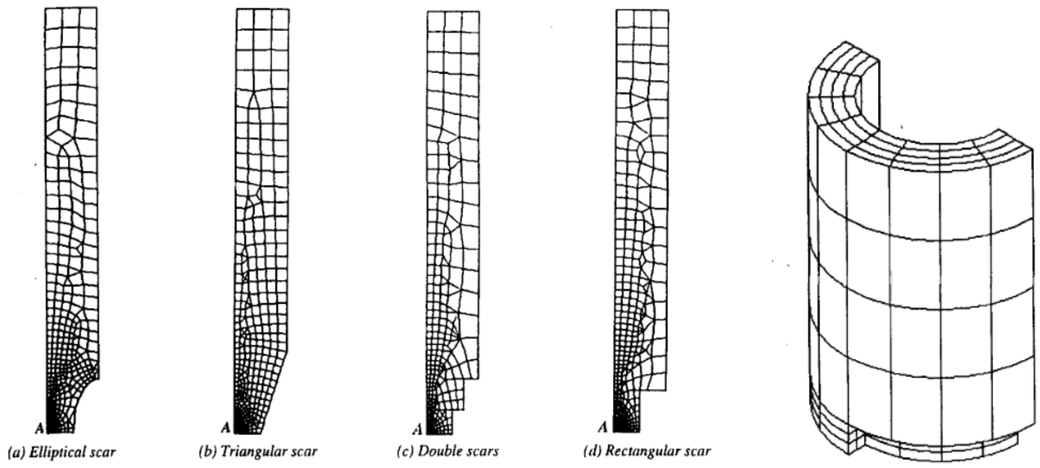

(a) Elliptical scar (b) Triangular scar (c) Double scars (d) Rectangular scar

Figure 3.1: (a) Various modelled flaw shapes on boiler tubes [21] and (b) Part-through rectangular modelled flawed tube [21,81].

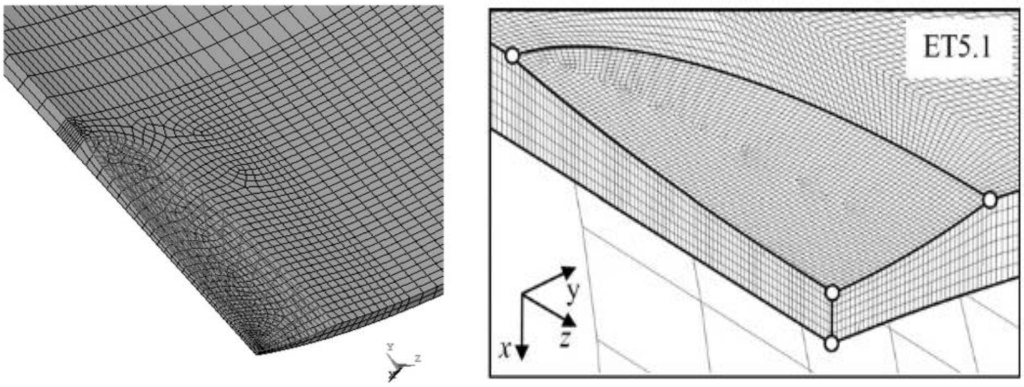

Figure 3.2: Modelled elliptical erosion defect of a titanium tube [30] and (b) corrosion defect on a pipe [68].

To mimic real types of localized thinned flaws that could possibly occur in practical scenarios, three conceptualized variants of localized thinned areas having a specific flaw depth, f_d are created on an open-ended flawed tube modelled in ANSYS® using the DesignModeler. Figure 3.3 shows a modelled tube having a localized thinned area (LTA), with flaw length (f_l) and flaw width (f_w) as the LTA dimensions.

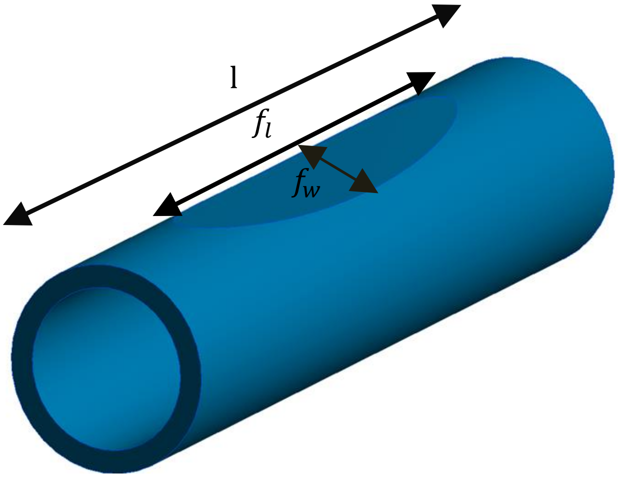

Figure 3.3: Sample of a modelled tube showing the localized thinned area.

The three variants are created by sweeping a flat line, a concave and a convex elliptical surfaces as described below in details.

The first variant referred to as the **flat line flaw** is made by first offsetting a plane, height, H from the centre line of the tube and sketching a horizontal straight line at the specific flaw depth, f_d. The sketch is revolved about the x-axis from the position of the plane to slice and cut the tube to the f_d as shown in Figure 3.4 to Figure 3.6.

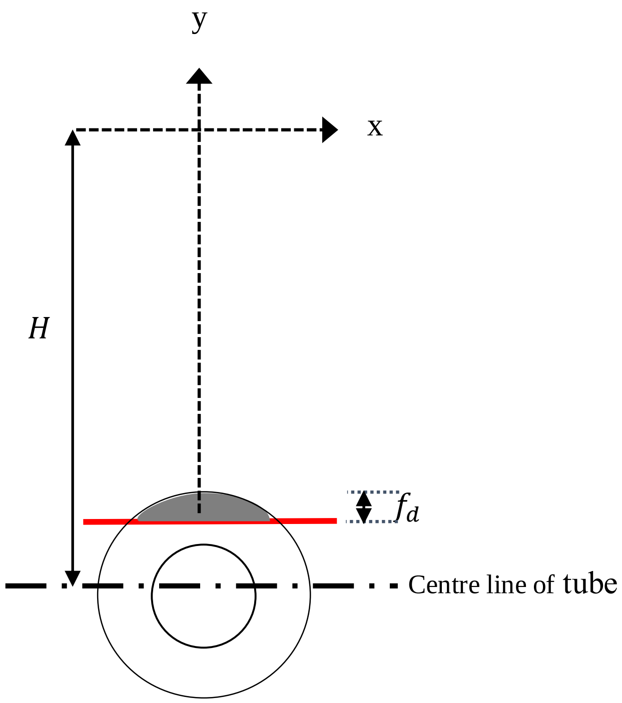

Figure 3.4: Schematic showing the modelling of a flat line flawed tube - cross-section

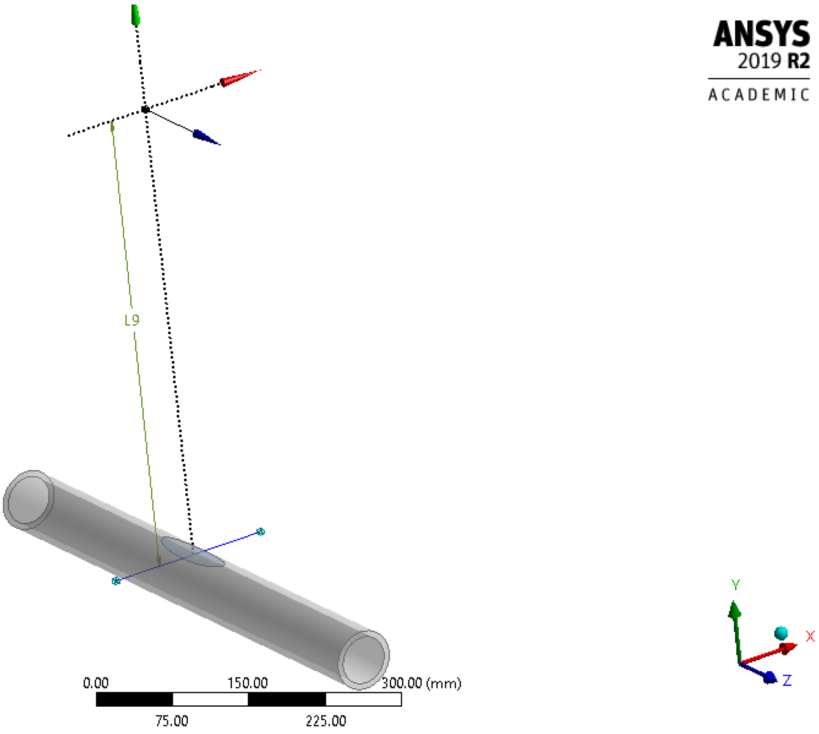

Figure 3.5: Pictorial representation in ANSYS® showing the plane axis offset from the centre line of the tube, the sketched horizontal line and the flat line modelled flaw

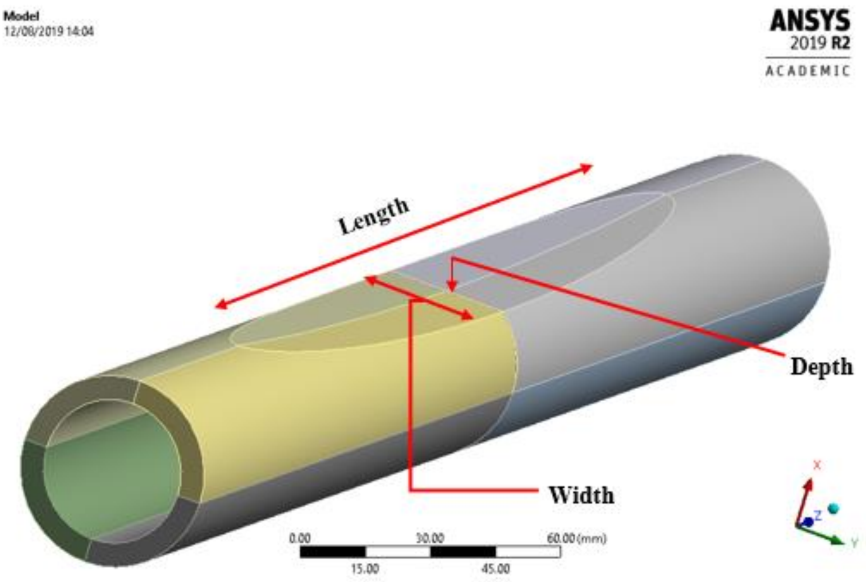

Figure 3.6: A flat line flawed tube

The second modelled localized flaw on the tube is a **u-shaped or scoop shaped flaw**, created by offsetting a plane from the centre line of the tube to a height, H, then sketching from the mid-axis of the tube a convex ellipse with an axis offset by a height, z from the tube centre line. This makes the ellipse intersect the circular cross section of the tube in a u-shaped manner. The sketch is revolved from the plane axis at H in the horizontal direction to slice-cut the tube to a specific f_d as shown in Figure 3.7 to Figure 3.9.

The third variant referred to as the **n-shaped or saddle shaped flaw** is made by first offsetting from the tube centre line to a height, H, then sketching a concave ellipse that is offset from the base to a height, z and also two vertical straight lines drawn from the plane to the vertices of the ellipse. This causes the ellipse to intersect the circular cross section of the tube in an n-shaped manner. The entire sketch is revolved about the x-axis from the vertical plane and sliced-cut to the required flaw depth, f_d on the tube as shown in Figure 3.10 to Figure 3.12.

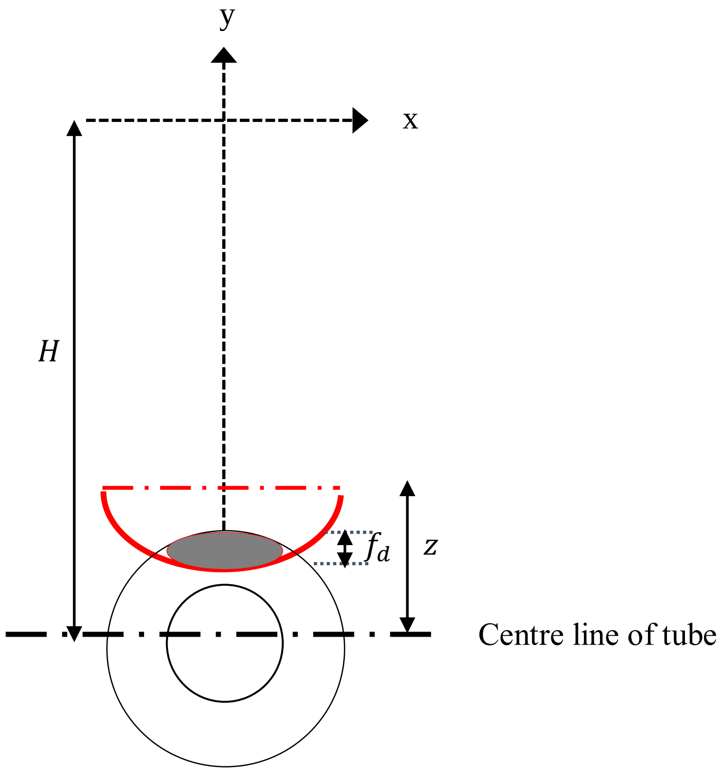

Figure 3.7: Schematic showing the modelling of a u-shaped flawed tube - cross-section.

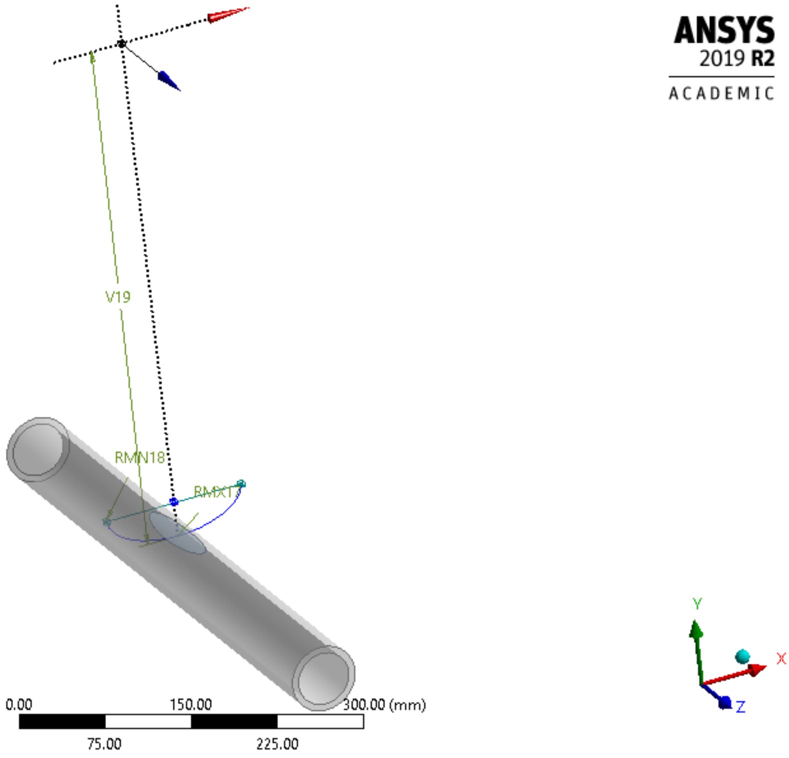

Figure 3.8: Pictorial representation in ANSYS® showing the plane axis offset from the centre line of the tube, the sketched convex ellipse and the u-shaped flaw.

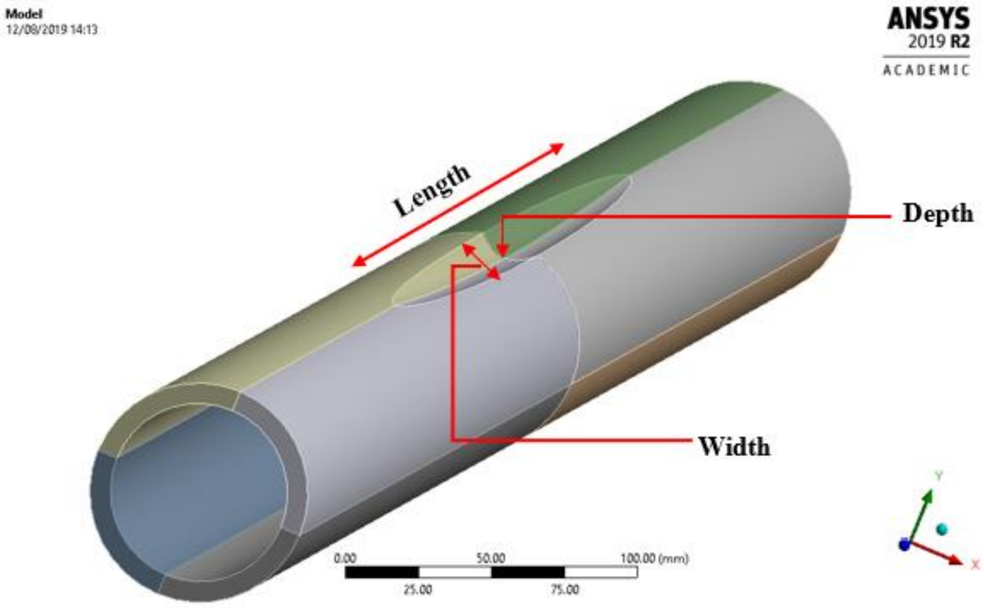

Figure 3.9: A u-shaped flawed tube.

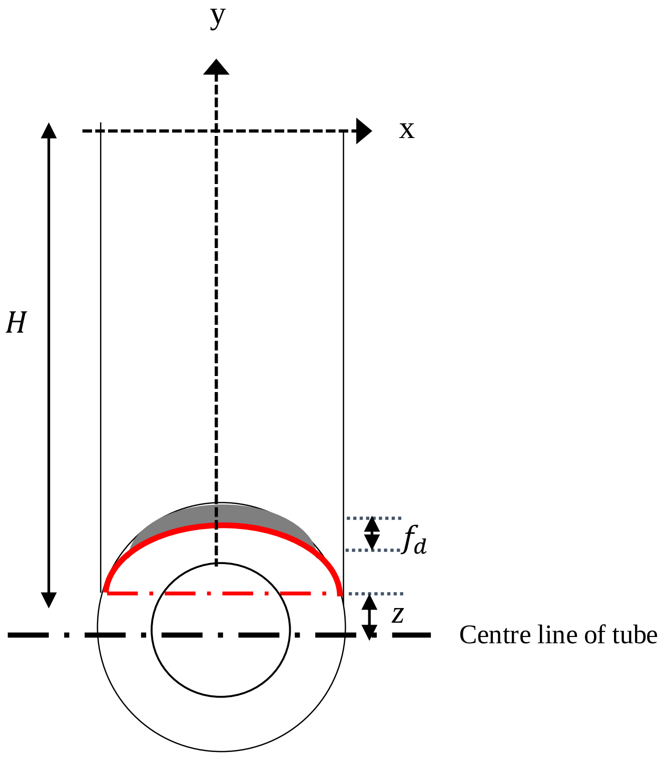

Figure 3.10: Schematic showing the modelling of an n-shaped flawed tube - cross-section.

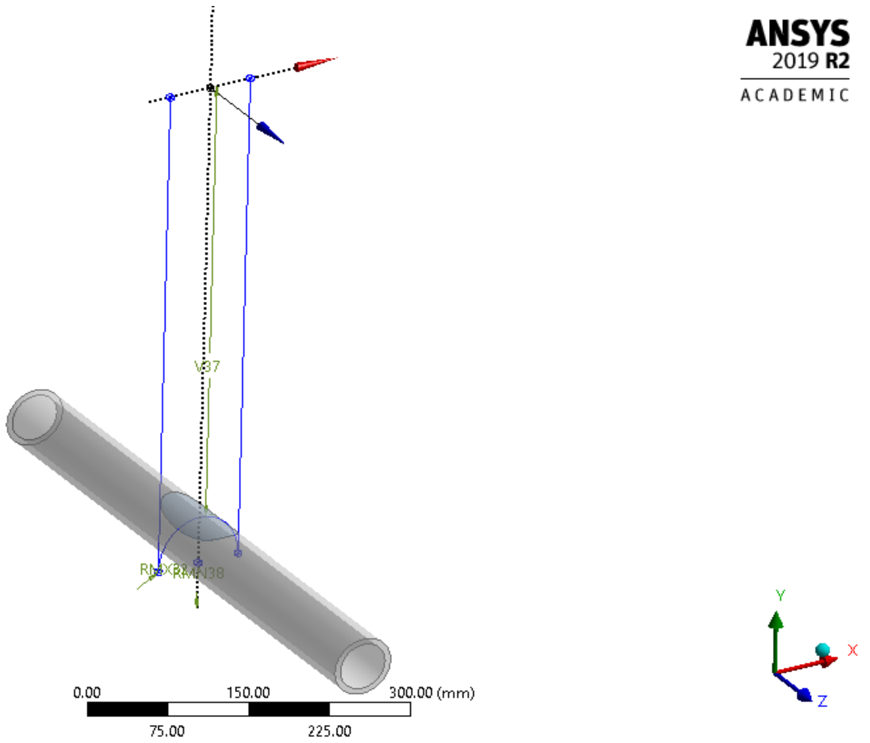

Figure 3.11: Pictorial representation in ANSYS® showing the plane axis offset from the centre line of the tube, the sketched concave ellipse and the n-shaped flaw.

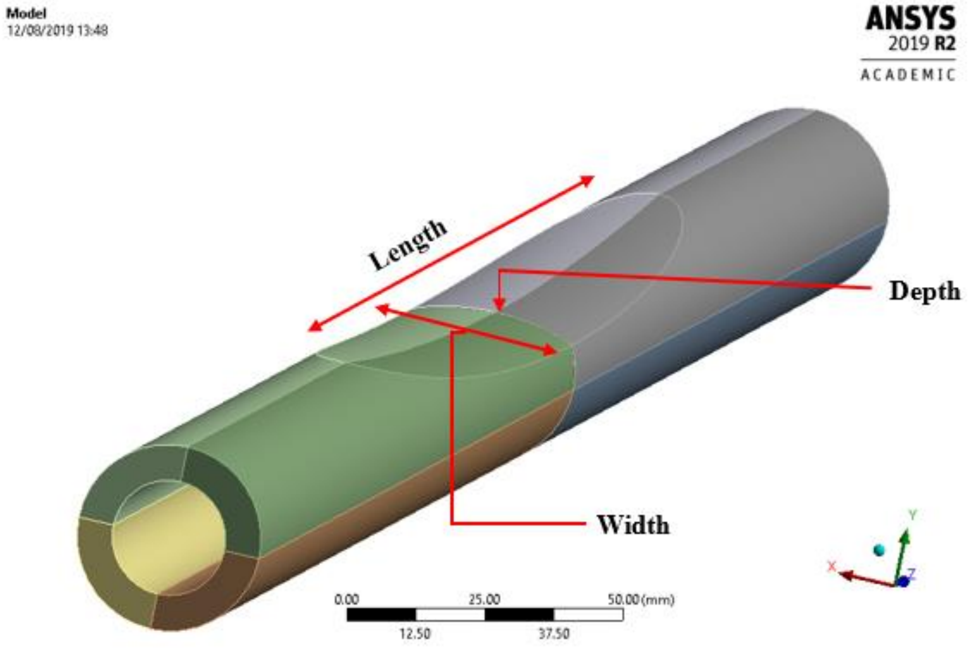

Figure 3.12: An n-shaped flawed tube.

After the creation of the flaw geometry on the model, it is sliced three times through each of the base planes (XY, ZX, and YZ Planes) in ANSYS. The outer flaw surface of the tube is then deleted, and the flaw surface extruded through a slice operation in the reversed direction to a depth greater than or relatively less than the tube thickness, depending on the shape of the flaw. Based on symmetry conditions of the FEM, three quarter of the model is deleted, leaving a quarter model to be used for the analysis as shown in Figure 3.13 (a). This is done to save computation time during the analysis. The flaw area is further sliced from the YZ base plane through the Z axis that is offset to half of the f_w, to facilitate the easy application of mesh control measures within the flaw area during the mechanical analysis. Figure 3.13 (b) shows the sliced flawed tube.

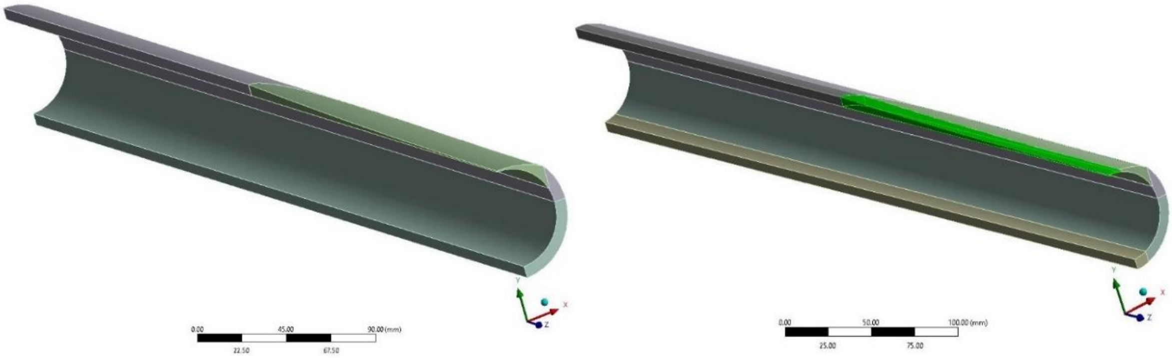

Figure 3.13: Quarter n-shaped finite element model showing (a) the extruded flaw area and (b) the sliced flaw area.

3.3 Geometric Definition of the Flaws

Having developed these conceptualized flawed tubes, it is necessary to generate some geometry functions from these conceptualized models that will enable the accurate modelling of real localized thinned tubes to carry out NLFEA and parametric studies for their failure assessment. The mathematical expressions for the tube flaw geometries: the flaw length (f_l), flaw width (f_w), and flaw depth (f_d) are formulated for a tube with an outer diameter (D_o) and tube thickness (t) using the following parameters:

- Plane height from the centre line of the tube (H)
- Radius of the cutting plane from the plane axis (R)
- Horizontal dimension of the elliptical surface (a)
- Vertical dimension of elliptical surface (b)
- Remaining thickness of the tube (t_r)

3.3.1 Computing the flaw length, f_l

The f_l of the flawed tube, which is the same for all three variants is derived from the schematic shown in Figure 3.14

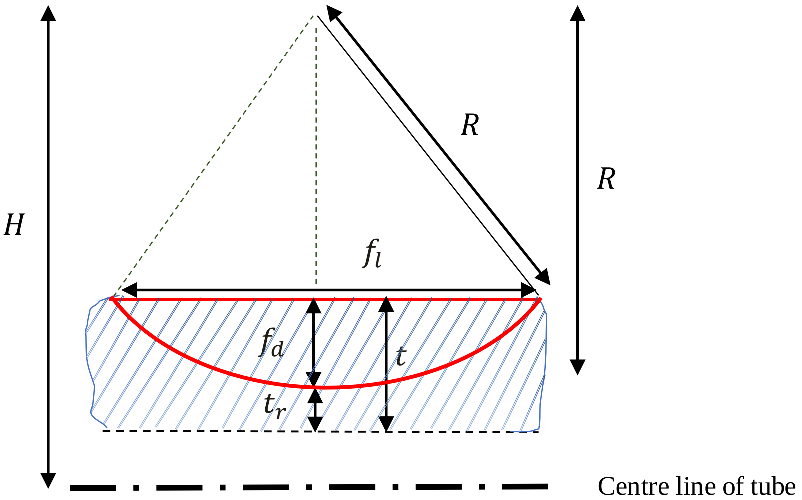

Figure 3.14: Schematic showing the creation of the localized flaw length on the tube – side view.

The cutting radius, R is given by:

$$R \;=\; H - [(\tfrac{D_o}{2}) - f_d] \tag{3.1}$$

By Pythagorean Theorem,

$$R^2 \;=\; (R - f_d)^2 + (\tfrac{f_l}{2})^2 \tag{3.2}$$

Rearranging to solve for f_l,

$$f_l = 2\sqrt{R^2 - (R - f_d)^2} \tag{3.3}$$

which simplifies to:

$$f_l = 2\sqrt{2Rf_d - {f_d}^2} \tag{3.4}$$

3.3.2 Computing the flaw width, f_w for the flat-line flaw

The f_w of the **flat line flaw** is derived from the schematic showing the intersection of the flat line with the circular cross section of the tube shown in Figure 3.15.

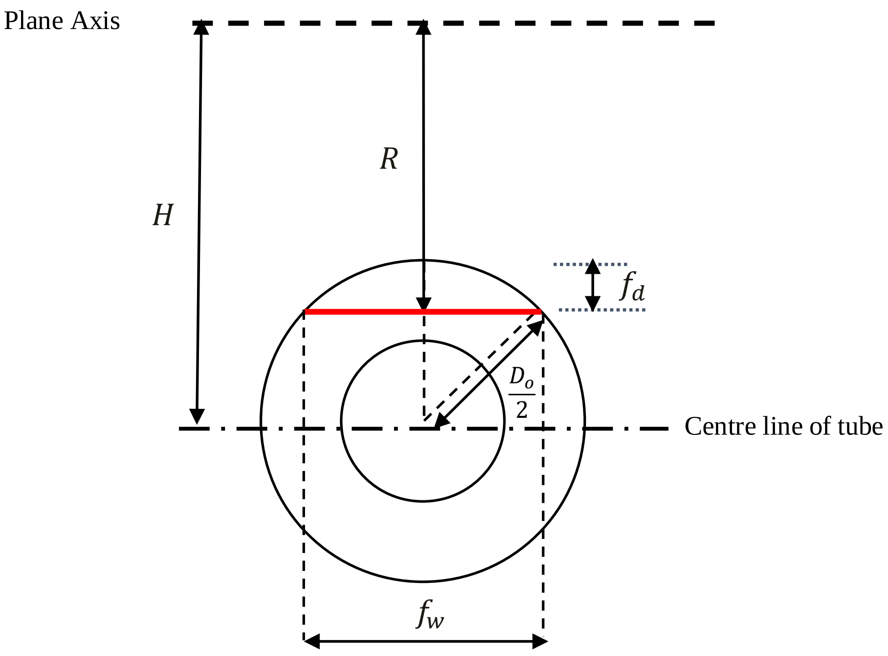

Figure 3.15: Front view of the flat line flaw showing the cutting plane in red, intersected with the tube cross-section.

Applying Pythagoras,

$$\left(\frac{D_o}{2}\right)^2 = \left(\left(\frac{D_o}{2}\right) - f_d\right)^2 + \left(\frac{f_w}{2}\right)^2 \tag{3.5}$$

Rearranging to solve for f_w,

$$f_w = 2\sqrt{\left(\frac{D_o}{2}\right)^2 - \left(\left(\frac{D_o}{2}\right) - f_d\right)^2} \tag{3.6}$$

which simplifies to:

$$f_w = 2\sqrt{D_o f_d - {f_d}^2} \tag{3.7}$$

3.3.3 Computing the flaw width, f_w for both the u-shaped and n-shaped flaws

The f_w of the **u-shaped flaw** is derived from the schematic showing the intersection of the convex ellipse with the circular cross section of the tube as shown in Figure 3.17. While the f_w of the **n-shaped flaw** is derived from the schematic showing the intersection of the concave ellipse with the circular cross section of the tube as seen in Figure 3.16. Tubes with f_w/D_o dimension ratio of less than 0.5 are **u-shaped flaws** while others above 0.5 are **n-shaped flaws**.

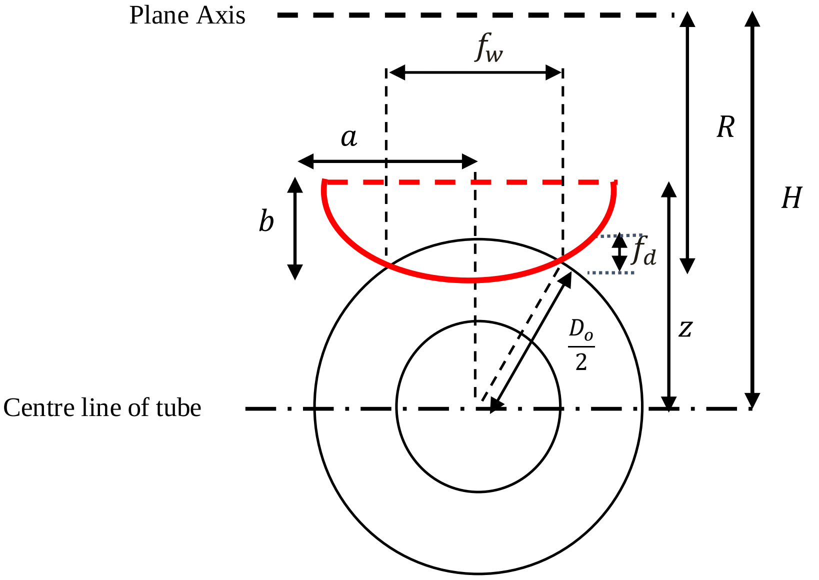

Figure 3.16: Front view of the u-shaped flaw showing the cutting plane in red, intersected with the tube cross-section.

From **Figure 3.16**,

$$f_d = \frac{D_o}{2} - (H - R) \tag{3.8}$$

$$f_d = \frac{D_o}{2} - (z - b) \tag{3.9}$$

$$R = H - (z - b) \tag{3.10}$$

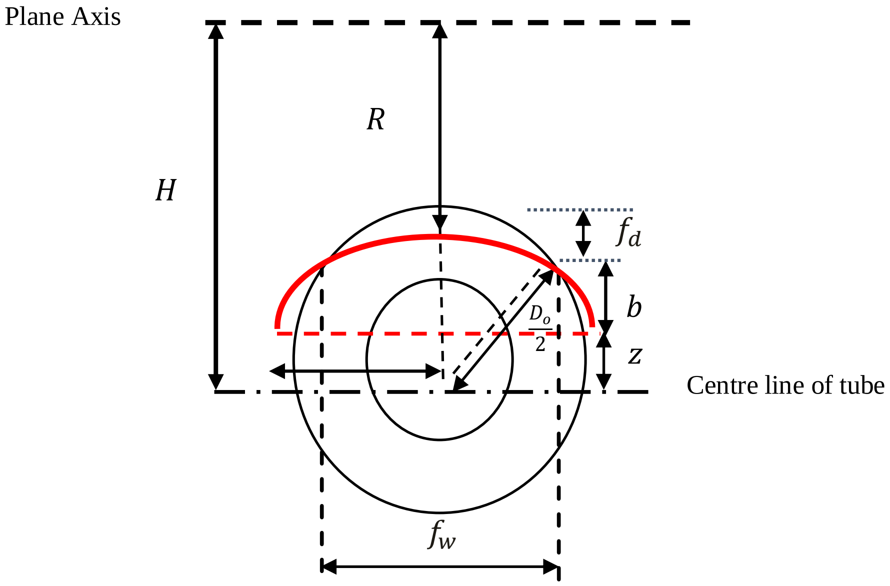

Figure 3.17: Front view of the n-shaped flaw showing the cutting plane in red, intersected with the tube cross-section.

From **Figure 3.17**,

$$f_d = \frac{D_o}{2} - (H - R) \tag{3.11}$$

$$f_d = \frac{D_o}{2} - (z + b) \tag{3.12}$$

$$R = H - (z + b) \tag{3.13}$$

To formulate the mathematical expression for the f_w, the point of intersection on the x-axis of the circle and ellipse need to be determined. The two simultaneous equations below are considered:

For the circle:

$$x^2 + y^2 = r_o^2 \tag{3.14}$$

For the ellipse:

$$\frac{x^2}{a^2} + \frac{(y-z)^2}{b^2} = 1 \tag{3.15}$$

By solving these two equations (as documented fully in Appendix A), the value of the f_w in terms of x is obtained from:

$$x = \sqrt{\frac{-B \pm \sqrt{(B^2 - 4AC)}}{2A}} \tag{3.16}$$

$$where\ A = \left(1 - \frac{b^2}{a^2}\right)^2;\ B = \frac{4b^2z^2}{a^2} + 2\left(1 - \frac{b^2}{a^2}\right)(b^2 + z^2 - r_o^2);\ C = (b^2 + z^2 - r_o^2)^2 - b^2z^2$$

From Eq. (3.16), f_w of either the n-shaped flawed tube or the u-shaped flawed tube can be computed as $\boldsymbol{2x}$ for their full dimension, as shown below:

$$2.\sqrt{\frac{-\frac{4b^2z^2}{a^2} + 2\left(1 - \frac{b^2}{a^2}\right)(b^2 + z^2 - r_o^2) \pm \sqrt{\left(\left(\frac{4b^2z^2}{a^2} + 2\left(1 - \frac{b^2}{a^2}\right)(b^2 + z^2 - r_o^2)\right)^2 - 4\left(1 - \frac{b^2}{a^2}\right)^2 C = (b^2 + z^2 - r_o^2)^2 - 4b^2z^2\right)}}{2\left(1 - \frac{b^2}{a^2}\right)^2}}$$

These developed mathematical expressions allow for the determination of the f_l, f_w and $f_{d,}$ as functions of the model parameters, which is instrumental for the failure assessment of the tubes.

3.4 Technique used to Extract Flaw Geometric Properties of Real Failed Tubes.

The equations defined in Section 3.3 allow the flaw geometric properties (f_w, f_l, t_r) to be determined from the parameters of the cutting ellipse (H, R, a and b). However, to model a specific real flaw for which the flaw geometric properties are known, the cutting ellipse parameters need to be determined. This is a simple inverse problem. A built-in optimization nonlinear function in MATLAB® [92] known as `fminsearch` that can find the minimum of a function of several variables in an unconstrained domain is used to obtain the flaw geometric properties of real localized thinned tubes in order to precisely model them. The function expression used is shown below:

`[xopt,fopt]=fminsearch('FitPipeFnx',[H R a b])` (3.17)

where `xopt` is the returned optimized output, `fopt` holds the returned value of the objective function, `FitPipeFnx` represents the function to be minimized, which in this case is the `error` between the measured flawed tube geometric dimensions and the computed flawed tube geometric dimensions from the derived mathematical expressions. `H, R, a, b`, are the starting input variables used.

The codes for the implementation of this technique and the `FitPipeFnx` function can be found in Appendix B. The program also contained codes that constructed the shape of the flawed tubes as they solved, which helped in deducing whether the obtained solution is realistic. A good initial estimate for the starting variables is needed in order to effectively use it. Table 3.1 shows the flaw geometric properties obtained using this technique for three real cases of failed tubes [93].

Table 3.1: Flaw geometric properties extracted from three real failed tubes using the optimization technique.

Tube No	Tube and flaw properties					Input parameters			
	D_o (mm)	t (mm)	t_r (mm)	f_l (mm)	f_w (mm)	H (mm)	R (mm)	a (mm)	b (mm)
1.	75.0	7.0	0.50	600	20	6957.333	6926.333	30.013	89.990
2.	50.8	4.4	0.30	80	25	218.477	197.177	105.101	114.305
3.	50.8	4.4	0.17	70	40	168.088	146.911	25.191	14.062

3.5 Summary and Conclusions

In this chapter, geometric variants of localized thinned tubes with real geometries, as could be seen in actual scenarios were modelled. Geometric functions that could help to model real localized thinned tubes were formulated from the developed models. The technique that could be used to extract flaw geometric properties from real tubes so they could be effectively replicated on conceptualized geometries was documented.

The next chapter presents the report of detailed investigations conducted on the developed models to determine the factors that influence the failure of these tubes while in use.

4 INVESTIGATION OF FACTORS INFLUENCING THE FAILURE OF BOILER TUBES UNDER LOCALIZED EXTERNAL EROSION

4.1 Introduction

Boiler tubes which have experienced a significant localized reduction in their wall thickness as a consequence of external erosion become susceptible to gross plastic deformation, and ultimately rupture [7–9,19,23]. In this chapter, comprehensive investigations by nonlinear finite element analysis (NLFEA) are carried out to find out in what way and to what extent the geometric and material properties of the tube play a role in the failure of the tubes. These will be done by investigating the hoop stresses through the cross-section of the modelled flawed tubes and examining the effect of flaw geometry on failure of the tubes. The strength properties will also be varied and the effect of the flaw geometry for varied strength ratios of the flawed tubes will be assessed. Finally, using a range of failure criteria from literature and additional proposed criteria, pressures of the modelled tubes are compared to investigate which criteria could be most suitable for failure assessment of these localized thinned tubes.

4.2 Material Properties and Models

Material properties to represent a 15Mo3 low-alloy heat resistant steel boiler tube used in coal fired power plants is used for this study. The physical and strength properties are shown in Table 4.1. For this first study, material properties at room temperature are used. The effect of elevated temperature on the material properties is included in the next chapter. Two different multilinear material models are implemented in ANSYS® R19.2 [94]. In the 5% plastic strain hardening model ($M_{5\%}$), the strain is chosen such that the stress reaches σ_{uts} when the elongation is 5%. Similarly, in the 20% plastic strain hardening model ($M_{20\%}$), the strain reaches σ_{uts} when the elongation is 20%. For both models, after σ_{uts}, the response is perfectly plastic with no further work hardening allowed, as shown in Figure 4.1.

Table 4.1: Properties of the tube material

Properties	Value	Unit
Density, ρ	7.85E03	Kgm^{-3}
Coefficient of thermal expansion, α	1.2E-05	C^{-1}
Yield stress, σ_y	260	MPa
Ultimate tensile strength, σ_{uts}	500	MPa
Elastic modulus, E	212	GPa

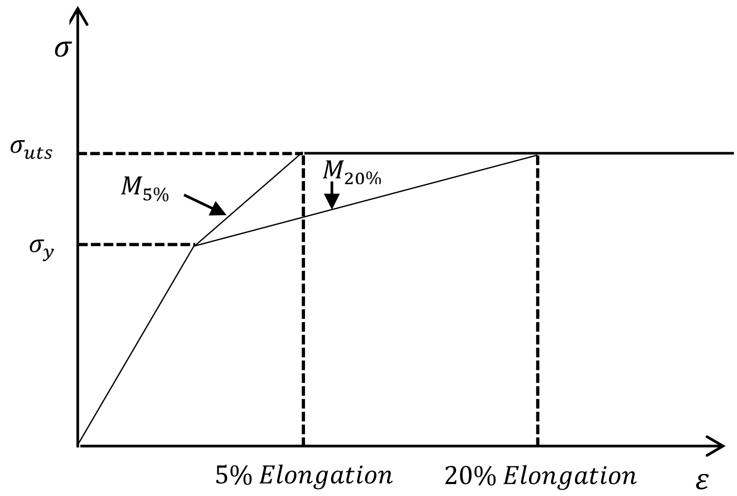

Figure 4.1: Material models used for this investigation.

4.3 Mesh, Load and Boundary Conditions

A quarter model with symmetry conditions is used in the FEM to reduce the computing time. Meshing of the model is done using mostly hexahedral elements. Body sizing control is used for the flaw area to obtain a finer mesh and soft edge sizing is used to create five sub-divisions along the edge of the model, as shown in Figure 4.2. Mesh control is used to obtain high quality results on the path created along the edge.

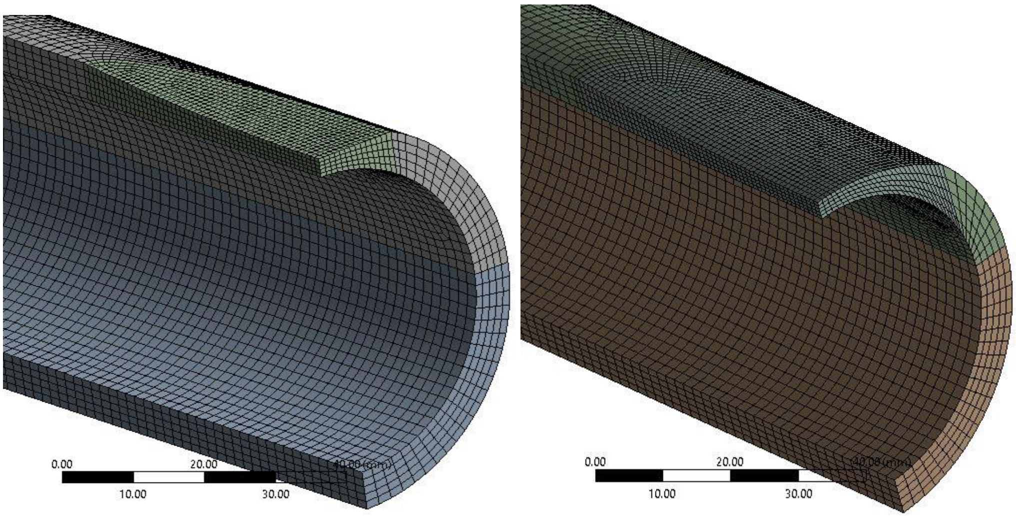

Figure 4.2: Samples of meshed u- and n-shaped flawed tubes respectively.

The maximum pressure applied as shown in Eq. (4.1) is derived from a modification of the theoretical plastic collapse pressures for flaw-free cylindrical hollow tubes [95] to account for an appropriate collapse pressure for the flawed tube based on its remaining tube thickness, t_r.

$$P_a = \frac{2}{\sqrt{3}}\sigma_{uts}\frac{t_r}{r_i} \tag{4.1}$$

where t_r and r_i are the tube remaining thickness and inner radius respectively.

The pressure is applied on the inner surface of the tube and ramped from zero to the prescribed value of P_a. Frictionless supports are applied along the symmetry boundaries of the model to prevent any form of motion and deformation in the normal direction to the applied faces. A displacement boundary condition is applied on the vertex at the lower tip of the model to prevent rigid body motion of the tube. An axial force based on P_a is applied on the far-left face of the model (furthest from the flaw) to introduce the appropriate axial stress without modeling end caps. The applied load and boundary conditions are shown in Figure 4.3. The simulations are run with a step subdivided into 20 initial/minimum sub-steps and 1000 maximum sub-steps using the ANSYS® built-in direct solver.

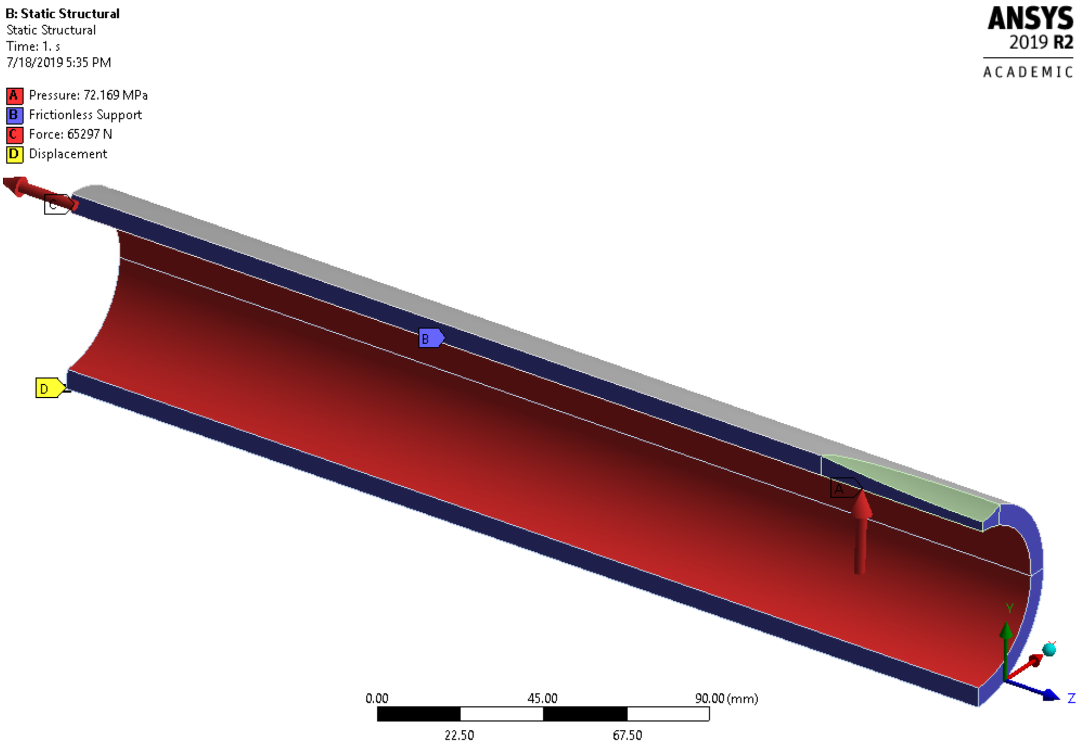

Figure 4.3: Load and boundary conditions of a u-shaped flawed tube.

4.4 Investigation of Factors Influencing the Failure of the Localized Tubes

4.4.1 Investigation of the hoop stresses through the circumferential cross-section of the modelled flaws

The n-shaped (saddle shaped) and u-shaped (scoop shaped) flaws are studied to investigate the effect of the hoop stress (σ_h) through the tube's circular cross-section. The n-shaped flaw model has the following dimensions: D_o = 60 mm, t = 6 mm, f_d = 3 mm, H = 500 mm, a = 55 mm, b = 50 mm, and z at -23 mm from the centre of the tube. The u-shaped model has the same diameter and remaining thickness but a, b and z are set at 10 mm, 33 mm and 60 mm respectively. Various paths are created from the centre of the tube to different points on the tube's circumference at small angular difference ($\theta \approx 12°$) for n-shaped flaws and for u-shaped flaws ($\theta \approx 3°$), within the flaw area but with incremental angular difference within the non-flaw area and other part of the tube cross-section, as shown in Figure 4.4 and Figure 4.5. Using the boundary conditions and applied pressure, $P_a = 72.169$ MPa (from Eq. (4.1)) for post yielding study and $P_a = 7.2169$ MPa for pre yielding study, the FEA is run to obtain hoop stresses along various paths created through the cross-section of the tube. The results obtained are shown in Figure 4.6.

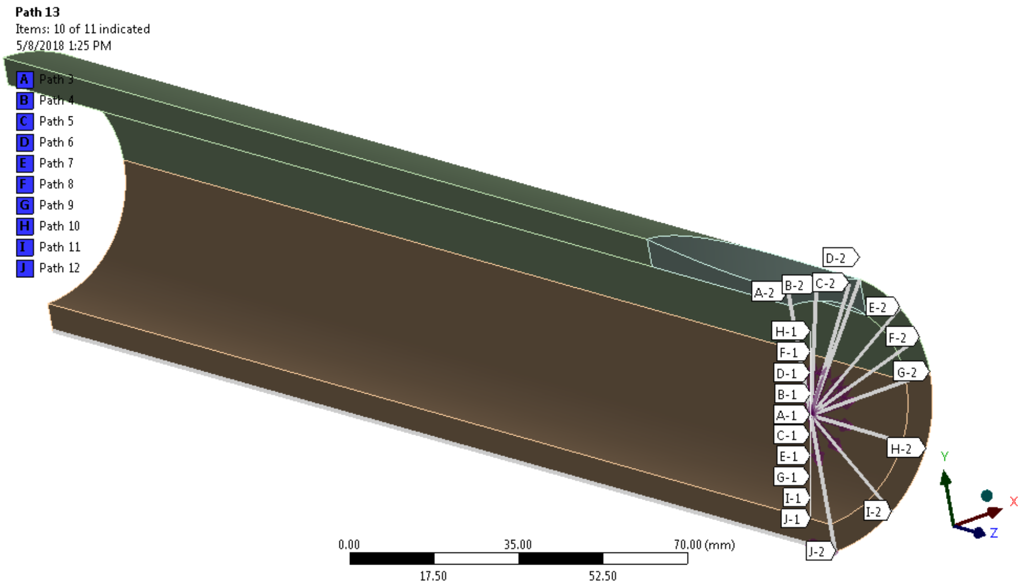

Figure 4.4: Side view of the n-shaped flawed tube showing the paths created from the centre of the tube spaced at different angles.

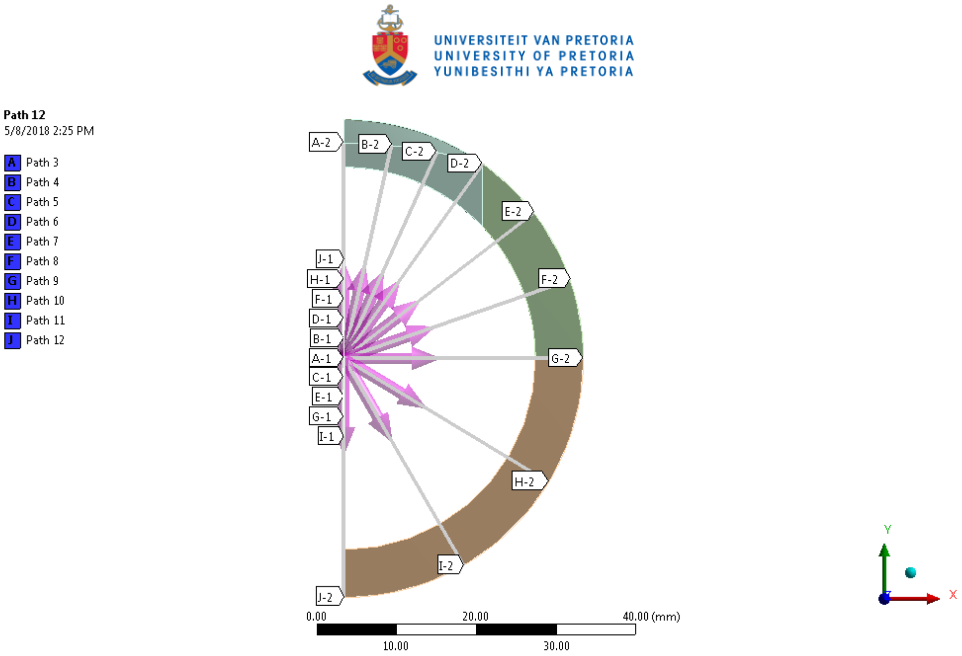

Figure 4.5: Front view of the n-shaped flawed tube showing the paths created from the centre of the tube spaced at different angles.

This analysis allows for the comparison of the stresses in the u-shaped and n-shaped flaws, when the remaining thickness, diameter and applied pressure are identical. Looking within the flaw areas of the tubes, as shown in Figure 4.6, it can be observed that the u-shaped flaw tube sustained higher hoop stresses within its flaw area compared to the n-shaped flawed tube. It can also be seen that the hoop stresses sustained by the n-shaped flawed tube are more distributed through the circumferential cross-section of the tube unlike in the u-shaped flawed tube, where the stresses are more localized and concentrated within a small part of the circumference. This implies that the n-shaped flawed tube shows the capacity of supporting more deformation prior to failure than the u-shaped flaws.

Also, when the hoop stresses, $\sigma_{h,}$ are normalized by the hoop stresses at the far field (i.e., at $\theta\ = 180°$), $\sigma_{h_{ff,}}$ as seen in Figure 4.7, the stresses before yielding peaked at a ratio of 5.1 for the u-shaped flaw and 3.25 for the n-shaped flaw. But these are redistributed due to yielding, decreasing the stress concentration within the flaw area to ratios of 2.25 and 2 for the u-shaped and n-shaped flaws respectively.

Beyond the flaw area (within the non-flaw area), it can be noticed that the stress concentration within the u-shaped tube still extends and get distributed through the circumference, as also seen with the n-shaped tube. Also, the magnitude of the stresses is reduced drastically by one-third for both flawed tubes, ascertaining the influence the localized flaw has on the tube compared to other parts. As expected, for the other part of the tube cross-section, a constant stress distribution through the circumference is observed. Prior to or after yielding, it can be noticed that both flawed tubes have similar behavior within their flaw areas, after which the stresses quickly dissipate beyond the flaw area.

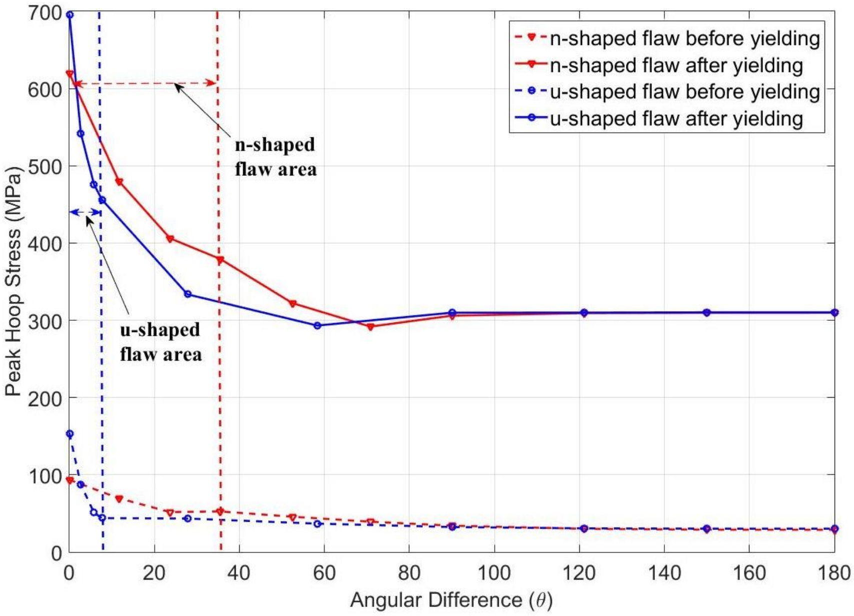

Figure 4.6: Plot showing the peak hoop stresses obtained on each path created on the tube well before and well after yielding.

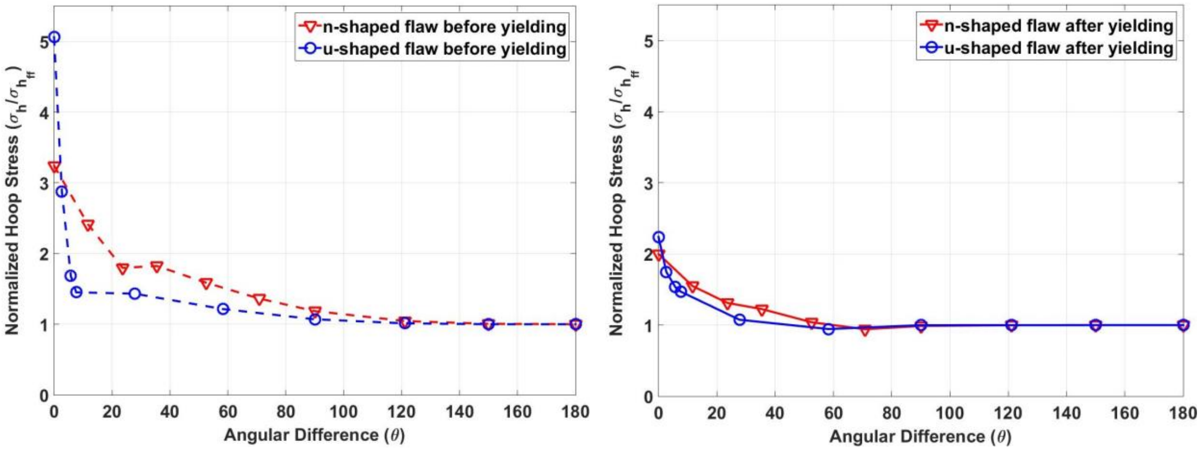

Figure 4.7: Normalized hoop stresses obtained on each path created on the u-shaped and n-shaped flawed tube (a) pre-yielding and (b) post-yielding.

4.4.2 Effect of flaw geometry on failure of the localized thinned tubes

The influence of the flaw geometry on failure of the localized thinned tubes are investigated in three different assessments, which are as follows:

1. Effect of stress concentration on the failure of the tubes.
2. Effect of the flaw aspect ratios (f_w/f_d) on failure of the tubes
3. Combined effect of the flaw width and depth variation on failure of the tubes.

Effect of stress concentration on the failure of the tubes

For the first assessment, the influence of the stress concentration on failure of the localized thinned tubes is investigated by examining the elastic stress concentration factors $(SCFs)$ for 14 modelled tubes with varied geometries. These tubes have constant flaw length (f_l) and varied flaw width (f_w) for a specific flaw depth (f_d). The dimensions of the finite element models are as follows: D_o = 100 mm, l = 300 mm t = 10 mm, f_d= 5 mm, H = 500 mm, z = 5 mm (for n-shaped) and z = 85 mm (for u-shaped), b is held constant at 40 mm, while a is varied from 52 mm to 300 mm for both u and n-shaped flaw types, as shown in Table 4.2.

The resultant geometries of the models in relation to their geometry axes and across the length of the tube can be seen in Figure 4.8, showing the effect of varying the aspect ratio of the cutting ellipse. When viewed from the end and from the side, it can be seen that the flaws modelled have varied widths and fixed constant length and depth. The models are run with loads of $0.1P_a$, ensuring that the tube remained elastic.

The elastic stress concentration factors (SCF) of the modelled tubes is computed using:

$$SCF = \frac{\text{Peak Stress}}{\text{Nominal Stress}} \tag{4.2}$$

where the peak stress is the obtained hoop stress at the deepest point of the localized flaw area in the tube and the nominal stress is given by:

$$\text{Nominal stress} = \frac{Pr_i}{t_r} \tag{4.3}$$

From the result of the hoop stress computation as seen in Table 4.2, the u-shaped tubes have higher hoop stresses within the localized areas compared to that of n-shaped ones. It can also be seen that for both flaw types, as the flaw aspect ratio increases, the hoop stress within the flaw area decreases. These observed difference in the response of both flaws indicate that first, the u-shaped flaws are more susceptible to failing before the n-shaped flaws, and second, the larger the aspect ratios of both flaw types are, the less prone to failure they become.

Table 4.2: Geometric dimensions of the investigated finite element models

FEM	a (mm)	b (mm)	f_l (mm)	f_w (mm)	f_w/f_d	Hoop Stress (MPa)
U1	52	40	134.54	33.43	6.686	107.79
U2	55	40	134.54	34.21	6.842	107.06
U3	60	40	134.54	35.34	7.068	106.04
U4	70	40	134.54	37.11	7.422	104.52
U5	85	40	134.54	38.90	7.780	103.05
U6	120	40	134.54	41.06	8.212	101.34
U7	300	40	134.54	43.16	8.632	99.76
N1	300	40	134.54	44.03	8.806	99.11
N2	120	40	134.54	46.60	9.320	97.28
N3	85	40	134.54	50.32	10.064	94.81
N4	70	40	134.54	54.88	10.976	91.98
N5	60	40	134.54	61.91	12.382	88.03
N6	55	40	134.54	69.21	13.842	84.37
N7	52	40	134.54	77.08	15.416	80.93

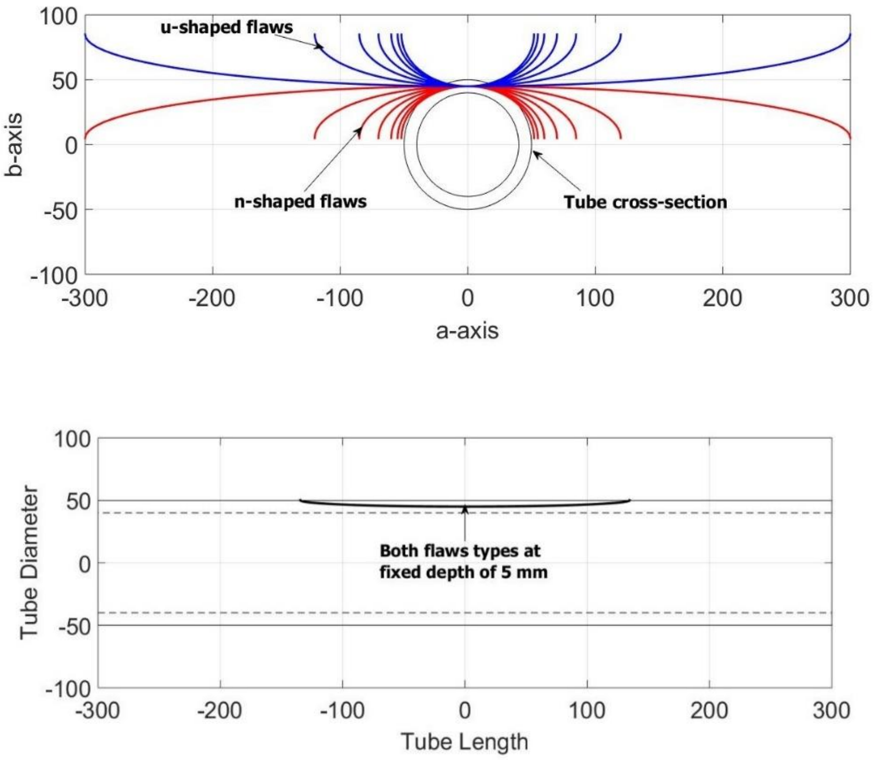

Figure 4.8: Cross-sectional view of the geometry plots of both u- and n-shaped flaws at constant flaw length and depth (above); Side view of the geometry plots for both flaws across the tube length (below).

Figure 4.9 ascertains this finding. The u-shaped tubes have higher SCF compared to their n-shaped counterparts. The SCF decreases smoothly with the f_w/f_d for both flaw types, beginning with the smallest u-shaped flaw, U1 (that has the smallest aspect ratio and highest SCF) to the largest n-shaped flaw, N7, with the largest aspect ratio and lowest SCF. This implies that within similar operating environment, the n-shaped flaws will tend to be less severe compared to the u-shaped ones. Within the family of the u-shaped flaws, the smaller ones are likely to pose more threat compared to the larger ones because of their high SCF.

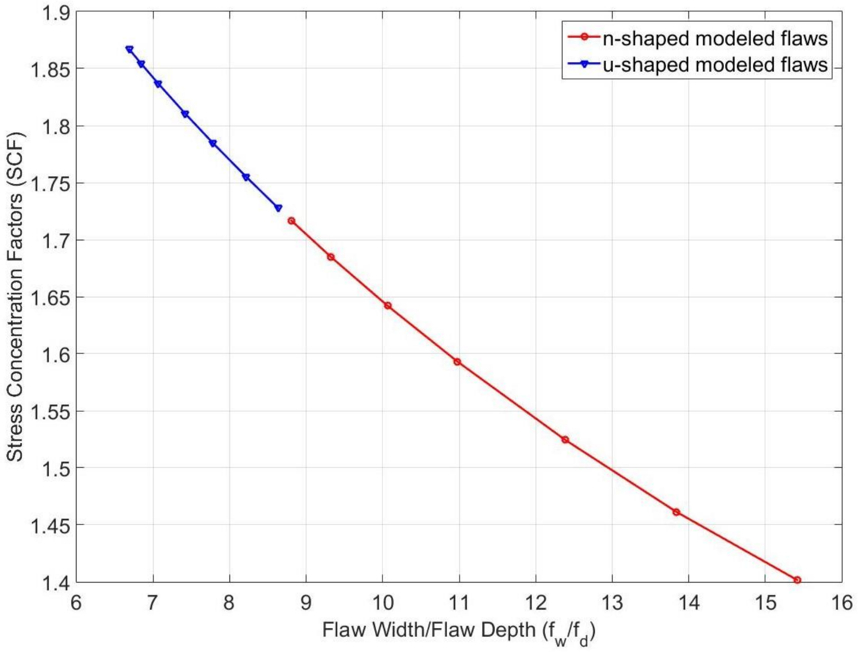

Figure 4.9: Stress concentration factors (SCF) for flaw width to depth ratios of both u- and n-shaped flaws.

Effect of the flaw aspect ratios (f_w/f_d) on failure of the localized thinned tubes

The second assessment is done to examine the effect of varying flaw width on failure of the localized thinned tubes using 24 n- and u-shaped flawed tube samples having constant f_l but varied flaw width f_w for a specific flaw depth f_d. A flat-line modelled tube sample with the same dimensions is also included. The dimensions for modelling the flawed tubes are as follows: D_o = 60 mm, t = 6 mm, l = 300 mm, f_d= 3 mm, H = 500 mm, z = -23 mm (for n-shaped) and z = 60 mm (for u-shaped), a is varied for both u and n-shaped flaw types, while b is held constant for both flaws. Figure 4.10 shows the resultant geometries of the cutting planes relative to the tube cross-section. It can be seen that both flaw types have varied widths and constant length and depths.

Table 4.3 and Table 4.4 reports the geometric dimensions of these tubes. It can be observed that the n-shaped flaws have higher shape aspect ratios compared to the u-shaped ones, with the flat line modelled flaw ratio in between them. The wide range of the flaw aspect ratios, from the smallest ratio of 2.66 for the u-shaped flaw (TSU12) to the highest ratio of 15.38 for the n-shaped flaw (TSN1), provides a broad spectrum to properly examine the effect of these varied ratios on the tubes while in plasticity.

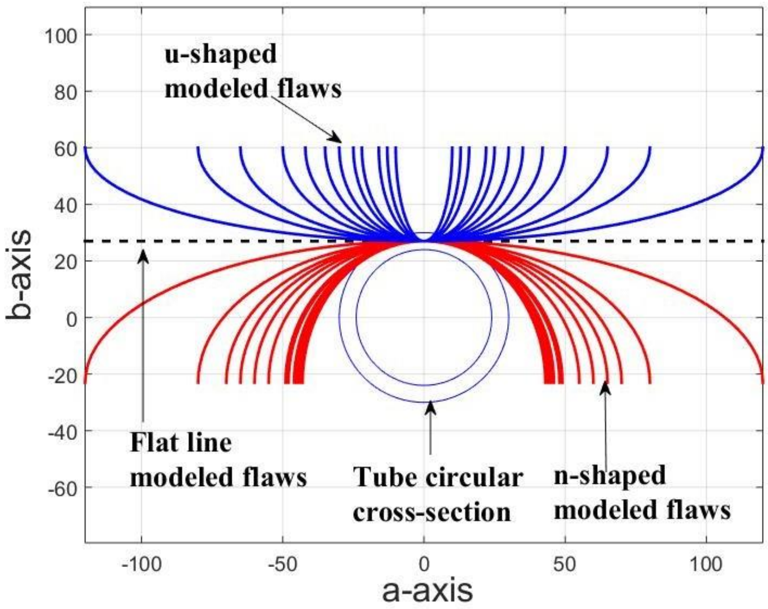

Figure 4.10: Geometric plots of the flaw widths for flat-line, n- and u-shaped flaws in relation to their shape aspect ratios.

Table 4.3: Geometric dimensions and flaw aspect ratios of n-shaped and flat-line modelled flawed tubes

Tubes no.	a (mm)	b (mm)	f_l (mm)	f_w (mm)	f_w/f_d
TSN1	43	50	106.38	46.07	15.38
TSN2	44	50	106.38	44.44	14.71
TSN3	45	50	106.38	42.99	14.29
TSN4	46	50	106.38	41.71	13.89
TSN5	48	50	106.38	39.55	13.16
TSN6	49	50	106.38	38.65	12.82
TSN7	55	50	106.38	34.83	11.63
TSN8	60	50	106.38	32.92	10.99
TSN9	65	50	106.38	31.61	10.53
TSN10	70	50	106.38	30.67	10.20
TSN11	80	50	106.38	29.41	9.80
TSN12	120	50	106.38	27.47	9.17
TSF1	N/A	N/A	106.38	26.15	8.70

Table 4.4: Geometric dimensions of u-shaped modelled flawed tubes

Tubes no.	a (mm)	b (mm)	f_l (mm)	f_w (mm)	f_w/f_d
TSU1	120	33	106.38	25.38	8.48
TSU2	80	33	106.38	24.48	8.13
TSU3	65	33	106.38	23.73	7.94
TSU4	50	33	106.38	22.37	7.46
TSU5	42	33	106.38	21.19	7.04
TSU6	35	33	106.38	19.71	6.58
TSU7	30	33	106.38	18.29	6.10
TSU8	25	33	106.38	16.49	5.50
TSU9	22	33	106.38	15.17	5.05
TSU10	16	33	106.38	11.97	3.98
TSU11	13	33	106.38	10.07	3.36
TSU12	10	33	106.38	7.97	2.66

The simulation is run using the $M_{5\%}$ material model with the maximum pressure, P_a = 72.169 MPa (obtained using Eq. (4.1)). The failure pressure is defined as the internal pressure that results in a peak plastic strain of 5%, $PP_{5\%}$. This is the point at which the stress reaches σ_{uts}. Previous literatures had reported on limit load analysis using an elastic perfectly plastic model [11,21,69,76], with some also using a 2% plastic strain, $P_{2\%}$ [64,65], as an upper limit, which were considered quite conservative. Others have also only used the σ_{uts} [56,66,68,69,96], without setting a limit on the amount of strain that should be allowed within the flaw area. In this case, we use a combination of a stress reference failure criteria set at σ_{uts} and a more realistic strain based criteria set at 5% plastic strain Figure 4.11 and Figure 4.12 show the plastic strain distribution of an example of an n-shaped and a u-shaped flaw. It can be seen that the modelled flawed tubes attained 5% plastic strain at the thinnest part of the defect.

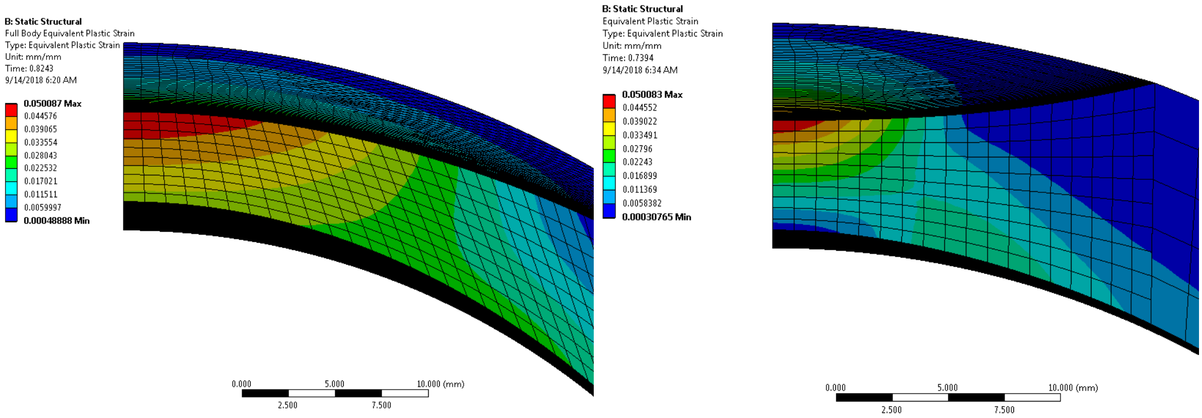

Figure 4.11: Front view of the plastic strain distribution for both the TSN7 flaw and TSU1 flaw respectively.

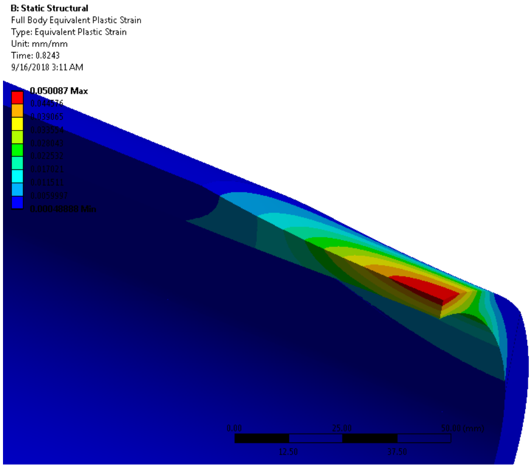

Figure 4.12: Side view of the equivalent plastic strain distribution for the TSN7 flawed tube.

Figure 4.13 shows the effect of the geometry of the modelled flaws in contributing to the failure of the tube. The failure pressure, $PP_{5\%}$, increases from a low failure pressure of 49 MPa for the u-shaped flaw with the lowest f_w/f_d ratios to a high failure pressure of 62 MPa for the n-shaped flaw with the largest flaw characteristic ratios. This indicates that n-shaped flaws will be able to withstand more pressure as they deform plastically for the same percentage elongation when compared to their u-shaped counterparts. It can also be observed that both the n- and u-shaped flaws with smaller aspect ratios tend to fail first before their larger ones, making them relatively less prone to failure. Also, it can be seen that the flat-line flaw failure behaviour is in between that of the n- and u-shaped flaws.

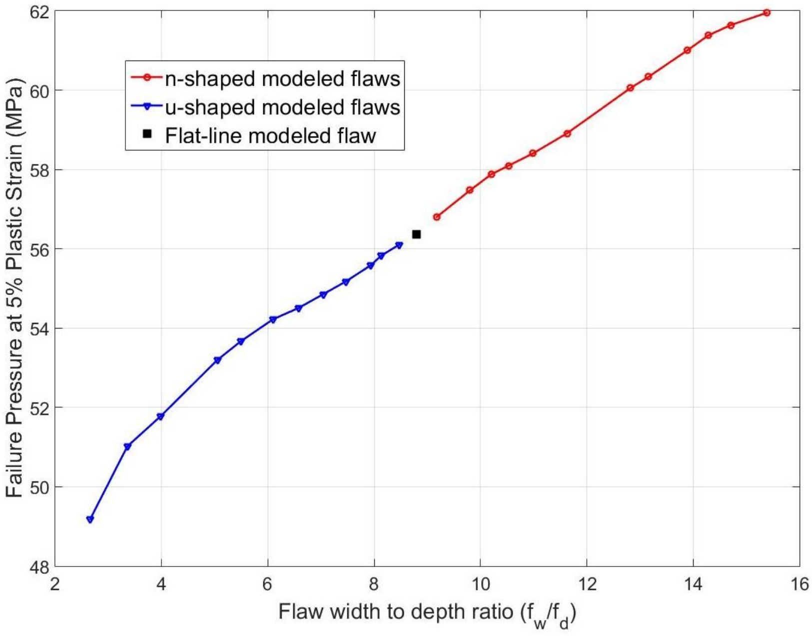

Figure 4.13: Failure pressure at 5% plastic strain for each flaw width to depth ratio of the modelled tubes at constant f_l and f_d.

As previously observed, those flaws with small aspect ratios, and less material removal, are in fact less safe than the ones with large aspect ratios and more material removal. From the outcome of the previous assessment and this second one, it can be deduced that even after the stress redistribution that occurs after yielding, the flaw geometry still significantly influences the failure of the tube.

Combined effect of the flaw length, width and depth variation on failure of the tubes

The third assessment on the flaw geometry is to investigate the combined effect of varied width and depth of the flaws on failure of the tube. This is performed by generating 10 flawed tubes with the for varied f_l, f_w and f_d. The geometric dimensions of the modelled tubes are as follows: D_o = 60 mm, t = 6 mm, l = 300 mm, H = 500 mm, with the flaw depth, f_d varied incrementally by 1 mm (from 1 mm to 5 mm), as well as z from 5 mm to 1 mm (for n-shaped) and from 62 mm to 58 mm (for u-shaped). Constant values of a and b are used for both the u-and the n- shaped modelled flaws, as shown in Table 4.5. It can be seen that as both flaw types become bigger in size in all dimensions (length, width and depth), the f_w/f_d decreases, truly capturing their effects. It can also be noticed that the u-shaped flaws have relatively smaller f_w/f_d ratios compared to the n-shaped ones for the same t_{rem}.

Table 4.5: Geometric dimensions of the investigated finite element models for varied width and depth

FEM	a (mm)	b (mm)	f_l (mm)	f_w (mm)	f_d (mm)	t_{rem}	f_w/f_d
UT1	24	33	61.35	25.74	1	0.833	9.360
UT2	24	33	86.81	35.15	2	0.667	6.590
UT3	24	33	106.38	41.53	3	0.500	5.357
UT4	24	33	122.90	46.21	4	0.333	4.620
UT5	24	33	137.48	49.75	5	0.167	4.114
NT1	33	24	61.35	9.36	1	0.833	25.740
NT2	33	24	86.81	13.18	2	0.667	17.575
NT3	33	24	106.38	16.07	3	0.500	13.843
NT4	33	24	122.90	18.48	4	0.333	11.553
NT5	33	24	137.48	20.57	5	0.167	9.950

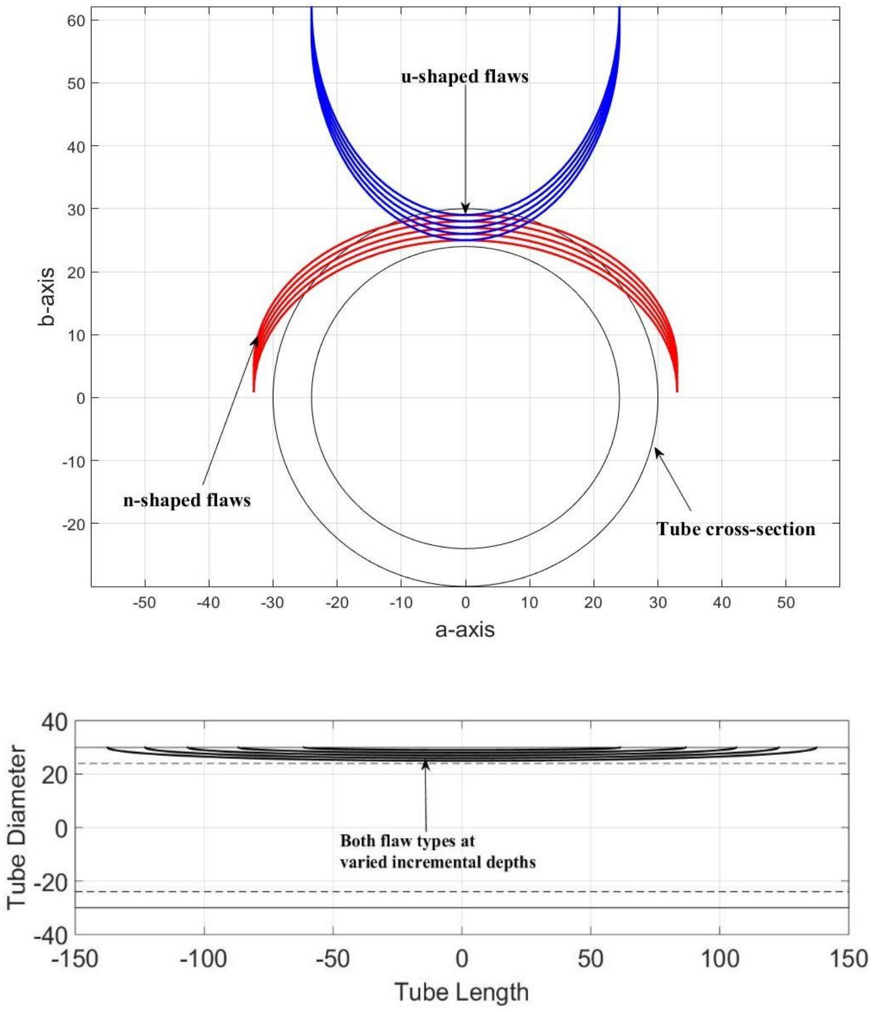

Figure 4.14: Front view of the geometry plots of both u- and n-shaped flaws for varied width and depth (above); Side view of the geometry plots for both flaws across the tube length (below).

Figure 4.14 shows the resultant geometries of the models in relation to their axes and across the length of the tube. When viewed from both sides, it can be seen that both flaw types have varied widths and incremental depths. With these tubes, the influence of the flaw width and depth in terms of (f_w/f_d) and the remaining thickness ratio (t_{rem}), which is the ratio of t_r and t, on failure of the tubes is investigated. Internal pressure computed using Eq. (4.1) and the $M_{5\%}$ material model are used for the simulation.

Figure 4.15 shows the failure pressure, $PP_{5\%}$, plotted against the remaining thickness ratio, $t_{rem.}$ A huge difference of about 80 MPa in the failure pressure between the tube with the smallest remaining thickness and the one with the largest remaining thickness can been seen, which indicates how severe the deeper flaws are compared to the shallow ones. It could also be noticed that for each flaw remaining thickness, the n-shaped flaws can relatively sustain more pressure before failure compared to the u-shaped flaws. Figure 4.16 correlates the observation in Figure 4.15. It can be observed that the u-shaped flaws in (a) failed relatively earlier than the n-shaped ones in (b), despite their larger aspect ratios. This again shows that the u-shaped flaws have a higher likelihood of failing before their n-shaped counterparts, even in scenarios of varied depths. These findings further suggest that beyond the usual amount of material removal during localized thinning of the tubes, some other factors (as shown in all the above investigations) do significantly influence the failure of the tubes.

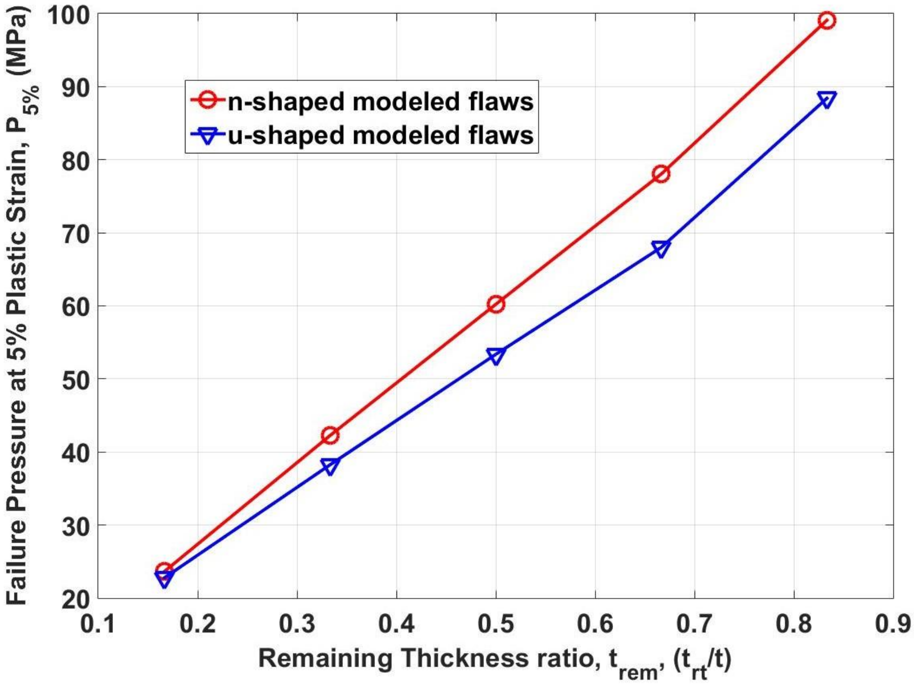

Figure 4.15: Failure pressure at 5% plastic strain for the remaining thickness ratios of both u- and n-shaped flaws

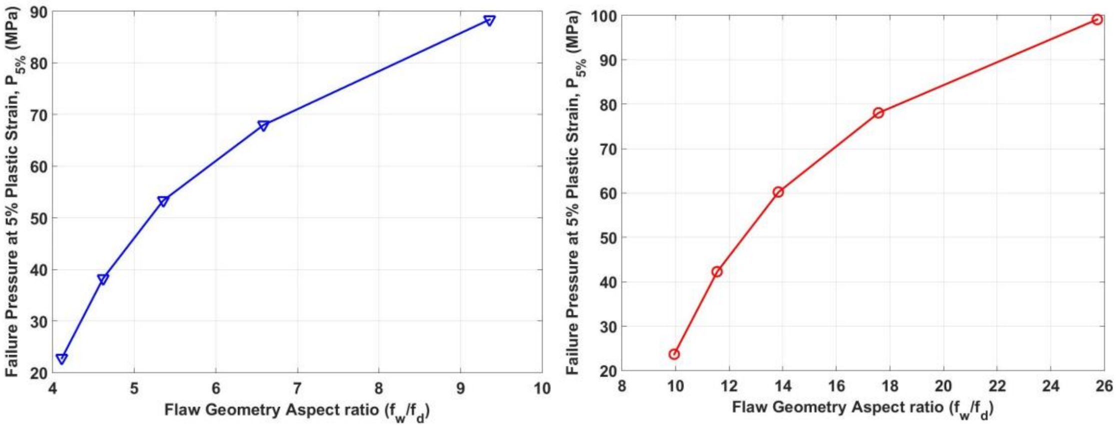

Figure 4.16: Failure pressure at 5% plastic strain for u-shaped flaw width to depth ratios; (b) Failure pressure at 5% plastic strain for n-shaped flaw width to depth ratios

In conclusion, all the studies reported under these sub-sections clearly show the effect of the flaw geometry aspect ratios and the SCF as key drivers responsible for failure of the tubes, in spite of the material removal experienced during the local thinning of the tubes. From all these assessments, it can generally be inferred that the flaw geometry along with stress redistribution that occur after yielding plays a critical role in influencing the failure of boiler tubes with localized thinning.

4.4.3 Effect of the flaw geometry on failure of the tubes for varied ratios of σ_{uts}/σ_y

To account for the influence of flaw geometry on failure of the tubes with varied strength conditions (as applicable in real scenarios), the effect of the flaw geometry for different ratios of the tube strength parameters (σ_{uts}/σ_y) are examined. By varying the σ_{uts} with respect to the σ_y as shown in Figure 4.17, the strain hardening is varied.

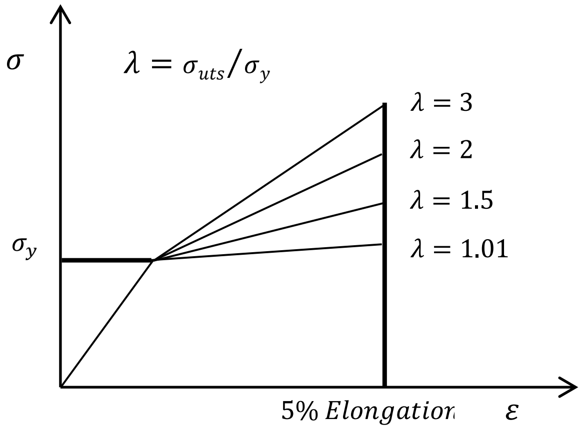

Figure 4.17: Set-up for different ratios of strength parameters of the tubes studied.

Figure 4.18 shows the same trend of the flaw aspect ratio (f_w/f_d), having a strong influence in the failure of the tubes, except for the case of the very low ratio, which is an elastic perfectly plastic approximation. As λ increases, the effect of the flaw geometry becomes more pronounced, with flaws having small aspect ratios for both flaw types, becoming more prone to failure compared to the larger flaws. It can also be noticed that as expected, the failure pressure increases as λ increases. A huge difference of 50 MPa can be observed between the closely elastic-perfectly plastic condition and the highest λ.

When the failure pressure is normalized with respect to the σ_{uts}, as seen in Figure 4.19, it will be observed that the normalized pressure gets to a high point for the elastic perfectly plastic approximation due to the stress concentration that is still locally contained at low strain hardening. But this changes as λ increases, with the normalized pressure declining, as the stresses gets more distributed within the tubes with increase in their strain hardening. It will also be noticed that the trend of each plot remains unchanged even with the normalization. This reinforces the earlier result in Figure 4.18 that the influence of geometry on the vulnerability of the flaws to failure increases with the strain hardening of the tubes.

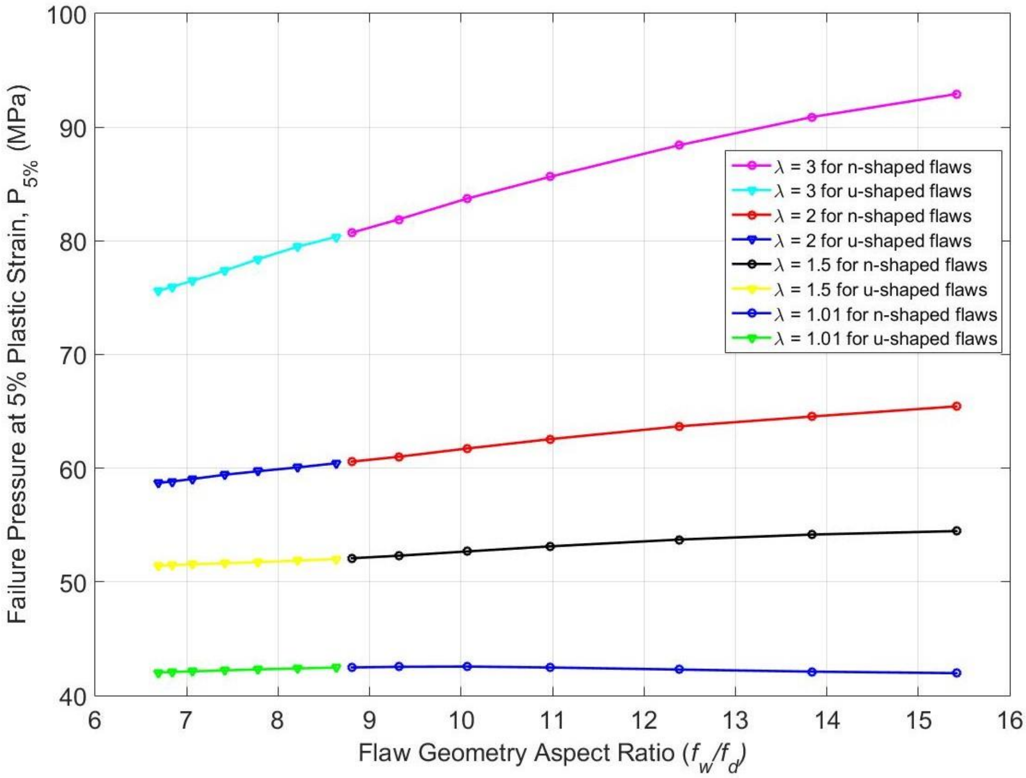

Figure 4.18: Influence of the flaw geometry on failure of the tubes for different ratios of strength parameters.

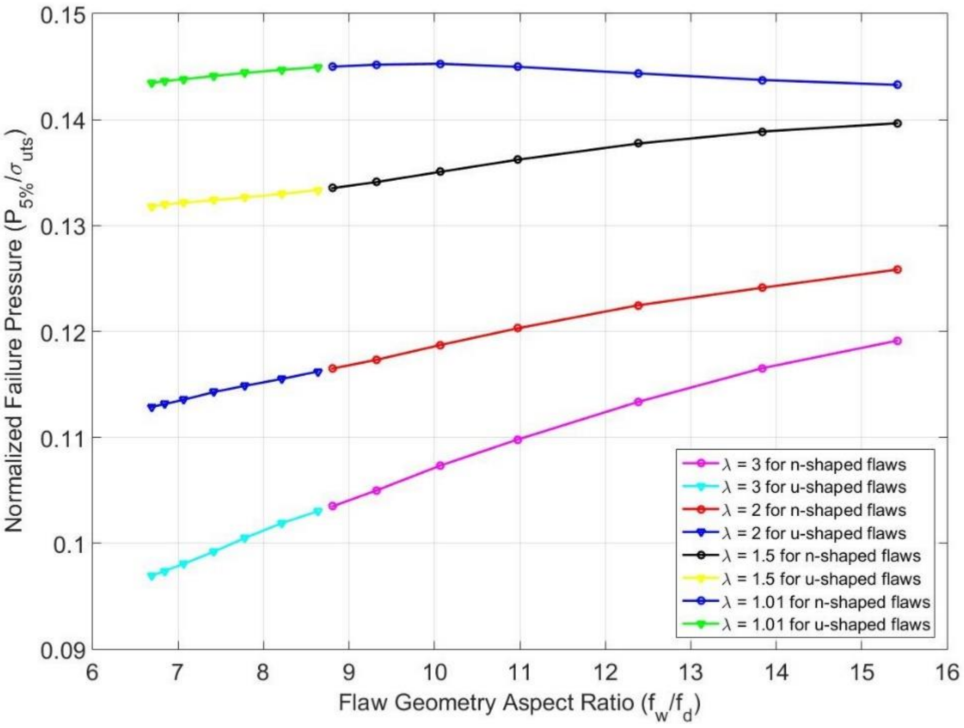

Figure 4.19: Effect of normalized failure of the tubes for different ratios of strength parameters.

The general implication of these results is that the influence of the flaw geometry on the failure of tubes transcends different strength conditions of the tube. This outcome reinforces the inference that beyond the material removal associated with the plastic deformation of the tubes during localized external erosion, the stress concentration and flaw geometry play critical roles in influencing the failure of their strength conditions.

4.5 Analysing Failure Pressures of the Tubes Based on Various Failure Criteria

Failure pressures of the modelled tubes are analysed based on some failure criteria from literature, as earlier reported in Section 2.2.2. These criteria include: The 2% plastic strain ($P_{2\%}$) [64,65], 0.9. σ_{uts} [73,76] and 0.8 σ_{uts} [76]. More criteria are proposed, which include: 20% plastic strain ($P_{20\%}$), 15% plastic strain ($P_{15\%}$), 10% plastic strain ($P_{10\%}$), 7.5% plastic strain ($P_{7.5\%}$) and 5% plastic strain ($P_{5\%}$) criteria. A large strain hardening model, the $M_{20\%}$, as described in Section 4.2 is used for this study. This is done to effectively account for the large percentage plastic strain these tubes could experience in reality. With the large strain used, it is then possible to investigate the failure pressure of these tubes using the different failure criteria so as to deduce which criteria could be most suitable for failure assessment of these localized thinned tubes.

14 modelled tubes with dimensions as described in Section 4.4.2 are run with a ramped internal pressure of $1.1P_a$ and their peak failure pressures based on each failure criteria are obtained. Figure 4.20 shows the effect of the flaw geometry on the failure of the tubes based on the criteria used. It can be first noticed that for all the failure criterion, except the lowest one $(P_{2\%})$, they follow the same pattern as had been reported from the outcome of the previous investigations done, with the n-shaped flaws generally having higher failure pressure compared the u-shaped ones.

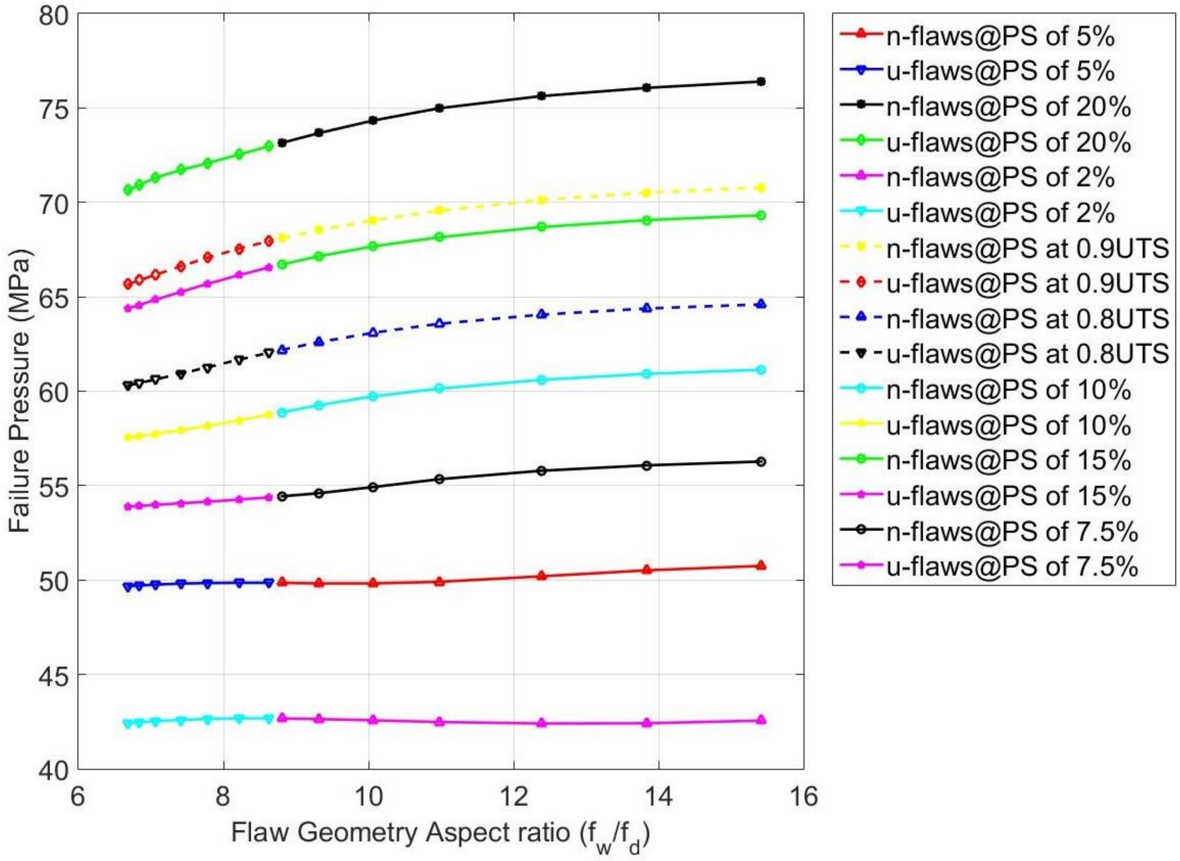

Figure 4.20: Failure pressure for different flaw geometries of modelled tubes based on various failure criteria.

It can also be observed that the $P_{2\%}$ criterion has a low failure pressure of 42.4 MPa compared to the next failure criterion $(P_{5\%})$ at 49.7 MPa, and quite so low when compared to the other failure criteria. This clearly shows how conservative the criterion is for evaluating failure of localized thinned tubes. $P_{15\%}$ and $0.9.\sigma_{uts}$ criteria have failure pressures close to the extreme benchmark criteria $(P_{20\%})$, and as such cannot be recommended to be used, as this could be risky. Between 0.8 σ_{uts} and $P_{10\%}$ criteria and the highest criterion, an average of 15-25% increase in failure pressure across all varied flaw geometries is seen. Any of these criteria seems to be a fair option to consider, but one of the aims of this study is to refrain from situations in which unexpected failures could occur, even while trying to avoid replacing tubes that could still be safe for continued operation. Hence, care must be taken to stay away from any precarious situation in which unexpected failures could possibly occur. Based on these, 0.8 σ_{uts} and $P_{10\%}$ may not be safe failure criteria to recommend. If a kind of safety factor is to be considered on the failure pressure of 0.8 σ_{uts} and $P_{10\%}$ criteria, that criterion could stand a better chance in terms of deciding to replace flawed tubes that can still be safe for continued operation or not. When this is considered, the $P_{7.5\%}$ or $P_{5\%}$ criteria could be recommended, even though there is about an average of 36-50% difference in failure pressures across all varied flaw geometries between them and the extreme benchmark criterion. Yet, they are safer options to guide against unexpected failures, while trying to also avoid being overly conservative with using the $P_{2\%}$criterion.

Although the insights gained from the above study helped to arrive at some reasonable failure criteria to consider for a more realistic failure assessment of localized boiler tubes, it will still be imperative to further investigate these using real failed tubes. This will be considered in subsequent chapters.

4.6 Summary and Conclusions

In this chapter, investigations were carried out using bilinear material models to examine the hoop stresses through the circumferential cross-section of the tube. It was observed that within the localized area of the tubes, the hoop stresses were more distributed through the circumferential cross-section of the tube for the n-shaped flawed tubes unlike in the u-shaped flawed tubes, where the stresses were more localized and concentrated within a small part of the circumference. This implied that the n-shaped flawed tube showed capacity of supporting more deformation prior to failure than the u-shaped flaws.

Also, more investigations were carried out on the models to determine the effect of the flaw geometry on failure of the tube. It was observed from the effect of the elastic stress concentration on the failure of the tubes that the SCF decreases linearly with the flaw aspect ratios (f_w/f_d) for both variants of flaw types, beginning with the smallest u-shaped flaw (that had the smallest aspect ratio and highest SCF) to the largest n-shaped flaw with the largest aspect ratio and lowest SCF. The implication of this is that within similar operating environment, the u-shaped flaws will tend to be more severe compared to the n-shaped ones. Within the family of the u-shaped flaws, the smaller flaws are likely to pose more threat compared to the larger ones because of their high SCF.

A study on the effect of the flaw aspect ratios on the failure of the tubes while they deform using different geometry offset values for n-shape flaws (which usually experience more material removal) showed that the u-shaped flawed tubes failed quicker compared to the n-shaped ones with more material removal. The n-shaped flawed tubes could withstand more pressure as they deform plastically for the same percentage plastic strain than their u-shaped counterparts. It was also observed that both flaws had high failure pressures for large flaw aspect ratios, and as these ratios decreases, the failure pressure decreases. One would have expected those flaws with small aspect ratios to be safer but contrary to that, they turned out to pose more threat compared to the ones with large aspect ratios that suffer more material removal.

Investigation on the combined effect of the flaw width and depth variation on failure of the tubes also showed that u-shaped flaws had relatively lower failure pressure compared to the n-shaped ones and as such will fail quicker. It was observed that for each flaw remaining thickness, the n-shaped flaws can relatively sustain more pressure before failure compared to the u-shaped flaws.

The effect of the flaw geometry on the failure of the tubes for different σ_{uts}/σ_y ratios revealed that the u-shaped flaws were more susceptible to failure compared to the n-shaped flaws for different σ_{uts}/σ_y ratios, except for the case of the very low ratio, which was almost elastic perfectly plastic. Also, the flaws with smaller aspect ratios for both flaw types were more prone to failure compared to the flaws with larger aspect ratios. The implication from this investigation shows that the influence of the flaw geometry on failure tubes transcends different strength conditions of the tube.

All the above outcomes from the investigations infer that beyond the material removal associated with the plastic deformation of the tubes during localized external erosion, the stress concentration and flaw geometry do play critical roles in influencing the failure of the tubes while in service.

Using several failure criteria, obtained failure pressures of the modelled tubes were analysed to determine which failure criteria will be best suited for the failure assessment of these localized tubes. From the results obtained, $P_{7.5\%}$ or $P_{5\%}$ criteria were recommended because they had lower pressures that were reasonably safe from the extreme benchmark failure criterion of $P_{20\%}$, and as such were safer options to guide against unexpected failures of the tubes, while trying to also avoid being overly conservative with using the lower $P_{2\%}$criterion.

Having performed these series of investigative studies to determine the factors that could influence the failure of boiler tubes under localized external erosion, the insights gained from these studies carried out on conceptualized variants of localized thinned tubes will now be extended to real localized eroded tubes obtained from industry. This will be used to develop an improved and efficient failure assessment methodology framework for heat resistant seamless tubes while in service. The development of this methodology framework beginning with a description of the realistic material modes used, will be discussed in the next chapter.

5 REALISTIC MATERIAL MODELS FOR ASSESSMENT OF REAL TUBES WITH LOCALIZED EROSION DEFECTS

5.1 Introduction

Real scenarios of localized external erosion in boiler tubes are needed to develop a more efficient and less expensive fitness-for service methodology. This could be used to avoid replacing tubes that could still be safe for continued operation, while also guarding against unexpected failure of tubes, their emergency costly repairs and forced outages. In this chapter, the outcome of detailed research conducted on the strength and physical properties of commonly used heat resistant tubes while in operation (under high temperature and pressure environment) is reported. Real tubes which failed due to localized thinning are used as case studies for this study. A discussion on the development of two material models based on the American Petroleum Institute and the American Society of Mechanical Engineers and (API-ASME) is presented.

5.2 Real Failed Tubes used for this Study

A range of heat resistant seamless steel boiler tubes that failed due to localized thinning obtained from industry is used for this study [93]. Table 5.1 provides an overview of their grades and dimensions.

Table 5.1: Grades and dimensions of heat resistant seamless tubes used for this study

Tube No	Tube Grades	D_o (mm)	t (mm)	t_r (mm)	f_l (mm)	f_w (mm)
1.	BS 3059 Grade 360	75.0	7.0	0.50	600	20
2.	BS 3059 Grade 360	50.8	4.4	0.30	80	25
3.	BS 3059 Grade 360	50.8	4.4	0.17	70	40
4.	SA 210 A1	47.5	5.4	1.20	400	45
5.	SA 210 A1	50.8	6.3	0.38	150	50
6.	BS 3059 Grade 440	63.5	6.6	0.80	240	30
7.	BS 3059 Grade 440	38.0	3.8	0.30	155	32
8.	BS 3059 Grade 440	38.0	3.8	0.30	110	28
9.	BS 3059 Grade 440	63.5	6.1	0.63	600	50
10.	BS 3059 Grade 440	63.0	5.4	0.42	310	60
11.	BS 3059 Grade 440	38.0	3.8	0.45	500	35
12.	DIN 17175 15Mo3	33.0	3.6	0.20	20	15
13.	DIN 17175 15Mo3	44.5	5.6	0.41	225	35
14.	DIN 17175 15Mo3	33.9	6.5	0.24	300	30
15.	DIN 17175 15Mo3	44.5	5.2	0.50	140	44
16.	BS 3059 Grade 620	34.9	4.2	0.20	300	30

5.3 Material Properties of Tubes

The strength and physical properties of the tubes used for this study, which operate within high temperature and pressure environments are examined.

5.3.1 Strength properties

The heat resistant tubes are categorized into four main steel groups based on their material composition. The strength properties of these tubes with their equivalent international standards obtained from handbooks and design standards [97–104] are shown in Table 5.2. These standards include: DIN **(**Standard of the German Institute for Standardization), BS (British Standard), EN (European Standard) and ASTM/ASME (both American Standards).

Table 5.2: Yield and tensile strengths for heat resistant seamless tubes used for the study.

Steel Type	Heat Resistant Seamless Steel Tubes and their Equivalent International Standards		
	Tube Standard Types and Grades	Minimum σ_y (MPa)	σ_{uts} (MPa)
Carbon Steel	DIN 17175 Gr. St 35.8	235	360 - 480
	BS 3059: Part 2 Gr. 360	235	360 - 500
	EN 10216 Part 2 Gr. P235GH	235	360 - 500
	*ASTM/ASME A/SA 192	180	325
Medium Carbon Steel	DIN 17175 Gr. St 45.8	255	410 - 530
	BS 3059: Part 2 Gr. 440	245	440 - 580
	EN 10216 Part 2 Gr. P265GH	265	410 - 570
	ASTM/ASME A/SA 210 Gr. A1	255	415
Carbon-Molybdenum Alloy Steel (C-1/4Mo and C-1/2Mo)	DIN 17175 Gr. 15Mo3	270	450 - 600
	BS 3059: Part 2 Gr. 243	275	480 - 630
	EN 10216 Part 2 Gr. 16Mo3	280	450 - 600
	ASTM/ASME A/SA 209 Gr. T1	207	380
Chromium-Molybdenum Alloy Steel (1Cr-1/2Mo)	DIN 17175 Gr. 13CrMo4-4	290	440 - 590
	BS 3059: Part 2 Gr. 620	180	460 - 610
	EN 10216 Part 2 Gr. 13CrMo4-5	290	440 - 590
	ASTM/ASME A/SA 213 Gr. T12	220	415

*ASTM/ASME A/SA signifies ASTM and ASME standard steel grade names respectively

Considering the effect of temperature on the strength properties of the tubes while in operation, three different approaches are used to examine the dependency of the materials yield strength (σ_y) and ultimate tensile strengths (σ_{uts}) with temperature. The first approach is to use the strength values as they varied with temperature directly from the handbooks and design standards. The second approach is to use the analytical expressions for the minimum specified yield (*MSYS*) and tensile strength (*MSUTS)* values as a function of temperature, documented in the material properties section of the FFS standard [33]. The third approach is to use the minimum σ_y and σ_{uts} values as a function of temperature obtained from data in API STD 530 [105] and documented in the material properties section of the FFS standard [33]. It is necessary to use these different approaches because of the intricate nature of the case of localized thinning considered in this study, which has to do with assessing the integrity of degrading structural components (boiler tubes) while in-service. Exploring the use of these approaches will help us evaluate the strength of these localized thinned tubes as a function of temperature from different perspectives.

First Approach: For this approach, only the σ_y variation with temperature is reported as provided by the handbooks and standards [97–104], with the exception of ASME that also provides the σ_{uts} temperature variation. The σ_{uts} with respect to temperature as reported by ASME is constant from room temperature to 350 – 370 ℃ for all tubes, after which their strengths degrade slowly [102]. The σ_y of the tubes studied at various operating temperatures are computed by interpolating between the strength values at two bounding temperatures to obtain the specific value for each operating temperature considered. Table 5.3 summarizes the σ_y values of the tube grades studied (having wall thickness ≤ 16 mm) at room temperature (T_{rt}) and their operating temperatures (T_{ot}).

Table 5.3: Yield strengths of specific tubes studied at T_{rt} and T_{ot} with their equivalent international standards using the First Approach.

Steel Type	Tube No	Heat Resistant Seamless Steel Tubes with their Equivalent International Standards			
		Tube Standard Types and Grades	σ_y (MPa) at T_{rt}	Operating Temp. (℃)	σ_y (MPa) at T_{ot}
Carbon Steel	1.	***BS 3059: Part 2 Gr. 360**	**235**	**384**	**114.56**
		DIN 17175 Gr. St35.8	235	384	113.20
		EN 10216 Part 2 Gr. P235GH	235	384	114.56
		ASTM/ASME A/SA 192	180	384	126.52
	2.	**BS 3059: Part 2 Gr. 360**	**235**	**358**	**118.72**
		DIN 17175 Gr. St35.8	235	358	118.40
		EN 10216 Part 2 Gr. P235GH	235	358	118.72
		ASTM/ASME A/SA 192	180	358	130.52
Medium Carbon Steel	3.	**ASTM/ASME A/SA 210 Gr. A1**	**255**	**400**	**176.30**
		BS 3059: Part 2 Gr. 440	245	400	150.00
		EN 10216 Part 2 Gr. P265GH	265	400	134.00
		DIN 17175 Gr. St 45.8	255	400	130.00
	4.	**ASTM/ASME A/SA 210 Gr. A1**	**255**	**390**	**178.50**
		BS 3059: Part 2 Gr. 440	245	390	151.60
		EN 10216 Part 2 Gr. P265GH	265	390	135.40
		DIN 17175 Gr. St 45.8	255	390	132.00
	5.	**BS 3059/45 or BS 3059: Part 2 Gr. 440**	**245**	**417**	**146.60**
		EN 10216 Part 2 Gr. P265GH	265	417	131.96
		DIN 17175 Gr. St 45.8	255	417	128.30
		ASTM/ASME A/SA 210 Gr. A1	255	417	172.91

Medium Carbon Steel	6.	**BS 3059/45 or BS 3059: Part 2 Gr. 440**	**245**	**367**	**155.28**
		EN 10216 Part 2 Gr. P265GH	265	367	138.62
		DIN 17175 Gr. St 45.8	255	367	136.60
		ASTM/ASME A/SA 210 Gr. A1	255	367	183.63
	7.	**BS 3059: Part 2 Gr. 440**	**245**	**333**	**163.10**
		EN 10216 Part 2 Gr. P265GH	265	333	145.42
		DIN 17175 Gr. St 45.8	255	333	146.80
		ASTM/ASME A/SA 210 Gr. A1	255	333	191.47
	8.	**BS 3059: Part 2 Gr. 440**	**245**	**350**	**158.00**
		EN 10216 Part 2 Gr. P265GH	265	350	141.00
		DIN 17175 Gr. St 45.8	255	350	140.00
		ASTM/ASME A/SA 210 Gr. A1	255	350	187.43
	9.	**BS 3059: Part 2 Gr. 440**	**245**	**250**	**195.00**
		EN 10216 Part 2 Gr. P265GH	265	250	171.00
		DIN 17175 Gr. St 45.8	255	250	185.00
		ASTM/ASME A/SA 210 Gr. A1	255	250	216.91
Carbon-Molybdenum Alloy Steel (C-1/4Mo and C-1/2Mo)	10.	**DIN 17175 Gr. 15Mo3**	**270**	**414**	**158.60**
		EN 10216 Part 2 Gr. 16Mo3	280	414	158.60
		BS 3059: Part 2 Gr. 243	275	414	174.88
		ASTM/ASME A/SA 209 Gr. T1	207	414	156.64
	11.	**DIN 17175 Gr. 15Mo3**	**270**	**370**	**166.00**
		EN 10216 Part 2 Gr. 16Mo3	280	370	157.80
		BS 3059: Part 2 Gr. 243	275	370	178.40
		ASTM/ASME A/SA 209 Gr. T1	207	370	162.85
	12.	**DIN 17175 Gr. 15Mo3**	**270**	**400**	**160.00**
		EN 10216 Part 2 Gr. 16Mo3	280	400	156.00
		BS 3059: Part 2 Gr. 243	275	400	176.00
		ASTM/ASME A/SA 209 Gr. T1	207	400	159.08
	13.	**DIN 17175 Gr. 15Mo3**	**270**	**405**	**159.50**
		EN 10216 Part 2 Gr. 16Mo3	280	405	155.40
		BS 3059: Part 2 Gr. 243	275	405	175.60
		ASTM/ASME A/SA 209 Gr. T1	207	405	158.21
Chromium-Molybdenum Alloy Steel (1Cr-1/2Mo)	14.	**BS 3059: Part 2 Gr. 620**	**180**	**431**	**176.28**
		DIN 17175 Gr. 13CrMo4-4	290	431	183.80
		EN 10216 Part 2 Gr. 13CrMo4-5	290	431	170.28
		ASTM/ASME A/SA 213 Gr. T12	220	431	157.34

*The bold entries are the specific tubes obtained from the study and used for this case study.

Second Approach: The *MSYS* and *MSUTS* values as a function of temperature are obtained from the material properties section of the FFS [33] using the analytical equations follow from:

$$\sigma_y = \sigma_y^{rt} \exp[C_0 + C_1 T + C_2 T^2 + C_3 T^3 + C_4 T^4 + C_5 T^5] \text{ (°C, MPa)} \tag{5.1}$$

$$\sigma_{uts} = \sigma_{uts}^{rt} \exp[C_0 + C_1 T + C_2 T^2 + C_3 T^3 + C_4 T^4 + C_5 T^5] \text{ (°C, MPa)} \tag{5.2}$$

where σ_y^{rt} and σ_{uts}^{rt} are the *MSYS* and *MSUTS* values at room temperature, and $C_0 \rightarrow C_5$ are given material coefficients for computing the σ_y and σ_{uts}, and T is the temperature.

For the computation of the *MSYS* as a function of temperature, the coefficients used for each steel type as provided in the FFS and seen in Appendix C. For the *MSUTS* computation as a function of temperature, the coefficients used for each steel type can be seen in Appendix D.

Third Approach: The σ_y and σ_{uts} values as a function of temperature are obtained from analytical equations based on the data provided in API STD 530 and documented in the material properties section of the FFS [33]. The expressions are:

$$\sigma_y = \sigma_y^{T_{min}} \exp[A_0 + A_1T + A_2T^2 + A_3T^3 + A_4T^4 + A_5T^5] \; (°\mathrm{F}, \mathrm{MPa}) \tag{5.3}$$

$$\sigma_{uts} = \sigma_{uts}^{T_{min}} \exp[B_0 + B_1T + B_2T^2 + B_3T^3 + B_4T^4 + B_5T^5] \; (°\mathrm{F}, \mathrm{MPa}) \tag{5.4}$$

where $\sigma_y^{T_{min}}$ and $\sigma_{uts}^{T_{min}}$ are values of the specified σ_y and σ_{uts} values (which could be minimum, average, maximum as desired) at the minimum temperature limit defined in Appendix E, $A_0 \rightarrow A_5$ and $B_0 \rightarrow B_5$ are given material coefficients for computing σ_y and σ_{uts} as can been seen in Appendix E, and T is the temperature.

Results of the computed σ_y and σ_{uts} values at various operating temperatures using the first, second and third approaches are shown in Table 5.4. From Table 5.4, it is observed that the second approach gives higher yield strength values for all tube types except for the BS 3059 Gr. 620, while the first and third approaches provide relatively close strength values at yield. Following this observation, only the tensile strengths for the second and third approaches are computed as reported in Table 5.5. From the table, it is observed that the two approaches produced fairly close tensile strengths for the carbon steel tubes, while those of the medium carbon steel and chromium-molybdenum steel differ by about 20-50 MPa. It is also observed that the second approach strength values are lower in comparison to those of the third approach, except for the DIN tubes that have higher values. The unique strength values obtained from these two approaches necessitated using both for the failure assessment study.

Table 5.4: Tubes yield strengths using the First, Second and Third Approaches.

Tube Grades	Min. σ_y (MPa) at T_{rt}	T_{ot} (°C)	σ_y (MPa) at T_{ot} computed using First Approach	σ_y (MPa) at T_{ot} computed using Second Approach	σ_y (MPa) at T_{ot} computed using Third Approach
BS 3059 Grade 360	235	384	114.56	170.08	120.18
BS 3059 Grade 360	235	358	118.72	173.96	123.20
SA 210 A1	255	400	176.30	181.91	159.11
SA 210 A1	255	390	178.49	183.56	160.91
BS 3059 Grade 440	245	417	146.60	172.03	155.81
BS 3059 Grade 440	245	367	155.28	179.97	164.70
BS 3059 Grade 440	245	333	163.10	185.17	169.72
BS 3059 Grade 440	245	350	158.00	182.59	167.27
BS 3059 Grade 440	245	250	195.00	197.33	182.40
DIN 17175 15Mo3	270	414	158.60	240.27	156.75
DIN 17175 15Mo3	270	370	166.00	242.32	162.66
DIN 17175 15Mo3	270	400	160.00	241.17	158.74
DIN 17175 15Mo3	270	405	159.50	240.88	158.00
BS 3059 Grade 620	180	431	176.28	143.24	150.97

Table 5.5: Tubes tensile strengths using the Second and Third Approaches.

Tube Grades	Min. σ_{uts} (MPa) at T_{rt}	T_{ot} (°C)	σ_{uts} (MPa) at T_{ot} computed using Second Approach	σ_{uts} (MPa) at T_{ot} computed using Third Approach
BS 3059 Grade 360	360	384	260.54	276.09
BS 3059 Grade 360	360	358	266.49	288.66
SA 210 A1	415	400	296.04	340.31
SA 210 A1	415	390	298.74	347.84
BS 3059 Grade 440	360	417	308.95	326.29
BS 3059 Grade 440	360	367	323.22	363.00
BS 3059 Grade 440	440	333	332.55	379.79
BS 3059 Grade 440	440	350	327.92	372.24
BS 3059 Grade 440	440	250	354.39	393.98
DIN 17175 15Mo3	450	414	400.45	359.66
DIN 17175 15Mo3	450	370	403.87	383.78
DIN 17175 15Mo3	450	400	401.95	367.60
DIN 17175 15Mo3	450	405	401.46	364.79
BS 3059 Grade 620	460	431	366.07	386.12

5.3.2 Physical properties

The tubes studied are all heat resistant tubes, therefore their physical properties are similar. Tube density, ρ = 7850 Kgm^{-3}, and Poisson ratio, v = 0.3 used are the same for all tubes, obtained from BS 3059: Part 2, Appendix C [99]. The coefficient of thermal expansion, α, and the Young's modulus of elasticity, E, with respect to temperature change for all tubes are shown in Table 5.6.

Table 5.6: Physical properties of the tubes with respect to temperature change.

Temperature (°C)	α ($\times 10^{-6}$ °C^{-1})	E (GPa)
20	*11.50	212
100	11.90	206
200	12.60	198
300	13.10	191
400	13.70	183
500	14.10	174

*The α value at room temperature is obtained from ASME [102], as the BS Standard does not provide it.

5.4 Material models

The Material Properties Council (MPC) stress-strain curve model from the API-ASME FFS [33] is used for this assessment study. This allows the development of a realistic work hardening using only information from the material datasheets. The effect of strain hardening in the tubes as they deform is properly captured and appropriately considered. Previous studies had not taken this into consideration [84–86] and some had used elastic-perfectly plastic models [11,55,64,65]. The guideline of how to use the MPC model to produce a true stress-strain hardening curve for the simulation is shown in Appendix F. This is effected in MATLAB® [92] to develop the curve from zero to the true ultimate tensile strain $(\varepsilon_{t,uts})$ using the derived strength properties (from the second and third approach) and an engineering strain value (ε). The plastic region of the developed stress-strain curves is implemented in ANSYS® [94] using the multilinear isotropic hardening toolbox of the engineering data for static structural analysis.

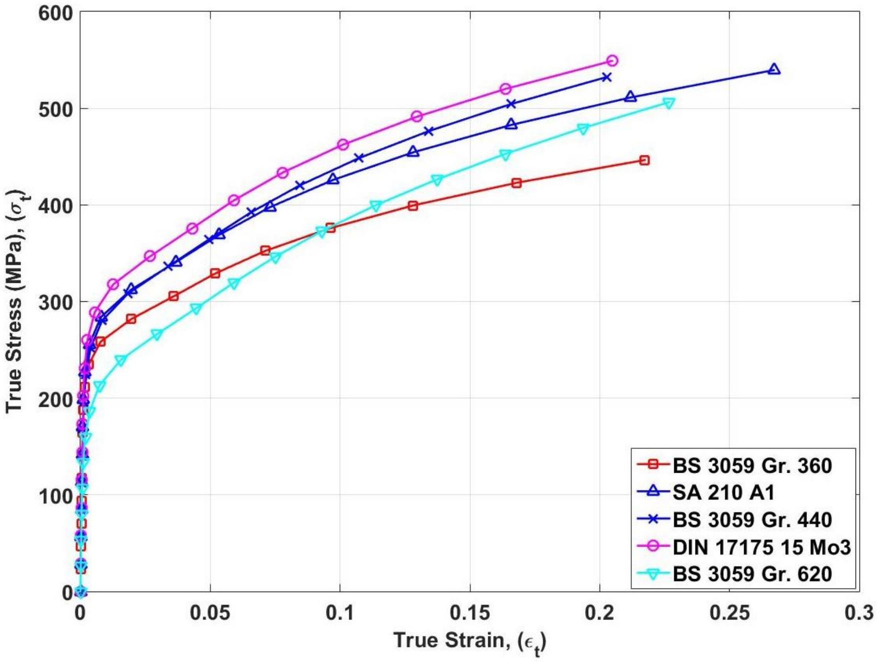

Figure 5.1: True stress strain curve for the various grades of tubes at room temperature T_{rt}.

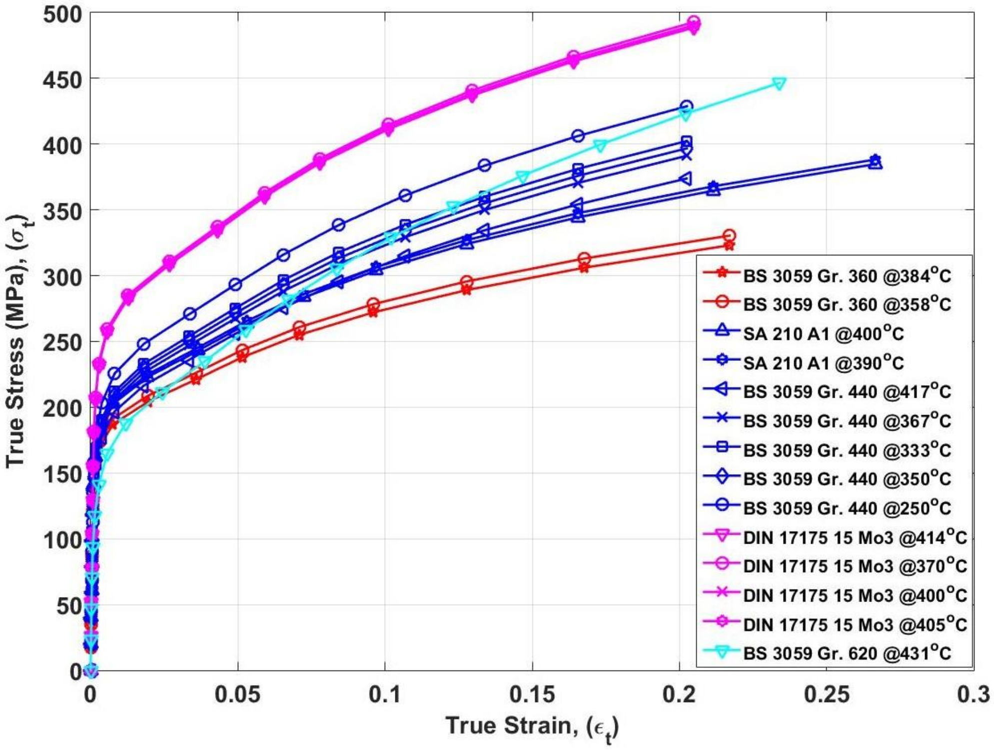

Figure 5.2: True stress strain curve for the various tubes at T_{ot} using the second approach.

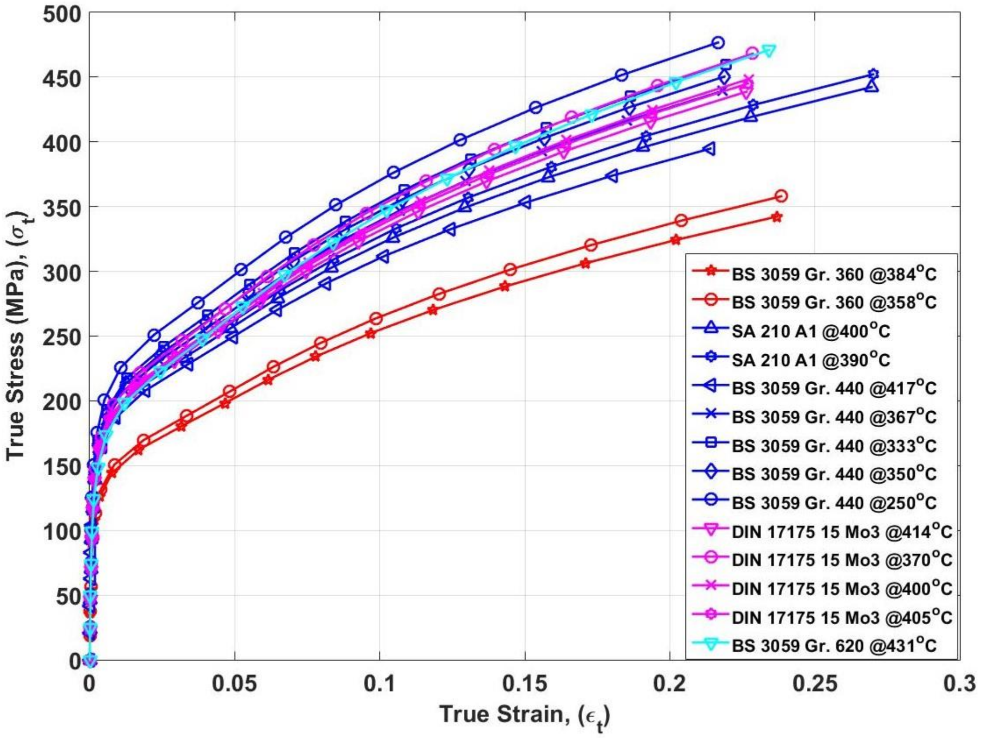

Figure 5.3: True stress strain curve for the various tubes at T_{ot} using the third approach.

Figure 5.1 shows the true stress-strain curves of different grades of the steel tubes at room temperature. The SA 210 A1 tube is seen to have the largest strain of 0.267 at room temperature and the BS 3059 Grade 440 has the lowest strain of 0.203. Figure 5.2 and Figure 5.3 show the true stress-strain curves for various operating temperatures using the second and third approach strength property values, respectively. The strength degradation for the different tubes from T_{rt} to their various T_{ots} can be noticed in Figure 5.2 and Figure 5.3.

From the second approach model in Figure 5.2, the pattern of strength deterioration for all the tubes at T_{rt} and T_{ot} appear to be well aligned compared to those of the third approach model in Figure 5.3. Also, in Figure 5.2, the variance in the strength of the tubes at T_{rt} and T_{ot} are most pronounced with the medium carbon tubes, having a difference of about 150 MPa in between their T_{rt} and T_{ots} for the SA 210 tubes and 105-160 MPa for the BS 3059 440 tubes. This is followed by the BS 3059 360 tubes that have an approximate difference of 120 MPa in between these temperatures. The 15 Mo3 and BS 3059 620 tubes have a difference of about 60 MPa in between their T_{rt} and T_{ots}. It can also be seen that the true stress–strain curves for the different grades of tubes at T_{ot} using this approach show some similarity in form with those of the T_{rt}.

In contrast, the third approach material model results depicted in Figure 5.3 show a repositioning of the true stress-strain curve, such that the carbon steel tubes are distinctly separated from the other tubes. It is also observed that when compared with the second approach, the third approach curves have narrower elastic region and the true stresses are relatively higher for all tube grades except for the 15 Mo3, making the model more conservative for most of the tube grades. Since the stresses continue to increase as the strains increase, the tubes have the potential to work harden during plastic flow. Hence, the combination of the distinctive attributes of these two models (a second approach model that is less conservative and a conservative third approach model) forms an all-inclusive model for a comprehensive assessment of localized externally eroded tubes.

5.5 Summary and Conclusions

The initial procedures that are employed to develop a failure assessment methodology framework for heat resistant seamless steel boiler tubes with localized external erosions was presented in this chapter. First, a detailed assessment of the strength and physical properties of a range of heat resistant boiler tubes commonly used in fossil-fuel industries, operating within high temperature and pressure environment while in service was carried out. The study involved the use of various handbooks and standards (BS, DIN, EN, ASTM, ASMI and API-ASME FFS), which led to the adoption of two unique material properties approaches for 16 different tube grades used to develop the assessment framework. The material properties of these localized thinned tubes were then used to generate two distinct true stress-strain hardening material models based on the MPC stress-strain models. This was to ensure that the effect of strain hardening in the tubes as they deform was properly captured in the failure assessment. Using these generated material properties and models, the failure assessment of real tubes with localized external erosion is conducted, as discussed in the next chapter.

6 FAILURE ASSESSMENT OF REAL TUBES WITH LOCALIZED EROSION DEFECTS

6.1 Introduction

This chapter reports on the failure assessment conducted on a set of real failed tubes. The flaw geometric properties of these tubes are used to effectively replicate them on the already developed conceptualized models. Nonlinear finite element analysis (NLFEA) and parameterized studies are performed on these models using the material properties and models generated in the previous chapter. Results from the comprehensive investigations and parametric studies on the modelled localized thinned tubes are presented, from which new failure assessment criteria are deduced for these tubes. Finally, this developed methodology is compared with the API-ASME fitness-for-service assessment and the outcome is reported.

6.2 Numerical Analysis and Validation using Real Failed Tubes

6.2.1 Flaw geometric properties of the real failed tubes

The flaw geometric properties of the real failed tubes obtained using the technique already described in Section 3.4 are shown in Table 6.1. Tubes with f_w/D_o dimension ratio of less than 0.5 are u-shaped flaws while others above 0.5 are n-shaped flaws. No flat-line flawed tube is present among the tubes. These are then used for the modeling of the tubes in ANSYS® as described in Section 3.2.

Table 6.1: Flaw geometric properties obtained from real localized thinned tubes at their respective operating temperatures and pressures using the optimization technique

Tube No	Tube Grades	D_o (mm)	t (mm)	t_r (mm)	f_l (mm)	f_w (mm)	T_{ot} (°C)	P (MPa)	H (mm)	R (mm)	a (mm)	b (mm)
*1.	BS 3059 Grade 360	75.0	7.0	0.50	600	20	384	12.40	6957.333	6926.333	30.013	89.990
+*2.	BS 3059 Grade 360	50.8	4.4	0.30	80	25	358	12.40	218.477	197.177	105.101	114.305
+3.	BS 3059 Grade 360	50.8	4.4	0.17	70	40	358	12.00	168.088	146.911	25.191	14.062
4.	SA 210 A1	47.5	5.4	1.20	400	45	400	19.58	4783.560	4764.010	24.339	19.308
5.	SA 210 A1	50.8	6.3	0.38	150	50	390	17.50	497.282	477.805	25.692	19.475
*6.	BS 3059 Grade 440	63.5	6.6	0.80	240	30	417	20.35	1270.222	1244.277	65.505	76.520
+7.	BS 3059 Grade 440	38.0	3.8	0.30	155	32	367	20.21	875.290	859.790	18.336	10.269
+8.	BS 3059 Grade 440	38.0	3.8	0.30	110	28	367	20.21	449.399	433.899	20.283	9.604
9.	BS 3059 Grade 440	63.5	6.1	0.63	600	50	333	12.10	8255.710	8229.430	32.090	17.982
10.	BS 3059 Grade 440	63.0	5.4	0.42	310	60	350	11.20	2441.160	2414.640	32.179	26.529
11.	BS 3059 Grade 440	38.0	3.8	0.45	500	35	250	20.00	9345.680	9330.030	19.193	14.000
*12.	DIN 17175 15Mo3	33.0	3.6	0.20	20	15	414	20.91	29.506	16.406	10.789	14.325
13.	DIN 17175 15Mo3	44.5	5.6	0.41	225	35	370	21.81	1238.950	1221.890	25.593	12.279
14.	DIN 17175 15Mo3	33.9	6.5	0.24	300	30	400	19.40	1810.950	1800.260	22.227	10.672
15.	DIN 17175 15Mo3	44.5	5.2	0.50	140	44	405	19.00	541.180	523.630	22.403	17.561
16.	BS 3059 Grade 620	34.9	4.2	0.20	300	30	431	12.10	2827.950	2814.500	18.623	11.129

*These are the u-shaped flawed tubes, while others are the n-shaped flawed tubes.

+ Have same operating temperatures but with different flaw geometries and so are labelled as (a) and (b).

6.2.2 Parameterization, meshing and boundary conditions

In order to investigate other localized thinned tubes beyond the ones already reported, additional models with remaining thicknesses greater than the t_r of the failed tubes are created through parameterization. For each of the tubes, 9 additional models with the same tube and flaw dimensions but different remaining thicknesses are created from the initial t_r to t_{min}, which is the minimum remaining thickness of the tube based on allowable stress. This is computed using [100]:

$$t_{min} = \frac{P.D_O}{2.\sigma_a + P} \tag{6.1}$$

where P is the operating pressure and σ_a is the allowable stress at operating temperature.

Table 6.2 shows the allowable stress σ_a as obtained from their respective standards [100,102] and the minimum allowable thickness t_{min} as computed from Eq.(6.1).

Table 6.2: Minimum remaining thickness based on allowable stress for each tube

Tube Grades	T_{ot} (°C)	σ_a (MPa) at T_{ot}	P (MPa)	t_{min} (mm)
BS 3059 Grade 360	384	80.88	12.40	5.34
BS 3059 Grade 360	358	85.56	12.40	3.43
BS 3059 Grade 360	358	85.56	12.00	3.33
SA 210 A1	400	89.03	19.58	4.71
SA 210 A1	390	95.37	17.50	4.27
BS 3059 Grade 440	417	100.30	20.35	5.85
BS 3059 Grade 440	367	104.30	20.21	3.36
BS 3059 Grade 440	367	104.30	20.21	3.36
BS 3059 Grade 440	333	110.42	12.10	3.30
BS 3059 Grade 440	350	106.00	11.20	3.16
BS 3059 Grade 440	250	134.00	20.00	2.64
*DIN 17175 15Mo3	414	116.44	20.91	2.72
DIN 17175 15Mo3	370	118.80	21.81	3.74
DIN 17175 15Mo3	400	117.00	19.40	2.60
**DIN 17175 15Mo3	405	116.80	19.00	2.80
BS 3059 Grade 620	431	117.52	12.10	1.71

*The σ_a for the 15 Mo3 tubes are obtained using the details of the equivalent steel grade in BS 3059, as the DIN 17175 standard does not provide for it.

** Due to flaw size that is too large to be modelled using the computed t_{min}, a reduced t_{min} that could accommodate the flaw size is used.

The flaw geometric properties of the 9 additional models for each tube type are also obtained using the optimization technique as earlier explained in Section 3.4. Appendix G shows the tube remaining thicknesses and flaw geometries of all the 160 models in total used for this study.

The global meshing of the finite element models is performed using quadratic elements, 2 mm in size. In order to have finer quadratic hexahedral meshes in the flaw area, local mesh control measures are applied on the model. To ensure that the flaw area is dominated by quadratic hexahedral elements, the multizone mesh method is applied on the flaw area and the hex dominant mesh method is used on the body that is adjacent to the flaw area. To make the hexahedral elements finer around the flaw area, body size control is applied to reduce the element size to 1 mm, edge sizing used to create five divisions along the edge of the tube remaining thickness (t_r), and a sphere of influence vertex sizing of radius equal to a quarter of the f_w is applied on the peak of t_r, as shown in Figure 6.1. All these are to be done to ensure each model has good mesh quality and the results that will be obtained from the path created along the edge of the t_r will be reliable. As shown in Figure 6.2, the mesh convergence check done in terms of element quality and number of elements showed 3.6% difference on the plastic strain value between the highest and lowest number of elements.

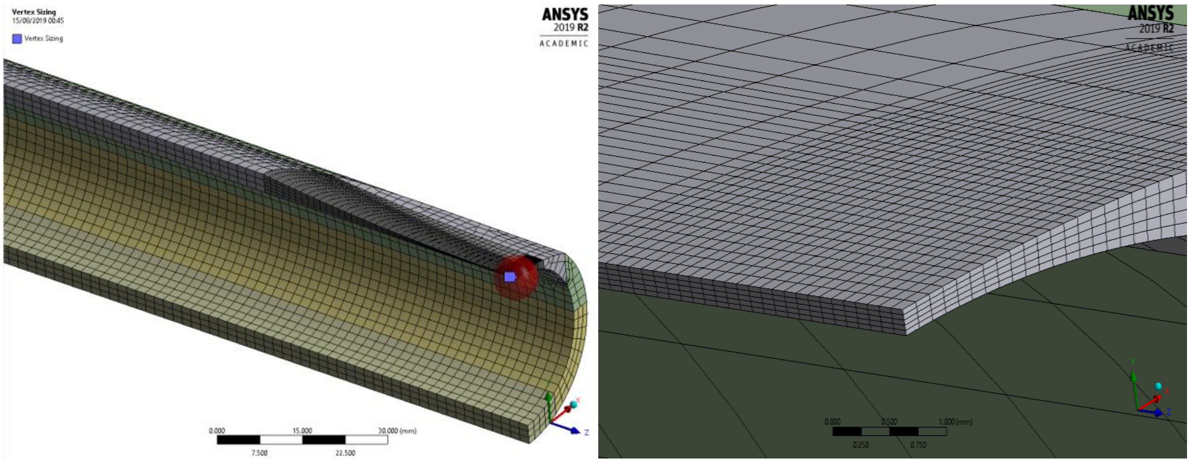

Figure 6.1: A meshed tube showing the refined flaw area and created vertex sphere of influence (on the left), with the enlarged mesh refinement as done along the edges of t_r (on the right).

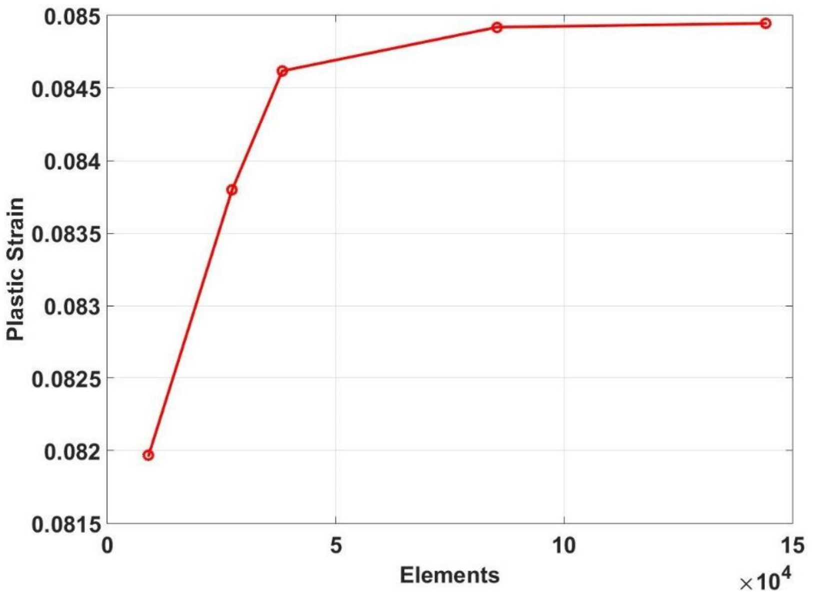

Figure 6.2: Mesh convergence plot

For the boundary conditions, frictionless supports are applied on the symmetrical boundaries of the models and to prevent rigid body motion, a displacement constraint is applied at the vertex on the lower tip of the model as shown in Figure 6.3. Each FEM is solved with its operating pressure (the pressure at which each tube failed in reality), which is applied by surface effect on the inner part of the model and ramped from zero to the given value. Also, an axial force based on the internal pressure is applied on the face of the model at the far-left side as shown in Figure 6.3. This helps to introduce the appropriate axial stress without modeling end cap effects. The model is solved using the direct solver type in ANSYS Mechanical using initial and minimum sub-steps of 20 and maximum sub-steps of 1000.

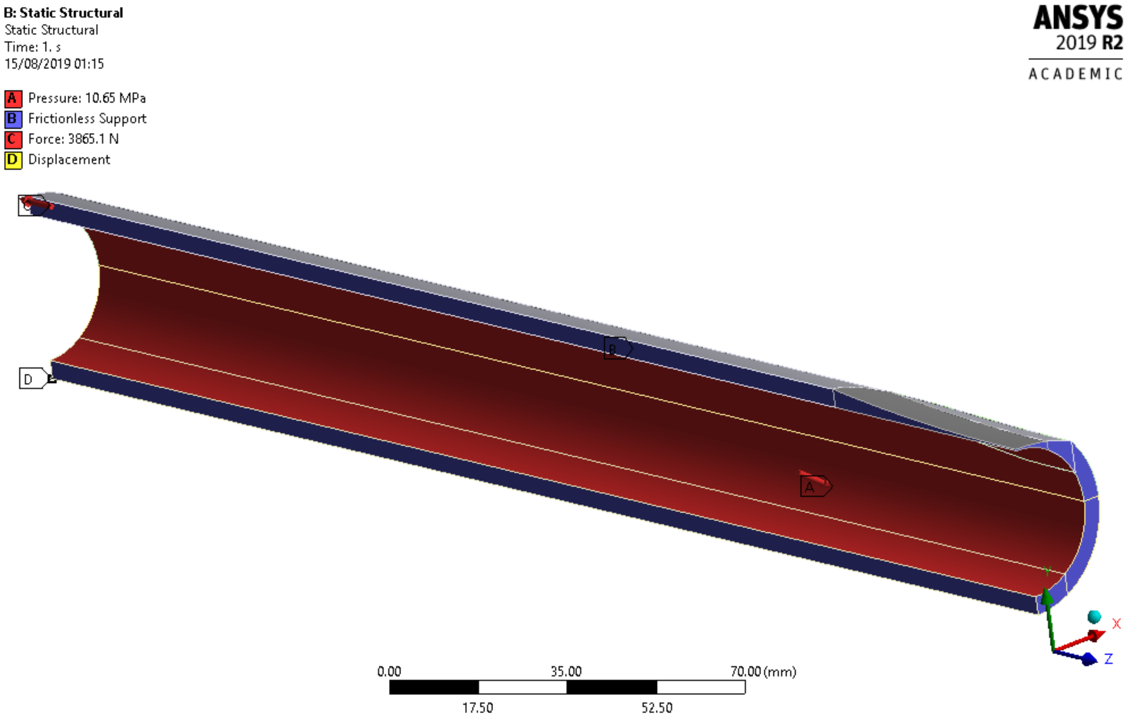

Figure 6.3: One of the localized thinned tubes showing all the boundary conditions applied.

6.3 Results and Discussion

6.3.1 Results using the second approach material model

Using the second approach material model (less conservative model), failure evaluation of 160 modelled tubes from 16 different tube grades are assessed based on the maximum equivalent plastic strain and Von Mises stress produced at the deepest point of the flaw area within each of the tubes when subjected to their respective operating pressures at which they fail, as shown in Figure 6.4.

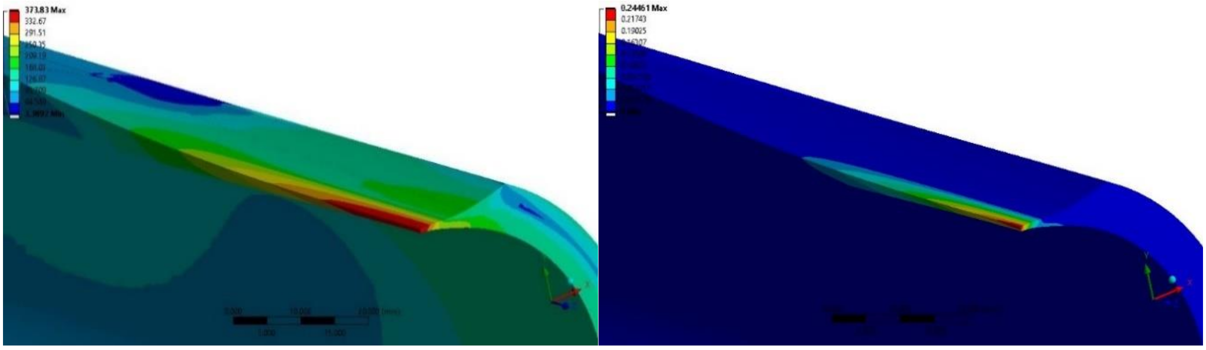

Figure 6.4: (a) Maximum equivalent von Mises stress and (b) plastic strain produced at the deepest point of one of the tubes flaw area.

Figure 6.5 depicts the results of the simulation, and it reveals that the plastic strain response for the normalized remaining thickness of the tubes (with respect to t_{min}) shows a nearly zero plastic strain for all the tube grades in the interval $t_r = 0.7\, t_{min}$ up to t_{min}. This indicates how safe these tubes could be within this range of remaining thickness while in service.

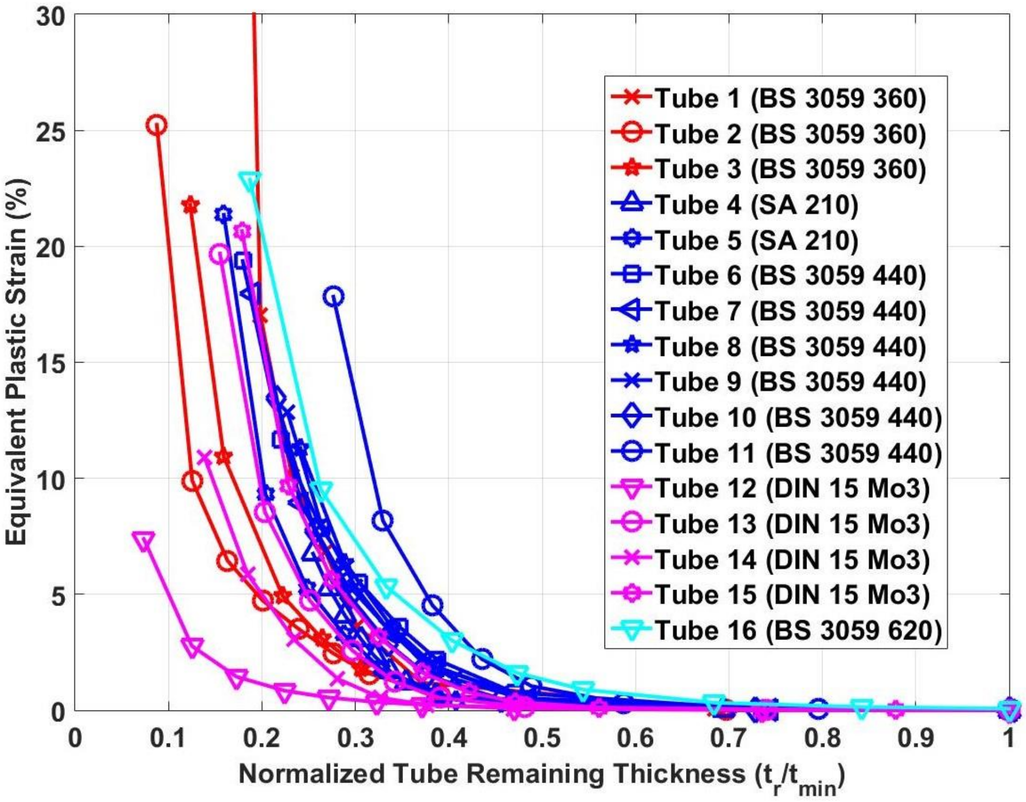

Figure 6.5: Plastic strain and normalized remaining thickness of the tubes based on the second material model

The result also indicates that the BS 3059 360 grades have relatively higher plastic failure strains as compared to other tubes grades. In fact, tube 1 continues to sustain more strain beyond 30% that is well above the material model true ultimate tensile strain $(\varepsilon_{t,uts})$ of ~22%. The other tube grades depending on their respective flaw geometries sustain broad range of plastic strains (between 6.75% and 22.88%) before failing. Failure in this context means that the analysis code fails to converge due to plastic strain localization and subsequent element inversion. All the tubes exceed a minimum of 5% plastic strain ($P_{5\%}$) before failure, with only two tube grades failing below 10% plastic strain ($P_{10\%}$). The implication of these results is that a reasonable plastic strain limit that would be safe for these heat resistant seamless tubes while in use can be deduced. Some earlier studies on localized thin areas had proposed a $P_{2\%}$ limit, which gave a conservative estimate of the real plastic collapse pressure for pressurized vessels [19,59]. It could also be recalled that earlier results reported in Section 4.5 from analyzing failure pressures of modeled conceptualized tubes based on various failure criteria indicated $P_{5\%}$ or $P_{7.5\%}$ as a safe limit criteria. Thus, a $P_{5\%}$ limit as seen from this outcome from real tubes is proposed as a more suitable failure criterion with reduced conservatism. Also, depending on one's appetite for risk, the criterion may be adjusted as deemed fit for different scenarios. For instance, if a user chooses to use the $P_{2\%}$, the allowable remaining tube thickness that could be considered safe will be 0.4 t_{min}, while at $P_{5\%}$, a reduced tube thickness as low as 0.3 t_{min} is seen to still be safe. By using the proposed strain limit and measuring the remaining thicknesses of the tubes while in service, the flawed tubes could be ranked based on the severity of their flaws, such that only the critical ones are repaired or replaced while others that could still be safe for continued operation are left for the next planned maintenance of the tubes.

From Figure 6.6 and Figure 6.7, based on the different shades of the plots, the effect of the flaw geometries on the tubes failure in terms of their f_l/f_w and f_w/f_d aspect ratios respectively can be seen, with Tube 1 having the largest f_l/f_w but the smallest f_w/f_d. The influence of this lengthy but narrow flaw is most likely one of the reasons Tube 1 is able to sustain continued plastic strains beyond its $\varepsilon_{t,uts}$, as earlier reported. In the same manner, other tube grades (like Tubes 6, 14 and 16) with fairly large f_l/f_w and small f_w/f_d ratios also sustain large plastic strains.

It can also be observed that tubes (like Tubes 3, 5, 7, 10, 15) with small f_l/f_w but fairly large f_w/f_d ratios equally sustain large plastic strain before failure. Interestingly, the two observations demonstrate the influence of lengthy but small width flaws and small but fairly large width flaws that potentially make these tubes sustain gross plastic strains before failing. The reason for this is that the flaw geometry creates room for the surrounding material to absorb some of the plastic strains and consequently helps to reduce the strain concentration produced within the flaw area of the tubes. Thus, making the tubes to sustain more plastic strains before they eventually fail.

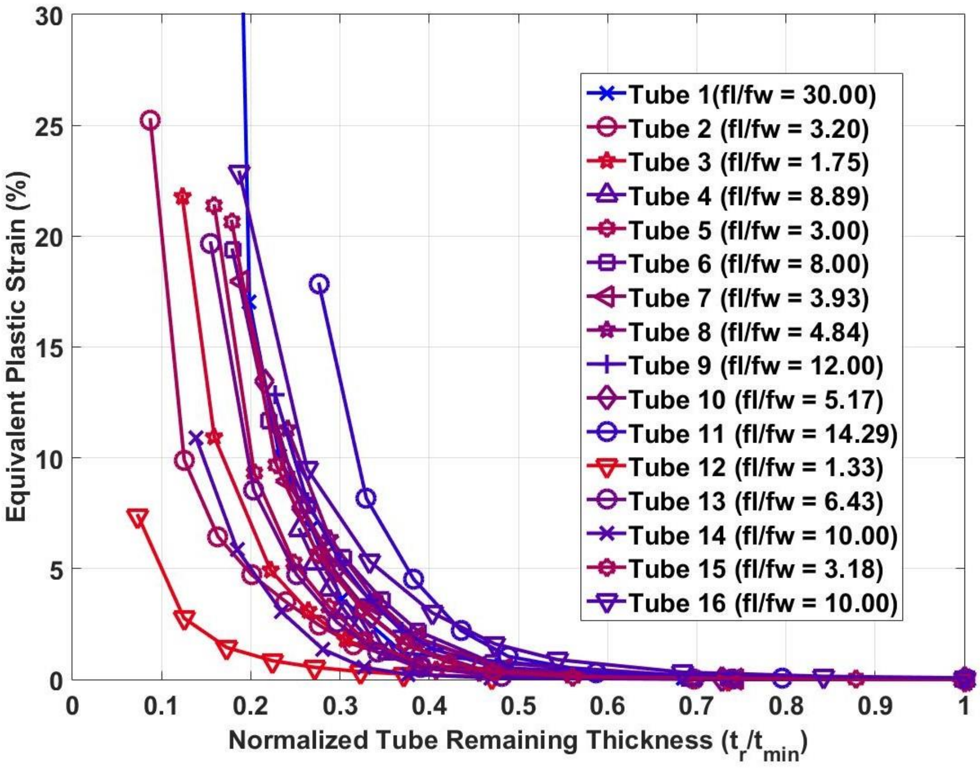

Figure 6.6: Plastic strain and normalized remaining thickness of the tubes with respect to their f_l/f_w aspect ratios based on the second material model coloured from red to blue – the lines are coloured from red to blue, where more red indicates a smaller value of f_l/f_w and more blue indicates a larger value.

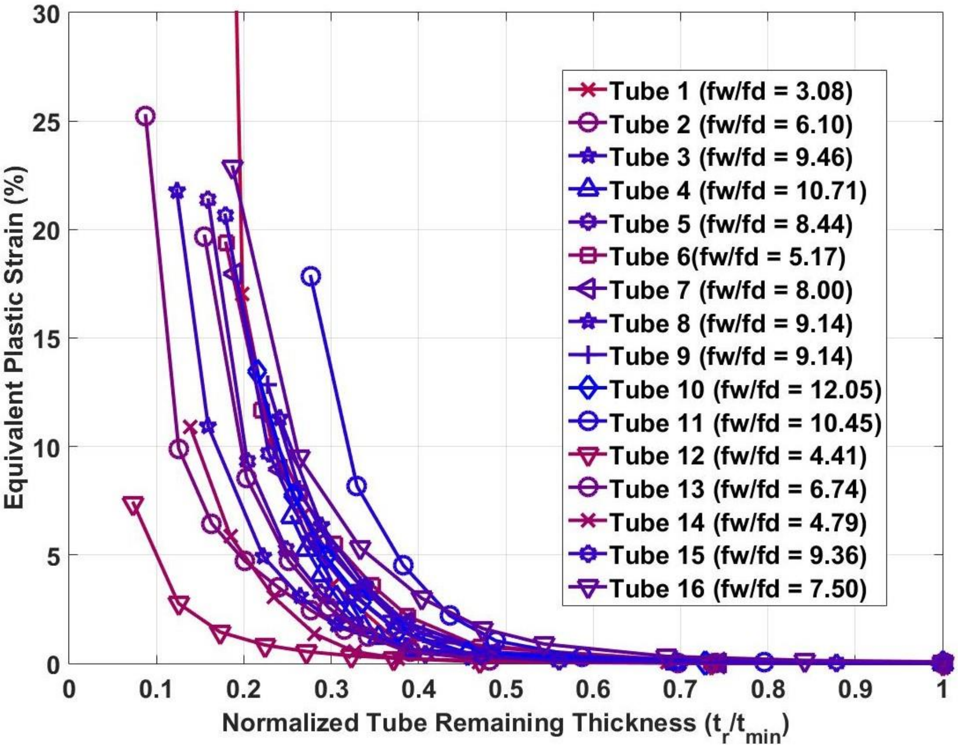

Figure 6.7: Plastic strain and normalized remaining thickness of the tubes with respect to their f_w/f_d aspect ratios based on the second material model coloured from red to blue - the lines are coloured from red to blue, where more red indicates a smaller value of f_w/f_d and more blue indicates a larger value.

It can be recalled from the Section 4.4.2 when the effect of f_d/f_w and f_w/f_d ratios on the failure pressure of the tubes were investigated for cases of conceptualized variants of boiler tubes under localized erosion flaws, the above findings were found to be true for large aspect ratios. Hence, this current analysis on real tubes expounds and substantiates the previously reported findings. It can now be seen that tubes with fairly large f_w/f_d ratios and small f_l/f_w will be able to sustain large plastic strains before failing, likewise tubes with a vice versa flaw geometry.

Also, the above results reveal that the tubes which failed under $P_{10\%}$ (Tube 12 with the smallest flaw having the smallest f_l/f_w and a small f_w/f_d and Tube 4 with a mid-range f_l/f_w and f_w/f_d ratios), show the possibility for some tubes to fail in reality at quite low plastic strains. Hence, these two real life examples present another motivation why a lower bound of $P_{5\%}$ could be a suitably safe strain limit criterion.

Figure 6.8 shows the peak Von Mises stress normalized with the σ_{uts}. It can be seen that the equivalent Von Mises stresses for all the tube grades at t_{min} are about 0.3 σ_{uts} and continue up until 0.9 σ_{uts} before any failure occurred. Most of the tubes remain intact beyond the σ_{uts}, with only Tube 4 and Tube 12 failing at 0.95 σ_{uts}.

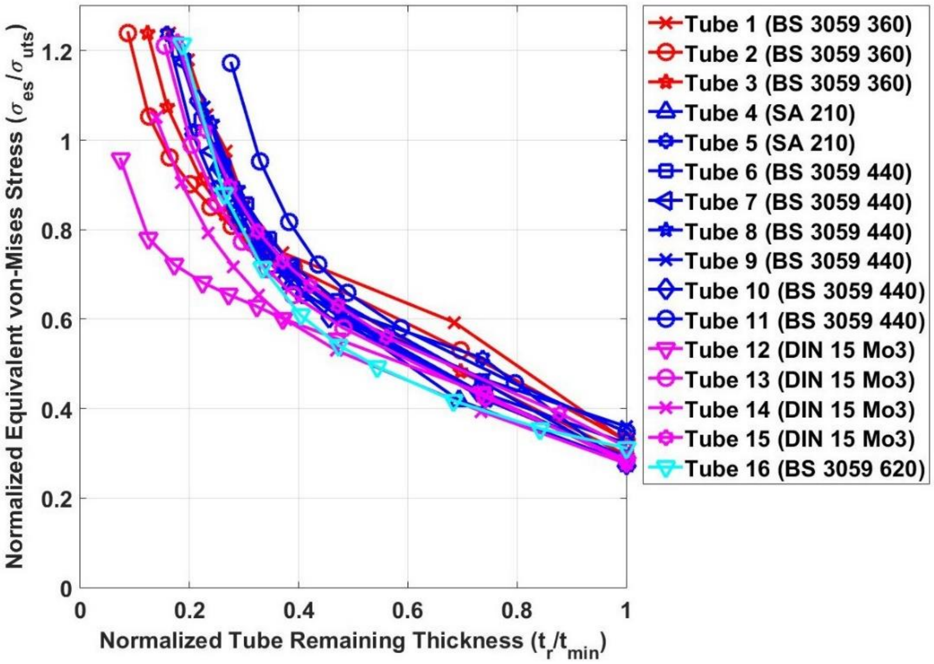

Figure 6.8: Von Mises stress with respect to σ_{uts} and normalized remaining thickness of the tubes based on the second material model

Figure 6.9 also reveals that the equivalent Von Mises stresses normalized with respect to the true ultimate tensile strength $(\sigma_{t,uts})$ shows all the tubes exceeding a minimum of 0.7 $\sigma_{t,uts}$.

Based on these findings, an equivalent Von Mises stress criterion can be deduced that could be safe for these heat resistant tubes while in service. Previous studies on external eroded pipes proposed the σ_{uts} as their criteria limit [68,72]. Thus, 0.8 σ_{uts} as a deduced failure criterion from the result obtained will be a reasonably safe limit for these tubes.

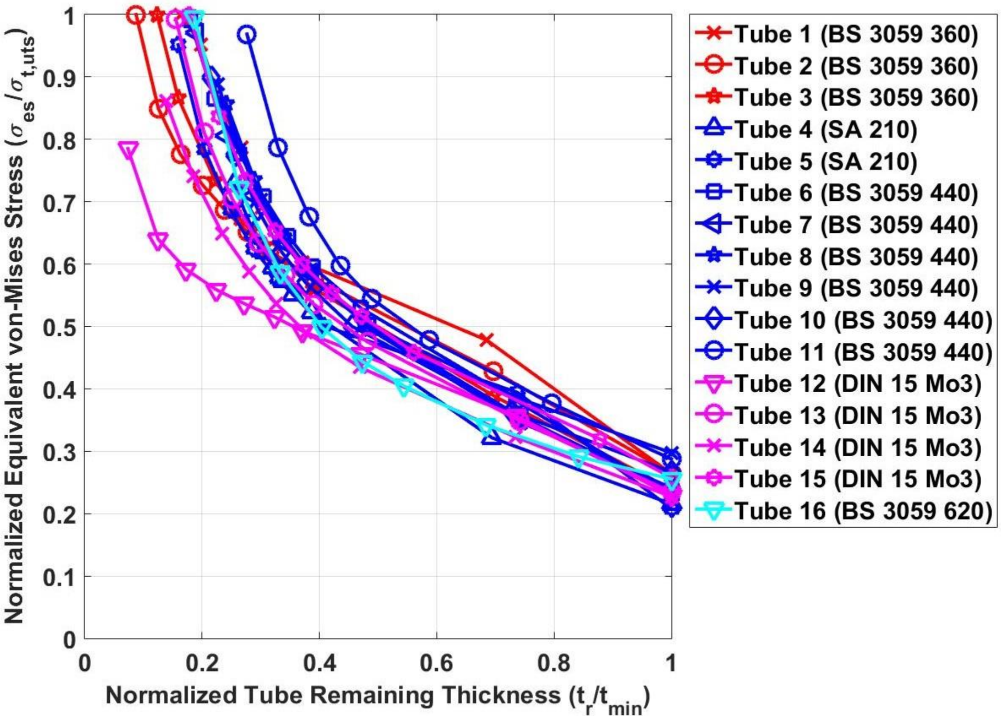

Figure 6.9: Von Mises stress with respect to $\sigma_{t,uts}$ and normalized remaining thickness of the tubes based on the second material model

6.3.2 Results using the third approach material model

The results of the assessment performed on the same modelled tubes but using the third approach material model (conservative model) are presented. The maximum equivalent Von Mises stress and plastic strain produced at the deepest point of the flaw area within each of the tube are obtained. Considering the result of the plastic strains for the normalized remaining thickness in Figure 6.10, it will be observed that for all the tube grades from when $t_r = 0.7\, t_{min}$ to t_{min}, there is almost zero plastic strain. It can be recalled that the same was also seen with the less conservative model in Section 6.3.1. This reinforces the earlier deduction in Section 6.3.1 that the tubes will be safe within the same range of remaining thickness while in operation.

The result also shows that except for two of the BS 3059 360 grades that have relatively higher plastic failure strains (beyond their material model $\varepsilon_{t,uts}$), the other tube grades depending on their respective flaw geometries sustain a broad range of plastic strains (between 6.76% and

22.35%) before failing. All the tubes exceeds a minimum of $P_{5\%}$ before failure, with only Tube 4 failing below $P_{10\%}$, which indicates the possibility for a tube to fail at low plastic strain. These results substantiate the earlier result in Section 6.3.1 that a plastic strain criterion that could be safe for these tubes while in service can be deduced for either specific grades of tubes or across all commonly used heat resistant seamless tubes in the power generation industry. Thus, it is proposed that the lower bound $P_{5\%}$ be used as a failure criterion, which can help prevent replacing tubes that can still be safe for continued operation.

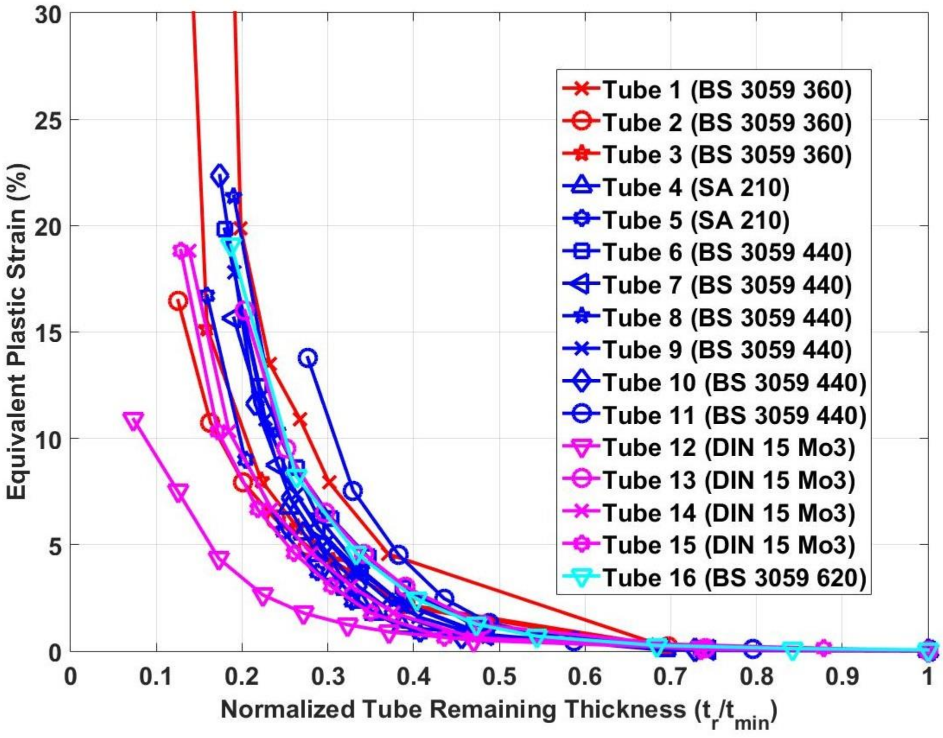

Figure 6.10: Plastic strain and normalized remaining thickness of the tubes based on the third material model

The influence of flaw geometries on the failure of the tubes in terms of their f_l/f_w and f_w/f_d aspect ratios respectively can be seen in Figure 6.11 and Figure 6.12**.** Here, it can be noticed that because of the conservativeness of the third model, in addition to Tube 1 with the largest f_l/f_w but smallest f_w/f_d (as seen in the case of the less conservative model), Tube 3 which has one of the smallest f_l/f_w but fairly large f_w/f_d continued to sustain large plastic strains beyond their $\varepsilon_{t,uts}$. Other tubes with fairly large f_l/f_w and small f_w/f_d ratios (like Tubes 6 and 16), as well as those with small f_l/f_w but fairly large f_w/f_d (like Tubes 5, 8, 10, 15) ratios sustain relatively large plastic strain before failure, similar to what was observed in Section 6.3.1. This again demonstrates the effect of a lengthy but small width flaw and a small but fairly large width flaw that cause these tubes to sustain large plastic strains as explained in Section 6.3.1.

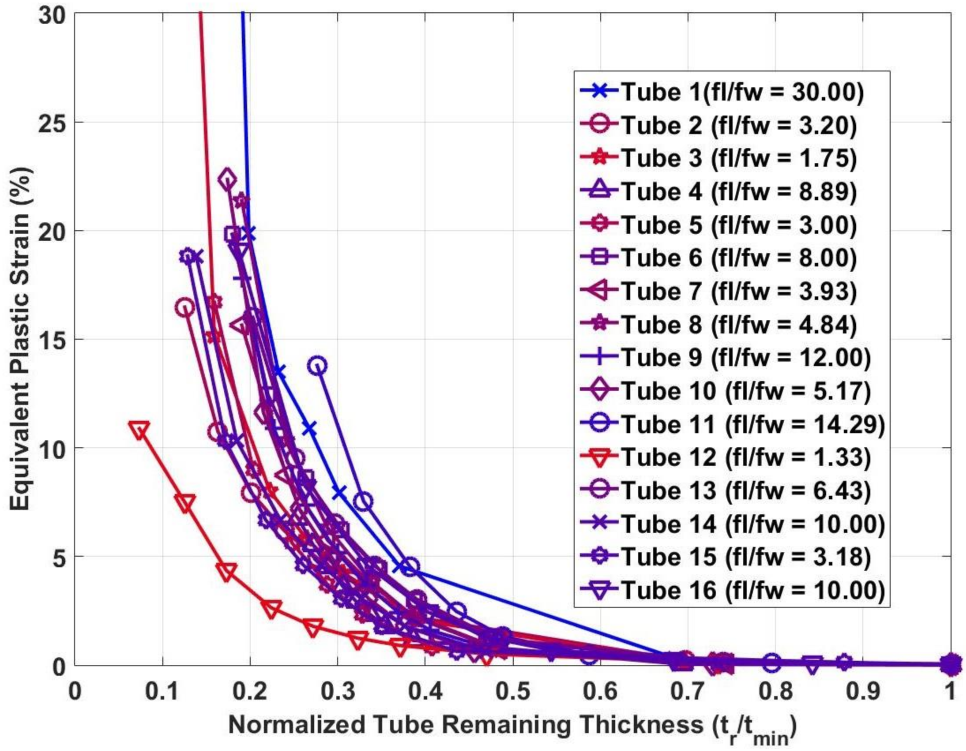

Figure 6.11: Plastic strain and normalized remaining thickness of the tubes with respect to their f_l/f_w aspect ratios based on the third model coloured from red to blue - the lines are coloured from red to blue, where more red indicates a smaller value of f_l/f_w and more blue indicates a larger value.

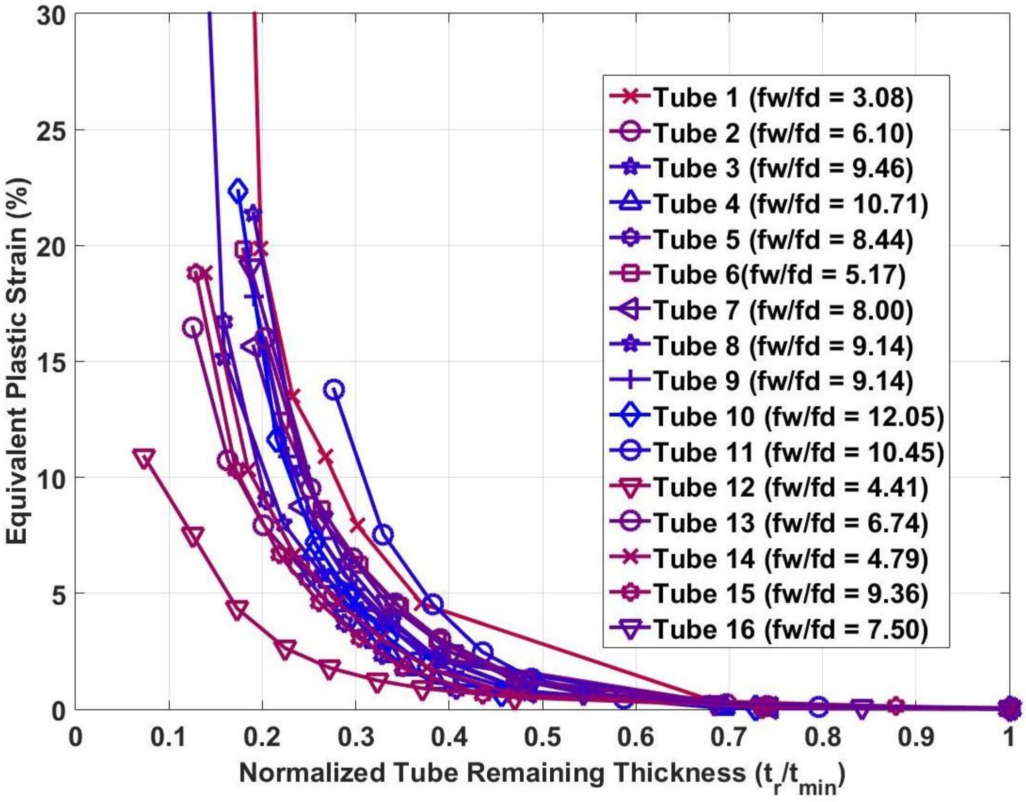

Figure 6.12: Plastic strain and normalized remaining thickness of the tubes with respect to their f_w/f_d aspect ratios based on the third material model coloured from red to blue - the lines are coloured from red to blue, where more red indicates a smaller value of f_w/f_d and more blue indicates a larger value.

Based on the result of the equivalent Von Mises stresses as seen in Figure 6.13, it could be observed that for all the tube grades, the stresses around the flaw area ranged from about 0.3 σ_{uts} to 0.9 σ_{uts} before one or two tubes failed. Most of the tubes continue to survive beyond the σ_{uts}, with only Tube 4 and Tube 12 grades failing at 0.84 σ_{uts} and 0.96 σ_{uts} respectively. For the equivalent Von Mises stresses with respect to the true ultimate tensile strength $(\sigma_{t,uts})$ as seen in Figure 6.14, a similar observation shows all the tubes grades exceeding a minimum of 0.7 $\sigma_{t,uts}$. From all these findings, it is obvious that the result from this third material model closely correlates with that of the second material model, only with Tube 4 failing quicker because of the conservativeness of the model. In spite of this, the same earlier proposed equivalent Von Mises stress criterion of 0.8 σ_{uts} is still adequate for the conservative model. This will ensure that the tubes remain safe while in service and also avoid their early replacement.

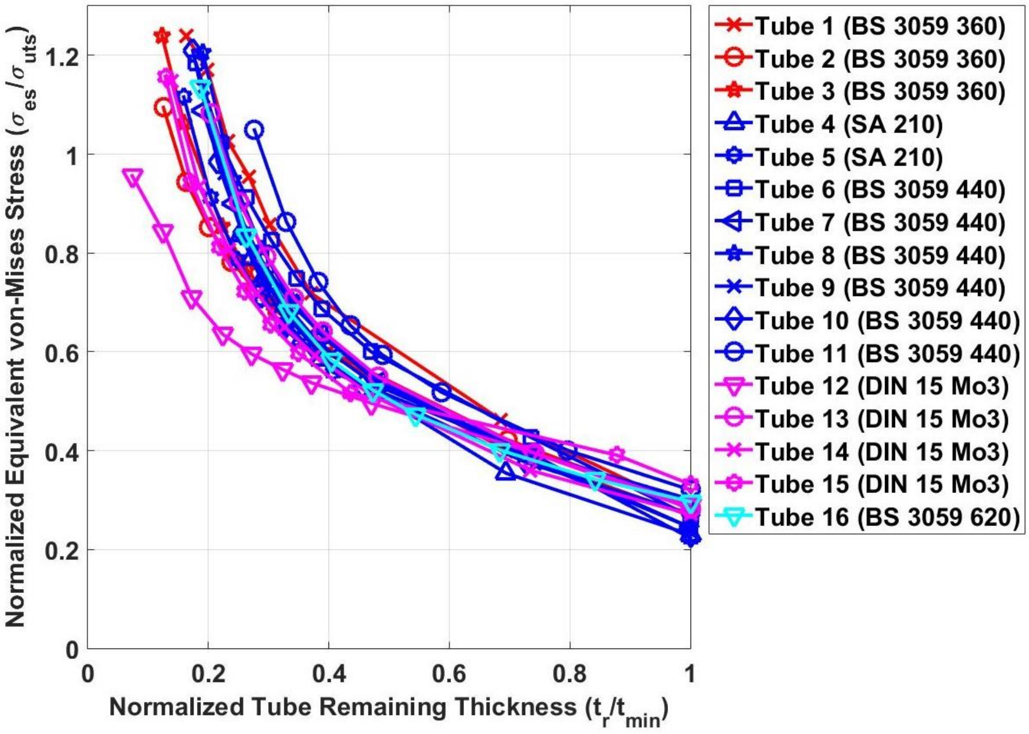

Figure 6.13: Von Mises stress with respect to σ_{uts} and normalized remaining thickness of the tubes based on the third material model

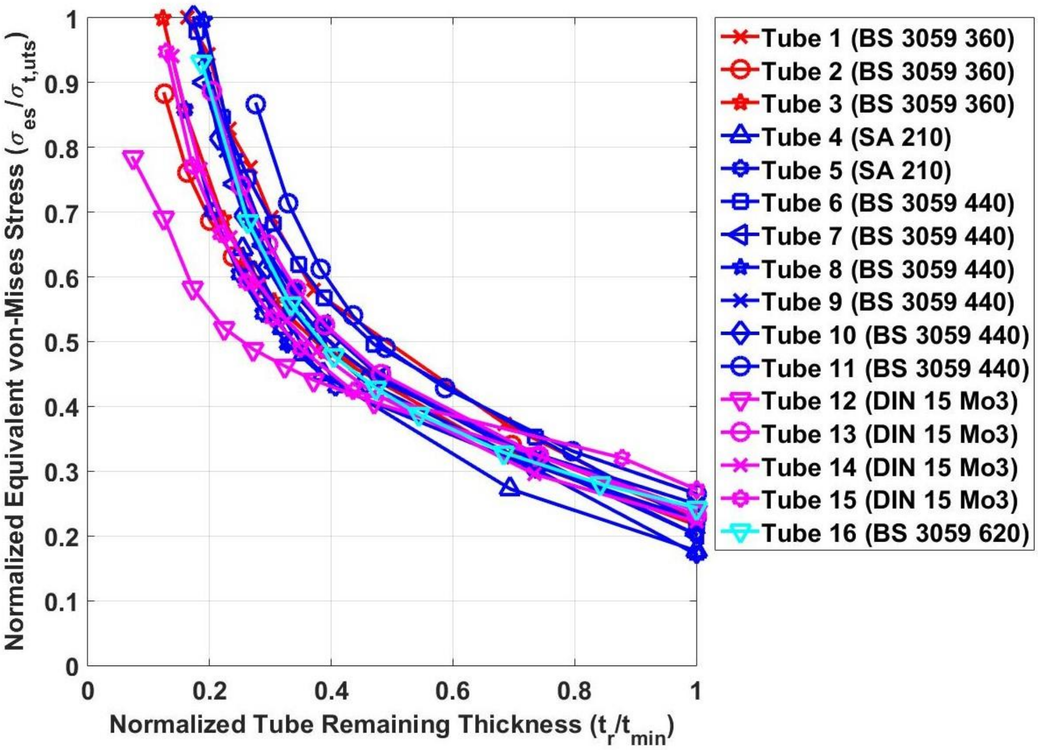

Figure 6.14: Von Mises stress with respect to $\sigma_{t,uts}$ and normalized remaining thickness of the tubes based on the third material model

6.4 Fitness-for-Service Assessment using the API-ASME FFS Standard

Having considered in detail the assessment of these real tubes, which have also been implicitly validated since they were determined from the respective pressures at which the tubes failed, it is still necessary to corroborate the proposed methodology and criteria by comparing them with the fitness-for-service assessment (FFS) on the tubes using the API-ASME standard [33,34].

6.4.1 FFS methodology

FFS analysis are performed on the 160 models used in this study. The nonlinear (elastic-plastic) stress analysis of the API-ASME FFS standard considered as the most accurate method is employed. In the standard, the concept of Load and Resistance Factor Design (LRFD) is to be used to determine the global plastic collapse load of the pressurized vessel to ensure its protection against plastic collapse. For the LRFD, different factored load combinations, based on the loads the vessel is subjected to, are to be used for the numerical analysis. For the case of internal pressure as applicable to the study presented in this study, the required factored load combination is given as:

$$\text{Factored Load for Elastic Plastic Stress Analysis} = \beta . P \tag{6.2}$$

β is the load factor coefficient based on the factor applied to the σ_{uts} to obtain a design allowable stress, (the value varies for different construction codes) as seen in Table 6.3. $\mathrm{RSF_a}$ is the allowable remaining strength factor which by the standard has a recommended value of 0.9.

The FFS is to be performed using the factored load for the finite element analysis (FEA) and if convergence is attained, it indicates that the boiler tube being analysed is stable globally under the applied load. If the FE simulation does not converge, the tube thickness would be modified (increased) or the applied loads reduced, and the analysis is repeated until convergence is attained. The highest pressure at which the simulation converges is defined as the plastic collapse pressure, P_{pc}. Note that if the simulation converges using the factored load, then the actual plastic collapse pressure is not obtained, as it is known that plastic collapse would occur at a greater pressure than is required by the standard.

It is clear from this discussion that determining the plastic collapse load requires many simulations which do not converge, and consume a lot of computational resources, making this a tedious procedure.

Table 6.3: Factored loads used for this study based on construction codes of the boiler tubes and applied loads

Construction Code	β	Factored Load for Global Stability
PD 5500	$2.35\mathrm{RSF_a}$	$2.12P$
EN 13345	$2.40\mathrm{RSF_a}$	$2.16P$
ASME Section VIII, Division 2, prior to the 2007 Edition	$3.00\mathrm{RSF_a}$	$2.70P$

Notes: The PD5500 represents the British specification for unfired, fusion welded pressure vessels, which the BS 3059 tubes fall under. While the EN 13345 represents the EU Standard for unfired pressure vessels that can also be applicable for both the BS 3059 tubes and the DIN 17175 tubes. The SA 210 A1 tubes fall under the ASME Section VIII codes.

In addition to demonstrating the global stability of the tubes (i.e., protection against plastic collapse) using the factored loads, the standard requires that the protection against local failure should be satisfied. This is to be done in terms of a strain limit, if the flaw creates a significant strain concentration within the tube. To ensure local stability for all the tube grades, an elastic plastic stress analysis based on the plastic collapse load is to be performed to determine a limiting triaxial strain, ε_{lt}. This will be compared with the sum of the total equivalent plastic strain, ε_{ps} within the flaw area and the forming strain, ε_{cf} if present in the tubes. But since the tubes all considered in this study are heat treated, the forming strain is taken as zero according to the standard. Hence, the ε_{lt} is only compared with the ε_{ps}.

The strain limit criteria to be satisfied is as follows:

$$\varepsilon_{ps} + \varepsilon_{cf} < \varepsilon_{lt} \tag{6.3}$$

Note for heat treatment tubes, $\varepsilon_{cf} = 0$. The limiting triaxial strain ε_{lt} is obtained from

$$\varepsilon_{lt} = \varepsilon_u * exp\left[-\left(\frac{\alpha_{mf}}{1+m_2}\right)\left(\left\{\frac{\sigma_1+\sigma_2+\sigma_3}{3\sigma_e}\right\}-\frac{1}{3}\right)\right], \tag{6.4}$$

where ε_u is the uniaxial strain limit, α_{mf} is the material factor for the multiaxial strain limit, m_2 is the strain hardening exponent, σ_1, σ_2, σ_3 are the principal stresses, and $\sigma_e$is the equivalent Von Mises stress within the flaw area.

The computation for ε_u and m_2, as well as the value of α_{mf} can be obtained from the standard. Since the heat resistant seamless tubes studied in this research are ferritic steels, only the details of these materials are provided in Table 6.4. It should be noted that if the elongation or reduction in area of a tube is specified, then ε_u would be taken as the maximum value of any of m_2, elongation, and reduction of area. R_o is the ratio of the minimum specified yield strength to the minimum specified tensile strength of the tubes (i.e., $R_o = \sigma_y/\sigma_{uts}$), E_o is the elongation in percentage and RA is the reduction in area in percentage based on the material specification of the tube.

Table 6.4: α_{mf} value and details for computing ε_u and m_2 from API-ASME FFS [33]

Material	Maximum Temperature	ε_u			α_{mf}
		m_2	Elongation Specified	Reduction of Area Specified	
Ferritic steel	480°C	$0.60(1.00 - R_o)$	$2 * \ln\left[1 + \frac{E_o}{100}\right]$	$\ln\left[\frac{100}{100 - RA}\right]$	2.2

6.4.2 Comparing the proposed methodology and criteria with FFS

Failure assessment of the localized tubes based on the proposed methodology reported earlier had been carried out using the operating pressure at which the tubes failed. From the assessment outcome, a strain and stress limit criteria were deduced, which could be applied to the tubes to ensure they remain safe for continued operation while avoiding their early replacement.

The proposed failure criteria of 5% plastic strain, $P_{5\%}$ or the equivalent Von Mises stress criterion of 0.8 σ_{uts} will now be compared to the outcome of the FFS assessment carried out on the tubes. As explained in Section 6.4.1, FFS requires changing the tube geometry or applied load in order for the tube to be globally stable under the required factored load. For the purpose of this comparison, the tubes are not re-rated, but the plastic collapse pressure P_{pc} for each tube is recorded. The load factor is defined as the ratio of the plastic collapse pressure, P_{pc} to the operating pressure, P. As the highest load factor required by the standards is 2.7, no plastic collapse pressures above $2.7P$ were obtained.

Figure 6.15 shows the load factor plotted against the normalized remaining thickness for all tubes. Also shown as dotted lines on Figure 6.15 are the recommended load factors for each standard. As can be seen, the load factor was at least equal to the threshold load factor of 2.7 for most of the tubes from approximately $t_r = 0.7\, t_{min}$ up to t_{min}, with Tube grades 12 and 14 extending beyond $0.7\, t_{min}$. The implication of this is that most of these tubes will remain intact and not fail from when $t_r = 0.7\, t_{min}$ to t_{min}. This indicates how safe these tubes could be within this range of remaining thickness while in service. It can be recalled that a similar trend was observed when using the proposed failure criteria, as earlier explained in Section 6.3.1 and Section 6.3.2. In this regard, this shows good correlation between the two methodologies.

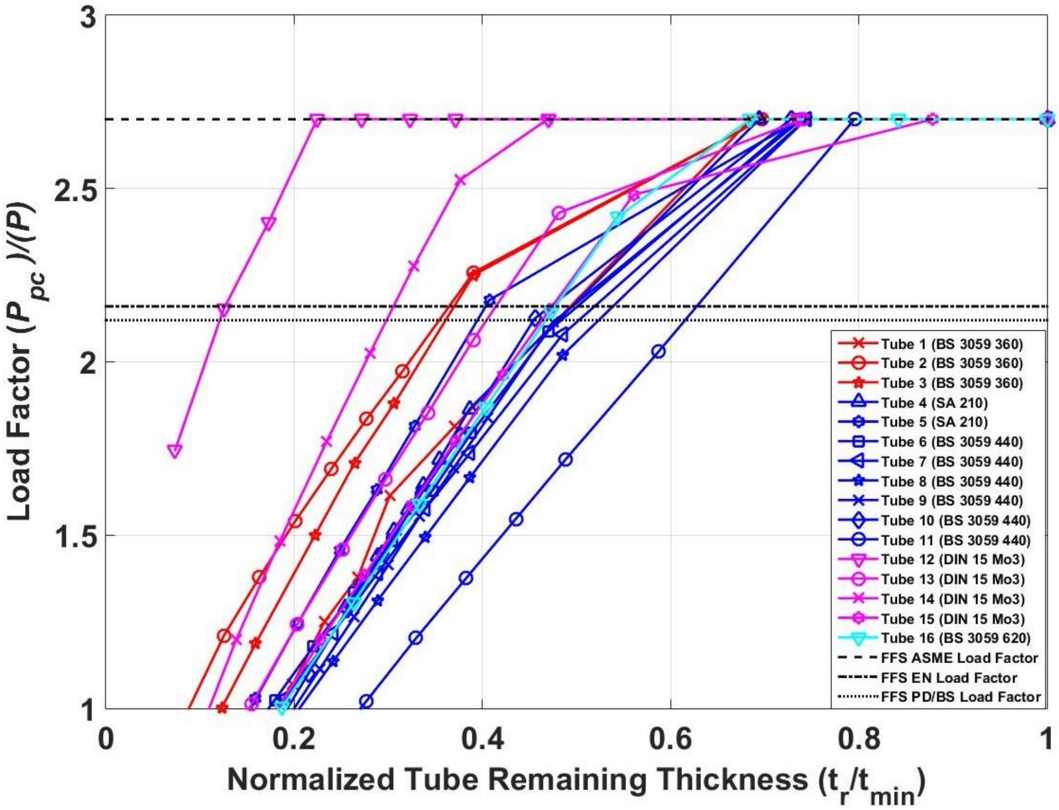

Figure 6.15: Load factors on the normalized tube remaining thickness of the modelled tubes. Note: If the simulation was stable at the threshold load factor of 2.7, the true plastic collapse load factor was not computed.

The result also shows that the failure of most of the tubes were predicted well, with failure occurring at a load factor of 1, the actual operating pressure. The exceptions were two tubes (Tube 12 and Tube 4) that were predicted relatively earlier, at load factors of 1.75 and 1.29 respectively. It is interesting to note that from the outcome of the failure assessment based on the proposed methodology, these tubes also had low plastic strains (~ 7%), which were above the $P_{5\%}$ limit and failed at about 0.95 σ_{uts}, above the 0.8 σ_{uts} stress limit. This corroborates why the proposed plastic strain and stress limit were recommended, leaving allowance for some uncertainty. A user may still choose a less conservative failure criterion as deemed fit for different grades of tubes and different scenarios, like in a constrained economic environment with ageing infrastructures.

However, the FFS failure prediction of all the tubes based on the three recommended load factors (FFS ASME load factor, FFS EN load factor and FFS PD/BS load factor) occur much earlier than the operating pressure at which they failed in reality, which is at a load factor of 1. For instance, based on the FFS PD/BS load factor, which is at 2.12, all the tubes would have been predicted to be globally unstable and susceptible to plastic collapse below the limit. But from the result, the tubes continue to survive below that limit up until a load factor of 1. This shows how conservative the FFS methodology is in predicting the failure of the tubes.

From Sections 2.2.5 and 6.4.1, the use of the FFS actually requires a detailed inspection of the tube and much information for the assessment. Beyond the ε_{ps} and σ_e, the assessment also requires the following input: β and $\varepsilon_u, m_2, \alpha_{mf}, \sigma_1, \sigma_2, \sigma_3$ to compute ε_{lt} for level 3 assessment. The other two lower levels (level 1 and 2) that must be done before level 3 assessment require lot more of input information. Cumbersome FEA simulation is also required each and every time you need to do an assessment for a particular flaw, which must be performed by an experienced engineering specialist. All these could be very demanding from time and cost perspectives.

Based on the challenges of using the FFS, it can be seen that in comparison to the proposed methodology in this thesis, which involves using the minimum remaining thickness for a specific tube grade and failure criteria values, given the operating pressure and temperature, a lot of computation time and resources can be saved and still be able to predict the failure of the tubes before they occur in reality.

6.5 How the Proposed Methodology will be used in Practice

The main requirements to conduct failure assessment on tubes under localized external erosion using the proposed methodology are the boiler tube grades, the tube and flaw dimensions, and the operating conditions (temperature and pressure) of the tubes to be assessed. Following the procedures that have been documented in Chapter 5 and 6, a user can generate the normalized remaining thickness curves for the plastic strains or normalized equivalent Von-Mises using a set of localized external erosion flaws with the stated requirements. On that basis, they can then categorize every other detected flaws from the most severe to the least severe, simply by measuring the remaining tube thickness, t_r, of the tubes based on the proposed failure criteria of 5% plastic strain, $P_{5\%}$ or the equivalent Von Mises stress criterion of 0.8 σ_{uts}. They may also choose to adjust the criteria as deem fit to them. By so doing, they will be able to prioritise the repair or replacement of more critical flawed tubes, judiciously use their maintenance budget, and ultimately avoid unplanned outages that usually lead to loss of production and costly emergency repairs.

6.6 Summary and Conclusions

A failure assessment methodology framework for heat resistant seamless steel boiler tubes with localized external erosions was presented in this chapter. Flaw geometric properties of these real failed tubes were obtained and used to accurately replicate the tubes on the already developed conceptualized geometries. For a detailed failure assessment of the tubes, using the optimization technique in MATLAB® and through parameterization in ANSYS®, 160 finite element models with the same tube and flaw dimensions but different remaining thicknesses (t_r) were generated from the 16 tube grades from their initial t_r to their t_{min}.

Using the MPC material models generated from material data, NLFEA investigations were conducted on the 160 flawed tubes. These tubes were assessed based on the maximum equivalent plastic strain and Von Mises stress produced at the deepest point of the flaw area within each of the tubes when subjected to their respective operating pressures at which they failed. The following outcomes were established from the failure assessment:

1. The results show a near zero plastic strain response for the normalized remaining thickness of the tubes (with respect to t_{min}) for all the tube grades from when $t_r = 0.7$ t_{min} up to t_{min}. The implication of this is that most of these tubes will remain intact and not fail from when $t_r = 0.7\ t_{min}$ to t_{min}, which indicates how safe these tubes could be within this range of remaining thickness while in service.
2. Most of the tube grades sustained a broad range of plastic strains (between 6.75% and 22.88%) before failing, with some even extending beyond 23%. The implication of these findings is that a reasonable plastic strain limit that could be safe for these heat resistant seamless tubes while in use can be established. Some earlier studies on localized thin areas had proposed a $P_{2\%}$ limit, which gave a very conservative estimate

of the real plastic collapse pressure for pressurized vessels [19,59]. Thus, a $P_{5\%}$ limit as seen from this result is an improved failure criterion with reduced conservatism.

3. Tubes with fairly large f_l/f_w and small f_w/f_d aspect ratios and also small f_l/f_w but fairly large f_w/f_d ratios all sustained large plastic strain before failure. This outcome demonstrates the influence of lengthy but small width flaws and small but fairly large width flaws that make these tubes sustain gross plastic strains before failing. The reason for this is that the flaw geometry creates room for the surrounding material to absorb some of the plastic strains and consequently helps to reduce the strain concentration produced within the flaw area of the tubes. This allows the tubes to sustain more plastic strains before they eventually fail. The possibility for some tubes to fail in reality at quite low strains was noticed from two tubes that failed below $P_{10\%}$. Therefore, a lower bound $P_{5\%}$ limit was recommended as the failure criteria to be used.
4. The equivalent Von Mises stresses for all the tube grades at t_{min}, were about 0.3 σ_{uts} and continued up until 0.9 σ_{uts} before any failure occurred. Most of the tube grades remained intact beyond the σ_{uts}, with only two tube grades failing at 0.95 σ_{uts}. From this result, an equivalent Von Mises stress criterion that could be safe for these heat resistant tubes while in service was deduced as 0.8 σ_{uts}. Previous studies on external eroded pipes had used the σ_{uts} as their criteria limit [68,72], hence, the deduced failure criterion was considered as a reasonably safe limit for the tubes.

The strain and stress limit criteria deduced from the assessment framework can be employed to heat resistant seamless tubes to ensure they remain safe for continued operation while avoiding their early replacement. Even though the assessment results of the real tubes have been implicitly validated since they were determined from the respective operating pressures at which the tubes failed, it was still necessary to corroborate the proposed methodology and criteria by checking and comparing them with the fitness-for-service assessment (FFS) using the API-ASME standard. The outcomes of the comparison were as follows:

1. The results of the FFS show good correlation between the two methodologies. Similar to the observations from the proposed methodology, the load factor was at least equal to the maximum recommended load factor of 2.7 for most of the tubes from approximately $t_r = 0.7\, t_{min}$ up to t_{min}. This again indicates that most of these tubes will remain intact and not fail from $t_r = 0.7\, t_{min}$ to t_{min}, establishing how safe these tubes will be within this range of remaining thickness while in service.

2. The result also shows that the failure of most of the tubes were predicted well except for two tubes that were predicted relatively earlier when compared to their actual failure pressures. This was similarly observed from the proposed methodology, where the same tubes also had low plastic strains (~ 7%), which were above the $P_{5\%}$ limit and failed at about 0.95 σ_{uts}, which was also above the 0.8 σ_{uts} limit. This corroborates the choice of the plastic strain and stress limits, which allow room for some uncertainty. A user may choose to use a less conservative failure criterion as deemed fit for different grades of tubes and scenarios, such as a constrained economic environment with ageing infrastructures.
3. However, the FFS failure prediction of all the tubes based on the three recommended load factors by ASME, BS, and EN occur much earlier than the operating pressure at which they failed in reality, which was at a load factor of 1. This shows how overly conservative the FFS methodology is in predicting the failure of the tubes. The FFS also requires a lot of input for the analysis and a more cumbersome FEA analysis, which could be very demanding and expensive. Hence, in comparison with the proposed methodology in this thesis (using the minimum remaining thickness for a specific tube grade and the failure criteria values, given the operating conditions of the tubes), a lot of computation time and resources would be saved, and the failure of the tubes would still be predicted well on time.

The easy-to-use and more efficient failure assessment framework developed will help in categorizing the severity of localized erosion defects in boiler tubes and consequently support maintenance decisions, as well as prevent the replacement of tubes that can still be safe for continued operation while in service. Having developed this failure assessment methodology, it is also necessary to examine its sensitivity with regards to changes in the flaw geometry and tube materials. Investigations carried out in this regard and their outcomes are reported in the next chapter.

7

SENSITIVITY STUDY ON THE DEVELOPED METHODOLOGY

7.1 Introduction

Although the developed methodology has been validated and demonstrated to be in good correlation with the established FFS Standard, a sensitivity study is needed to check if changes in the flaw geometries and material factors could possibly influence the proposed methodology. In this chapter, a report on how this study is carried out, the outcomes from the study and their implications will be discussed.

7.2 Sensitivity Study Set-Up

7.2.1 Selection of tubes for the study

From the range of the tubes grades used to develop the failure assessment methodology, as reported in Chapters 5 and 6, five different flawed tubes based on the variation of their flaw geometries are selected for this study as reported in Table 7.1. The selected tubes reasonably cover a broad range of scenarios. Figure 7.1 shows the flaw geometries of these flawed tubes.

Table 7.1: Selected localized thinned tubes used for the sensitive study, showing their dimensions, flaw geometric properties and descriptions

Tubes No	D_o (mm)	t (mm)	t_r (mm)	f_l (mm)	f_w (mm)	f_l/f_w	f_w/f_d	Flaw Description
1.	75.0	7.0	0.50	600	20	30	3.08	Longest & slender flaw
4.	47.5	5.4	1.20	400	45	8.89	10.71	Fairly large flaw
10.	63.0	5.4	0.42	310	60	5.17	12.05	Widest but short flaw
11.	38.0	3.8	0.45	500	35	14.29	10.45	Mid-range flaw
12.	33.0	3.6	0.20	20	15	4.41	1.33	Smallest flaw

7.2.2 Material properties modification for selected tubes

To carry out the sensitive study with respect to the tubes flaw geometry and material type, the material properties of all the different tube grades considered in the course of this research will have to be determined at one specific T_{ot} for all the selected tubes, to eliminate any temperature variation in the material properties. It will be recalled from the previous chapter that these tube grades were as follows: BS 3059 Grade 360, SA 210 A1, BS 3059 Grade 440, DIN 17175 15Mo3, BS 3059 Grade 360. The specific T_{ot} that will be used to conduct this study is at 350°C, which is a reasonable operating temperature for most heat resistant tubes.

From the documentation on how to generate the strength properties of the tubes as a function of temperature based on the second and third approaches, as seen in Section 5.3.1, the strength values for each of the tubes based on this new configuration used for the sensitivity study are shown in Table 7.2. While the physical properties of the tubes at the specific T_{ot} are deduced from Section 5.3.2.

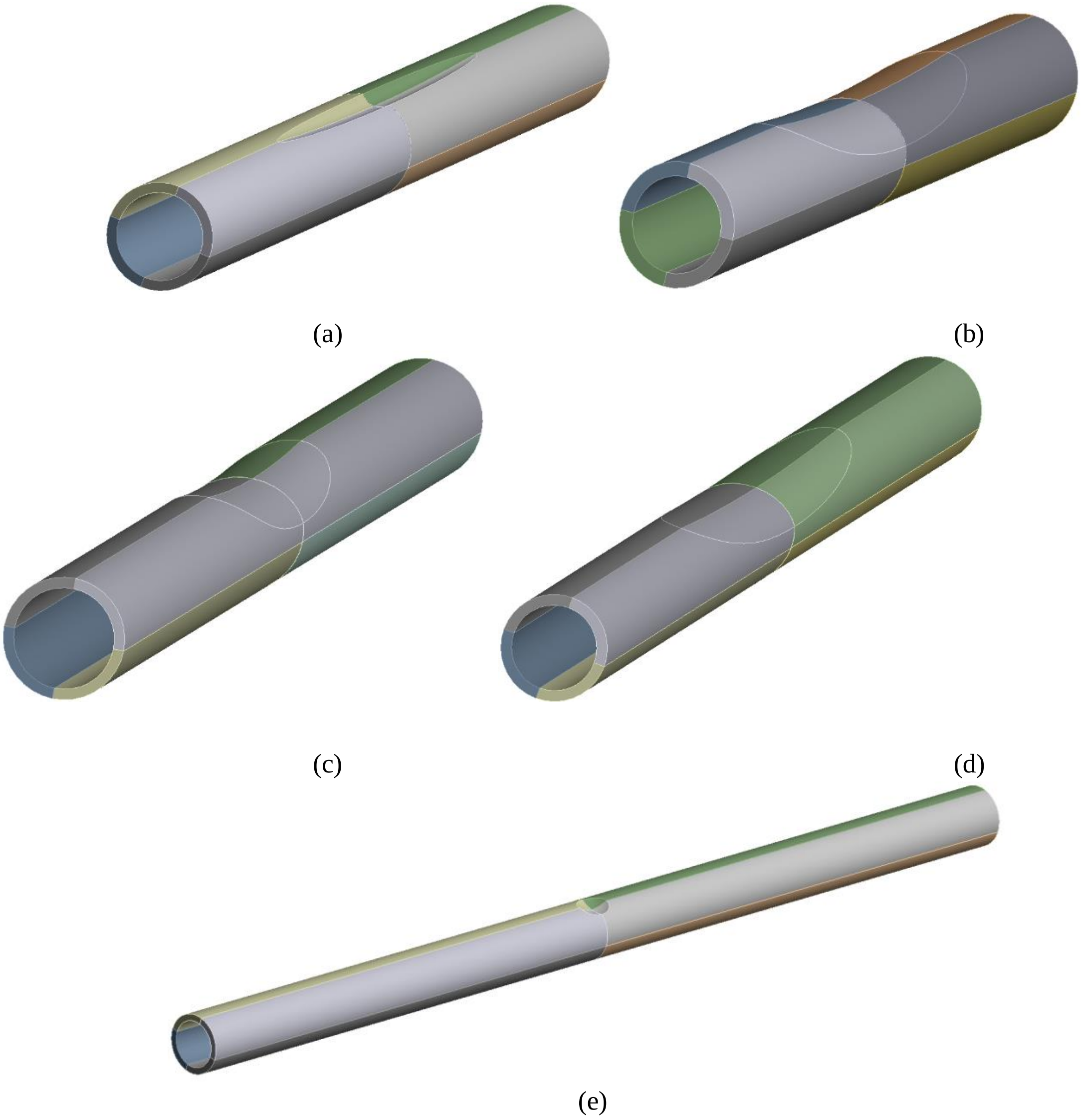

(a) (b)

(c) (d)

(e)

Figure 7.1. Flaw geometries used for the study (a) longest and slender flaw on Tube 1 (b) fairly large flaw on Tube 4 (c) widest but short flaw on Tube 10 (d) mid-range flaw on Tube 11 and (e) smallest flaw on Tube 12.

Table 7.2: Strength properties for selected tubes at specific T_{ot}

Tube Grades	T_{ot} (°C)	σ$_y$ (MPa) at T_{ot} computed using Second Approach	σ$_y$ (MPa) at T_{ot} computed using Third Approach	σ_{uts} (MPa) at T_{ot} computed using Second Approach	σ_{uts} (MPa) at T_{ot} computed using Third Approach
BS 3059 Grade 360	350	175.14	124.08	268.30	291.92
SA 210 A1	350	190.04	167.27	309.29	372.24
BS 3059 Grade 440	350	182.59	167.27	327.92	372.24
DIN 17175 15Mo3	350	242.66	165.06	404.43	393.78
BS 3059 Grade 620	350	150.94	160.66	385.74	411.99

7.2.3 Material models used for the study

The material models used for the sensitivity study are generated as described in Section 5.4 using the second and third approach strength properties. The plastic region of the developed stress-strain curves is then implemented in ANSYS® engineering data for static structural analysis. From the material curves, depicted in Figure 7.2, it is obvious that all of the stress values (except for the 15 Mo3 grades) based on the second approach strength properties are relatively less conservative to that of the third approach. As was pointed out in Section 5.4, using these two models will provide a unique advantage of having a two sided comprehensive model (one that is conservative and the other less conservative) for a detailed sensitivity analysis.

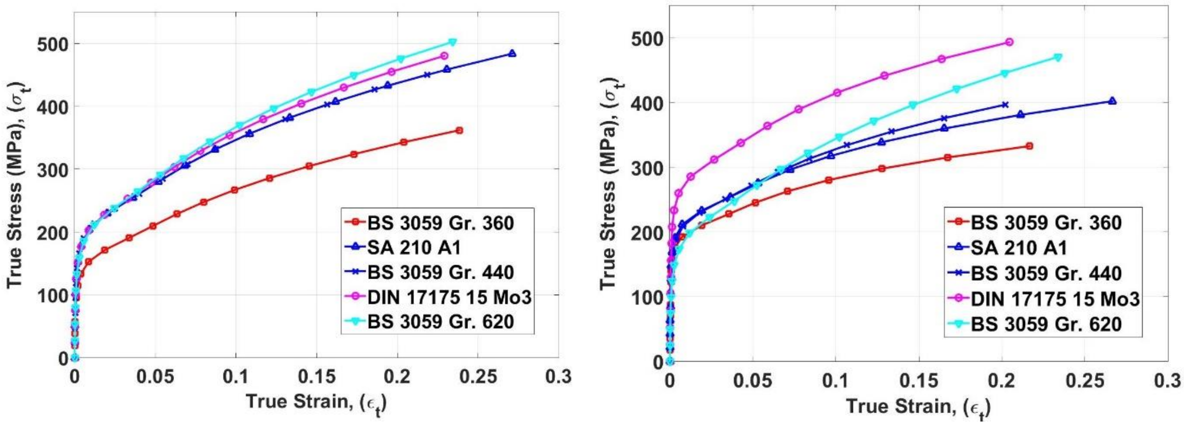

Figure 7.2: Material curves for various tube grades at the specific T_{ot} based on (a) Second approach and (b) Third approach strength properties.

7.3 Sensitivity Analysis Using the Developed Methodology

To be able to correctly analyze these tubes based on the above stated configuration and using the developed methodology, the previous P for each of the selected flawed tubes will have to be modified based on the modified material properties at the specific T_{ot}. From t_{min} as seen in. Eq. (6.1), the modified P can be computed using:

$$P = \frac{2.t_{min}.\sigma_a}{D_o - t_{min}} \tag{7.1}$$

Obtaining σ from respective standards of the tube grades and computing P for each of the tube, the complete tube parameters that are used for the sensitivity analysis are shown in Table 7.3. Finite element models of the selected tubes along with their respective parameterized models (details of the parameterized properties can be seen in Appendix G) are then solved using the computed P on ANSYS® Mechanical platform.

Table 7.3: Selected tubes parameters used for the sensitivity study

Tubes No	D_o (mm)	t_{min} (MPa)	Tube Grades	σ_a(MPa) at T_{ot}	P (MPa)
1.	75.0	5.34	BS 3059 Grade 360	87.00	13.34
			SA 210 A1	115.42	17.70
			BS 3059 Grade 440	106.00	16.25
			DIN 17175 15Mo3	120.00	18.40
			BS 3059 Grade 620	129.00	19.78
4.	47.5	4.71	BS 3059 Grade 360	87.00	19.15
			SA 210 A1	115.42	25.41
			BS 3059 Grade 440	106.00	23.34
			DIN 17175 15Mo3	120.00	26.42
			BS 3059 Grade 620	129.00	28.40
10.	63.0	3.16	BS 3059 Grade 360	87.00	9.19
			SA 210 A1	115.42	12.19
			BS 3059 Grade 440	106.00	11.20
			DIN 17175 15Mo3	120.00	12.67
			BS 3059 Grade 620	129.00	13.62
11.	38.0	2.64	BS 3059 Grade 360	87.00	12.99
			SA 210 A1	115.42	17.23
			BS 3059 Grade 440	106.00	15.83
			DIN 17175 15Mo3	120.00	17.92
			BS 3059 Grade 620	129.00	19.26
12.	33.0	2.72	BS 3059 Grade 360	87.00	15.63
			SA 210 A1	115.42	20.74
			BS 3059 Grade 440	106.00	19.04
			DIN 17175 15Mo3	120.00	21.56
			BS 3059 Grade 620	129.00	23.18

7.4 Results and Discussion

Based on the two material models used, the results of the sensitivity study are depicted in Figure 7.3 to Figure 7.6. These figures show that the third approach model is conservative, generally predicting failure relatively earlier for all the tubes compared to the second approach model, as expected. Considering the results from the less conservative model in Figure 7.3, it can be seen that the normalized equivalent Von-Mises stress ratios and plastic strain response for the normalized remaining thickness of the tubes with respect to t_{min} do not really change with the assessment result earlier reported in Section 6.3. Using the proposed $P_{5\%}$ limit, failure can be accurately predicted for all the tubes. Failure as earlier explained means that the analysis code fails to converge due to plastic strain localization and subsequent element inversion. From Figure 7.4, it can also be seen that the 0.8 σ_{uts} proposed criteria is a reasonably safe limit for these tubes. Thus, it can be seen that in spite of changes in the flaw geometries and tube materials, the proposed methodology is not affected.

The sensitivity results in Figure 7.3 and Figure 7.4 also reveal that the tubes with DIN 15 M03 tube grades fail at the lowest stress and strain. This is followed by the three BS 3059 tube grades and the SA 210 tube grades, which though have relatively higher normalized equivalent stress ratios than other tube grades. But based on the equivalent plastic strains, the BS 3059 620 grade exhibits the highest plastic strains at failure, except for Tube 1, which exceeds the material model true ultimate tensile strain $(\varepsilon_{t,uts})$, running at high values due to ANSYS computing capability. The plastic strain difference at failure between the BS 3059 620 and SA 210 grade for all the tubes ranges from ~2.5% to 4%, with Tube 12 at the upper bound, while no difference is seen with Tube 4. The reason for this is traceable to the strain hardenability of the grade, even at elevated temperature, as seen from the research on the strength properties of the tubes in Section 5.3.1. The implication of this result is that for most of the heat resistant tubes under localized erosion, those with BS 3059 620 grades due to their strain hardenability, will be able to sustain relatively higher plastic strains compared to their counterpart grades.

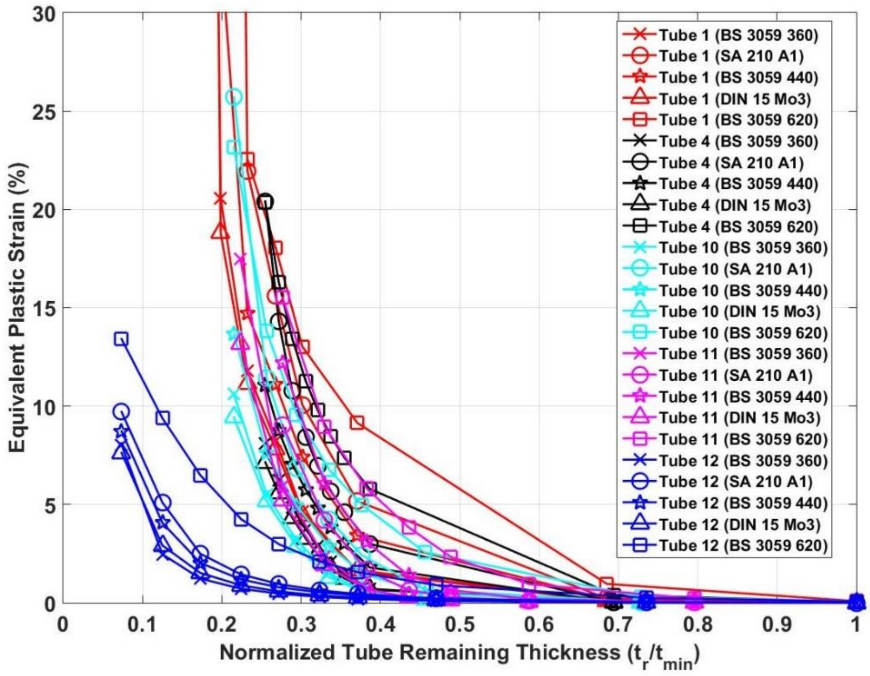

Figure 7.3: Plastic strain and normalized remaining thickness sensitivity result based on the second material model

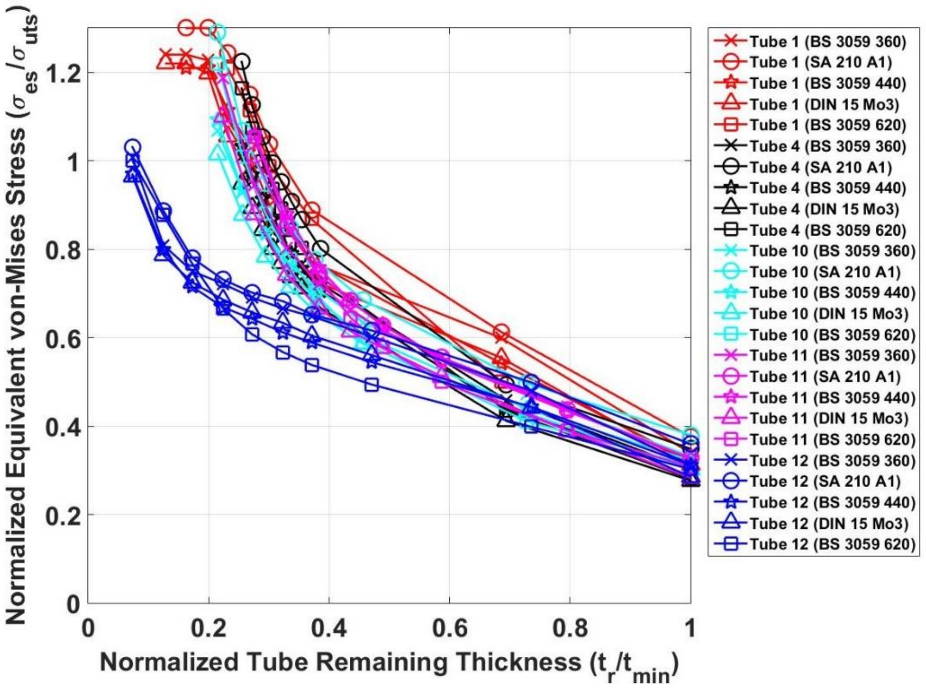

Figure 7.4: Von Mises stress with respect to σ_{uts} and normalized remaining thickness sensitivity result based on the second material model

For the BS 3059 grades of the fairly large and mid-range flawed tubes (Tubes, 4, 10 and 11), the sensitivity study shows that BS 3059 620 tube grade has the highest normalized stress ratio and plastic strain, followed by the BS 3059 440 and the BS 3059 360 tube grades. This finding can be attributed to the material composition of these tube grades. Also referring to the earlier report from the research on strength properties of the tubes in Section 5.3.1, the BS 3059 360 grade is essentially carbon steel and has the lowest strain hardening capability, while the BS 3059 440 grade, a medium carbon steel and BS 3059 620 grade, an alloyed steel have better strain hardenability.

The results so far give useful insights into the effect different grades of heat resistant tubes could pose on the tubes as they deform in service, which will evidently help to provide guidance with taking proactive measures for the maintenance of the tubes.

Based on the third approach model in Figure 7.5 and Figure 7.6, the results also showed no appreciable changes with the outcomes of the assessment earlier reported in Section 6.3. Using the proposed $P_{5\%}$ and 0.8 σ_{uts}, all the tubes are seen to be within the safe limit. This again shows that proposed methodology is not affected by changes in the geometry of the flaws and tube materials. The results also indicates that the BS 3059 620 tube grade sustained relatively higher plastic strains at failure and normalized stress ratios than other tube grades, with the exception of the BS 3059 360 grade for Tube 1, which exceeds the material model true ultimate tensile strain $(\varepsilon_{t,uts})$, and continued solving at high plastic strain values due to ANSYS computing capability. It could be recalled from the earlier report based on the less conservative second approach model, that the BS 3059 620 grade also showed high plastic strain at failure and stress ratios for most of the tubes. Based on this, the result from this conservative model, thus, substantiates this finding.

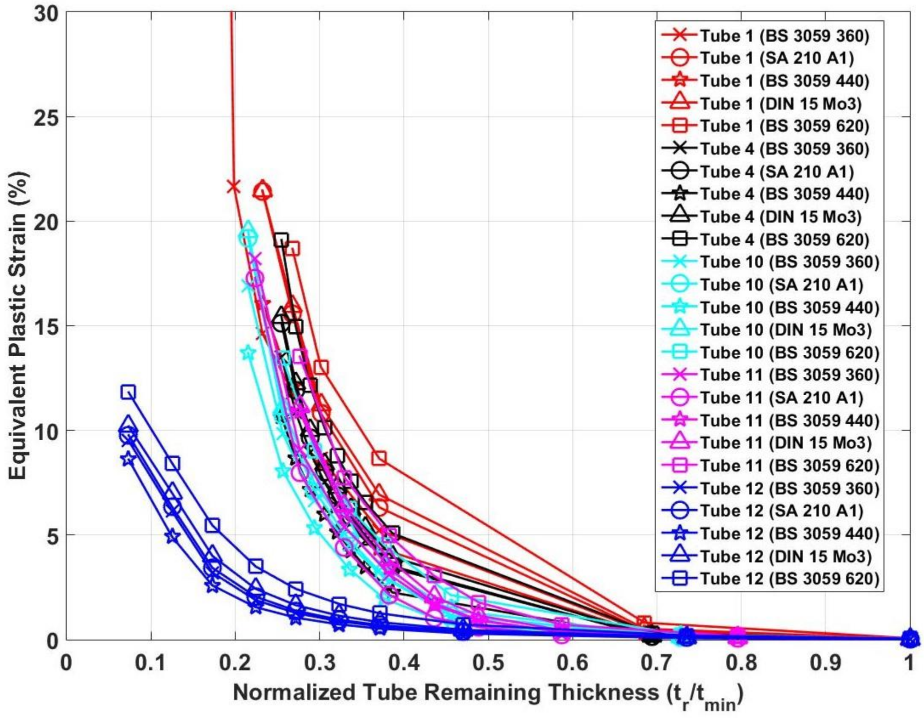

Figure 7.5: Plastic strain and normalized remaining thickness sensitivity result based on the third material model

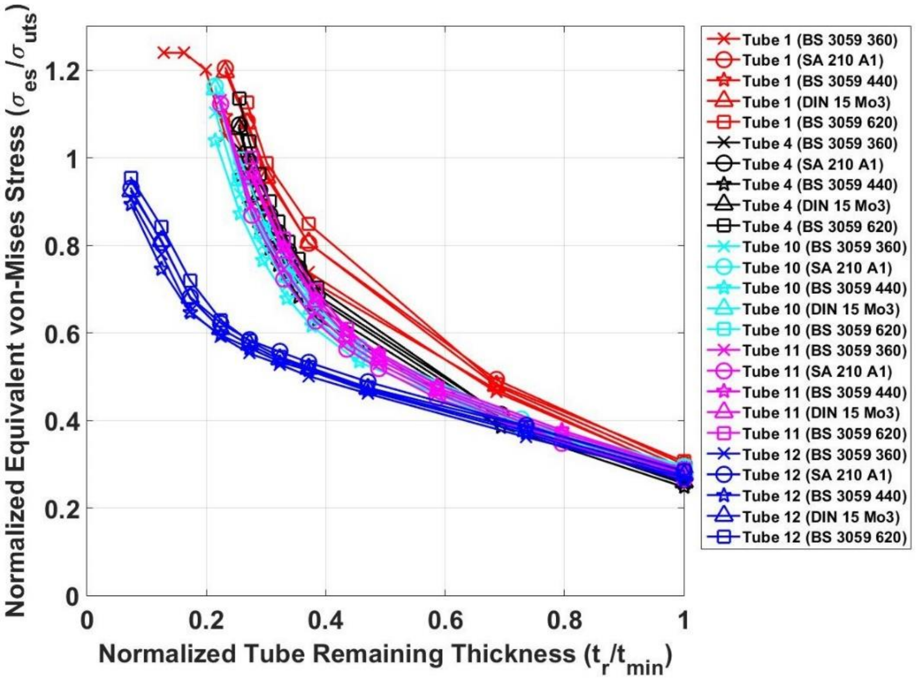

Figure 7.6: Von Mises stress with respect to σ_{uts} and normalized remaining thickness sensitivity result based on the third material model

Equally, from Figure 7.5 and Figure 7.6, the results of the conservative third approach model, which has less variation between the material curves demonstrates an improved safety prediction for the DIN 15 M03 tube grades compared to that seen with the second approach model. The BS 3059 620 tube grades also have the highest strain and stress ratios before failure (as also seen with the second approach), followed by the DIN 15 Mo3, the SA210, the BS 3059 360, and the BS 3059 440 tube grades. This outcome can be attributed to the influence of the conservative model on the strain hardenability of these tubes. Their strain hardenability become quite conservative when compared to their (engineering strength values or the true stress values of the less conservative model) at elevated temperature, as seen in Sections 5.3.1 and 5.4.

The distinction between Tube 12 and other flawed tubes is also visibly noticed in all the figures (Figure 7.3 to Figure 7.6) from the two models used, with the flawed tube still able to sustain itself at very low tube remaining thickness ratio of ~0.075 though at a lower normalized stress and strain ratios. The rationale for this is ascribable to the flaw small size, which will first create substantial strain concentration within the flaw area as the tube deforms while in use. But over time, the concentration effect reduces, as it become largely absorbed by the substantial elastic material around the flaw. This ends up reducing the stress and strain ratios within the tube, while sustaining it in service before it eventually fails at a very low ratio of the tube remaining thickness. In contrast, other flawed tubes are not able to attain this low ratio, as they all failed at about 20% of their remaining thicknesses or more. Similar to the results in Chapter 4 and 6, these findings give further understanding of how sensitive the tubes are to their flaw geometry.

The insights from this sensitivity analysis provides us with a deeper understanding of the interplay between the various grades of commonly used heat resistant tubes and their failure under localized external erosion.

7.5 Summary and Conclusions

This chapter presents the report of the sensitivity study based on the developed methodology carried out on some carefully selected localized thinned tubes from the set of real flawed tubes used as case study for this research. Five different flawed tubes based on the variation of their flaw geometries were selected for this study. The tubes reasonably cover a broad range of scenarios (from smallest through mid-range flaws to longest and slender flaws). The sensitivity study was done to examine how the combination of the flaw geometry and material factors could possibly influence the failure of the tubes while in use, using the developed methodology.

For the set-up of this study, the material properties of the five grades (BS 3059 Grade 360, SA 210 A1, BS 3059 Grade 440, DIN 17175 15Mo3, BS 3059 Grade 360) of the tubes were modified at a fixed operating temperature T_{ot} of 350℃ to eliminate the effect of any temperature variation on the material properties of the selected tubes. The modification of these properties was carried out using two different approaches, from which two material models (one that is conservative and the other less conservative) were generated and used for the sensitivity analysis.

In order to analyze these tubes correctly based on the modified configuration and using the already developed methodology, the previous P for each of the selected flawed tubes were modified at the specific T_{ot}. Finite element models of the selected tubes along with their respective parameterized models were then solved using the modified P in ANSYS®.

Based on the results from the sensitivity study using the two material models, it was seen that changes in the flaw geometries and tube materials did not really affect the normalized Von-Mises Stress ratios and plastic strain response for the normalized remaining thickness of the tubes with respect to t_{min}. The proposed $P_{5\%}$ limit correctly predicted the failure for all the tubes. The 0.8 σ_{uts} proposed criteria also was a reasonably safe limit for the tubes.

The results from the second approach model (less conservative model) also indicated that the DIN 15 M03 tube grades fail at the lowest stress and strain, which was followed by the three BS 3059 tube grades and the SA 210 tube grades that had relatively higher normalized equivalent stress ratios than other tube grades. However, the BS 3059 620 grade exhibits the highest plastic strains at failure. Similarly, the results based on the third approach model substantiated this finding, as the BS 3059 620 grade sustained relatively higher plastic strains at failure and normalized equivalent stress ratios than the other tube grades. The reason for this could be linked to the strain hardenability of the grade, even at elevated temperature. The implication of this result is that for most heat resistant tubes under localized erosion, those with BS 3059 620 grades, will be able to sustain relatively higher plastic strains compared to their counterpart grades due to their improved strain hardenability.

From the less conservative model results of the BS 3059 grades of mid-range and fairly large flawed tubes, the sensitivity study shows that BS 3059 360 had the lowest normalized stress ratio and plastic strain, followed by the BS 3059 440 and then the BS 3059 620 grades. This finding can be attributed to the material composition of these tube grades, in which the BS 3059 360 grades are carbon steel materials and had the lowest strain hardenability, while the

BS 3059 440 grades, a medium carbon steel and BS 3059 620, an alloyed steel had better strain hardenability.

It is also worth mentioning that the results of the third approach model had improved safety prediction for the DIN 15 M03 tube grades compared to that which was seen with the second approach model. The BS 3059 620 tube grades, as was seen with the second approach model, had the highest strain and stress ratios before failure, followed by the DIN 15 Mo3, the SA 210, the BS 3059 360, and the BS 3059 440 tube grades. The outcome of this result was based on the effect of the conservative model on the strain hardenability of these tube grades, making them quite conservative when compared to their engineering strength values or the true stress values of the second approach model at elevated temperature.

Finally, the distinction between the tube with the smallest flaw and other flawed tubes was clearly seen from all the results of the two models used, with the tube still able to sustain itself at very low tube remaining thickness ratio of ~0.075 though at a lower normalized stress and strain ratio. This was due to the small size of the flaw, which will first create substantial elastic strain concentration within the flaw area as the tube deforms while in use. But as the load increases, the effect of this strong elastic stress concentration reduces due to the relatively large surrounding material around the flaw that remains in the elastic domain. This ultimately reduces the stress and strain ratios within the tube, while sustaining it in service before it eventually fails at a very low ratio of the tube remaining thickness. Contrary, other flawed tubes failed at about 20% of their remaining thicknesses and more. These findings give further understanding of how sensitive the tubes are to their flaw geometry.

The above results from this study give useful insights into how sensitive the in-service behavior of an externally eroded tube is when using different grades of heat resistant tubes. They provide deeper understanding of the interplay around the various grades of commonly used heat resistant tubes in relation to their failure under localized external erosion. These findings will help to provide guidance with taking proactive measures for the maintenance of the tubes.

8 CONCLUSIONS AND RECOMMENDATIONS

8.1 Summary of Thesis

Boiler tubes used in power plants, manufacturing and processing industries usually operate in an erosive-corrosive and high temperature environment and as such are exposed to a broad range of failures while in use. One of the most common tube failure mechanisms in these industries is localized external erosion, wherein the tube undergoes considerable loss of its wall thickness within a localized area under the influence of some erosive components within the plant. As time passes, the localized thinning of tube evolves into gross plastic deformation, leading to the eventual bursting of the tube. This failure has been a leading cause of tube leakages, availability loss and unscheduled boiler outages in the relevant industries, usually resulting in loss of production and unplanned expensive repairs.

Even though this problem has received attention over the years, most of the studies on the tubes have been centered on metallurgical failure investigations, visual inspections, chemical composition and microstructural analyses to determine the root cause of the failure and in some cases propose recommendations for preventive measures. A few studies have tried to estimate to the tube remaining life, while others have proposed guidelines to prevent the erosive particles from the combustion chamber of the plant from impinging on the tubes. In spite of these efforts, the problem of localized external erosion in boiler tubes continues to be a leading cause of tube leakages and unscheduled boiler outages in power plants and other utilities.

The American Petroleum Institute (API) and the American Society of Mechanical Engineers (ASME) also developed a standard document to provide guidance in conducting fitness-for-service assessments of pressurized vessels and their components, containing a damage or flaw while in service. But this has also had its challenges, which includes: the assessment requiring a detailed inspection and many input details, cumbersome FEA simulations that are needed for the highest level of assessment, which is only considered as the most reliable for severe flaw assessment, and also the concept of factored loads used for the assessment that have possibilities of giving relatively conservative results, which could lead to replacing tubes that still could continue to be safe for operation.

Based on the aforementioned, there has been, therefore, a need to approach this persistent problem from a different perspective and engage in further studies that will lead to a rapid decision making tool to assess the flaws and prioritize their repairs or replacement. This is especially crucial in a constrained economic environment with ageing infrastructure, where one does not want to replace flawed tubes that could still be safe for continued service, while also avoiding their unexpected failure and all the already mentioned negative issues associated with their failure. Therefore, a procedure is required that can rank detected flaws from most likely to fail to least likely to fail. It is for this reason that a series of detailed studies were performed and reported in this thesis to provide a pragmatic solution to this problem.

In the first chapter of the thesis, a general background and motivation for the study on localized external erosion in boiler tubes was reported. The aims and research objectives were clearly spelt out and the scope of the research was also well defined.

The second chapter gave an account of the literature on this topic, beginning with a review of the initial studies that led to the development of different failure assessment methodologies and criteria for pressure vessels. A detailed review of the methodologies and criteria that could predict the failure of these vessels while in service was presented. In addition, previous numerical studies on localized external erosion in boiler tubes were reported. The ASME and API fitness-for-service assessment guides were also discussed and the challenges inherent in them were discussed. From the literature review, it was evident that though metallurgical investigations and finite element studies have been done to determine the root cause of these failures and also provide some preventive measures to avoid their reoccurrence, a focused study on which flaws in boiler tubes are most at risk of failure due to plastic collapse has not been done.

Based on this background, it was apparent that more detailed studies were needed to able to rank detected flaws from most severe to least severe. This would allow operators to optimize the available budget to focus attention where necessary, reducing the likelihood of unexpected outages. Thus, the third chapter of this thesis reported on the initial investigation of localized external eroded tubes, which was the modelling of tubes with variants of conceptualized localized external flaw geometries that exist in real scenarios. The geometric definitions of these flaws to aid in the process of replicating real tubes on the conceptualized models was also discussed.

Chapter Four presented the report on comprehensive studies carried out on the modelled localized external eroded tubes. The outcome of these investigations provided useful insights into the factors that influence the failure of these tubes while in use. It was inferred from the studies that beyond the material removal associated with localized external erosion, the elastic stress concentration and flaw geometry play critical roles in influencing the failure of tubes. The failure pressures of the modelled tubes were analyzed using a range of failure criteria, to determine which failure criterion would be best recommended for the failure assessment of the locally flawed tubes. Based on the result, 7.5% plastic strain or 5% plastic strain criteria were proposed because they had lower failure pressures that were reasonably safe from the extreme benchmark failure criterion of 20% plastic strain. These criteria were safer options to guard against unexpected failures of the tubes, while also trying to avoid being overly conservative with using the lowest 2% plastic strain criterion.

Insights gained from the studies carried out on conceptualized variants of localized thinned tubes in Chapter Four were extended to 16 real examples of failed externally eroded tubes obtained from the power generation industry, representing 5 different tube materials. Chapter Five reported on the methodology to obtain realistic material properties and models from design codes. A detailed assessment of the strength and physical properties of a range of commonly used heat resistant boiler tubes in fossil-fuel industries, operating within high temperature and pressure environments while in service were carried out. The material properties for each tube material were used to generate two distinct true stress-strain hardening material models based on the Material Properties Council (MPC) stress-strain models. This was to ensure that the effect of strain hardening in the tubes as they deform plastically was properly captured in the failure assessment. Previous published papers had not taken this into consideration, and some had used elastic-perfectly plastic models.

The Sixth chapter reported on how the failure assessment was performed. The failed tubes were treated as an inverse problem and an optimization technique in MATLAB® was used to obtain the geometric properties of the real flaws to effectively replicate them on the already developed conceptualized geometries. For a thorough failure assessment of the tubes, 160 finite element models with the same tube and flaw dimensions but varying remaining thicknesses (t_r) were generated from the 16 tubes. Using the generated MPC material models, comprehensive Nonlinear Finite Element Analysis (NLFEA) investigations were conducted on the 160 modelled flawed tubes. These tubes were assessed based on the maximum equivalent plastic strain and Von Mises stress produced at the deepest point of the flaw area within each of the failed tubes when subjected to their respective operating pressures. The failure assessment outcome revealed that most of the heat resistant tubes while in service will remain safe if their remaining thicknesses t_r are within the range of $0.7\, t_{min}$ to t_{min}. A 5% plastic strain and equivalent Von Mises stress criteria of 0.8 σ_{uts} were deduced as appropriate failure criteria to guard against the failure of these tubes while in service, and also avoid their early replacement.

Though the assessment results of these real tubes were already implicitly validated since they were determined from the respective operating pressures at which the tubes failed, the developed methodology framework was checked and compared with the API-ASME FFS standard and found to be in good agreement with it, being also less complex, efficient and less conservative. The FFS assessment requires pressure vessels to be re-rated for a lower pressure if they do not comply with the specified load factor, imposing a severe requirement on the operator. In this analysis, rather than varying the operating pressure, the remaining tube thickness was varied, and a thickness-based failure criterion was proposed.

Chapter Seven of the thesis reported on a sensitivity study to examine how the combination of the flaw geometry and material factors could possibly influence the failure of the tubes while in use, using the developed methodology. This sensitivity study aimed to demonstrate that the results from Chapter Six are generalizable. This was carried out on five carefully selected localized thinned tubes from the set of real flawed tubes that were used as case study for this research. The selected tubes covered a broad range of flaw geometries (from small and deep, through mid-range flaws to a long and slender flaw). These five flaw geometries were combined with the five tube materials to generate 25 analyses. The material properties of the five grades of the tubes used for the study were modified at a fixed operating temperature T_{ot} of 350℃ to eliminate the effect of any temperature variation on the material properties of the selected tubes. Just as in chapter Four, two MPC material models (one that is conservative and the other less conservative) were used for the sensitivity analysis.The previous operating pressures P for each of the selected flawed tubes were modified at the specific T_{ot}. Finite element models of the selected tubes along with their respective parameterized models were then solved using the modified P in ANSYS®.

From the results of the sensitivity study using the two material models, it was seen that the normalized stress ratio and the plastic strain response for the normalized remaining thickness of the tubes with respect to t_{min}, were not remarkably affected by changes in the flaw geometries and tube materials. The proposed $P_{5\%}$ and 0.8 σ_{uts} limits accurately predicted the failure for all the tubes and were reasonably safe limit for the tubes.

The results using the less conservative model (the second approach) also revealed that the DIN 15 Mo3 tube grades fail at the lowest stress ratios and strain, which was followed by the three

BS 3059 tube grades and the SA 210 tube grades. The BS 3059 620 tube grade (one of the BS 3059 tube grades) had the highest plastic strain at failure. The outcome of the result showed that for most of the heat resistant tubes under localized erosion, those made from BS 3059 620 will be able to sustain relatively higher plastic strains compared to their counterparts due to the higher strain hardenability. The effect of the strain hardenability for the BS 3059 360, 440 and 620 grades of mid-range and fairly large flawed tubes were also apparent. The conservative results obtained using the third approach material model, which had less variation between the material curves, accordingly, showed less variation in the stress ratios and strain at failure. The highest values were observed with the BS 3059 620 material, followed by the DIN 15 Mo3, the SA 210 and the BS 3059 360 tube grades. The BS 3059 440 tube grades had the lowest values. Again, this was due to the variations in the strain hardenability of these materials.

The distinction between the tube with the smallest flaw and other flawed tubes was clearly seen from both results, as the tube was able to sustain itself at very low tube remaining thickness ratio of ~0.075 though at a lower normalized stress and strain ratios. Other flawed tubes failed at about 20% of their remaining thicknesses.

In general, the sensitivity study clearly shows that the conclusions from the failure assessments do not change if we use different geometries or materials. All the above gained insights from this sensitivity study will help to support maintenance decisions on these tubes while in service.

8.2 Conclusions

In this thesis, detailed studies were performed and reported to provide a rapid decision making tool for assessing and ranking localized external erosion defects in boiler tubes, so as to prioritize their repairs or replacement.

The outcome of the comprehensive research done provided useful insights into the mechanical behaviour of localized external erosion flaws and the factors that could possibly influence the failure of the tubes. Conceptualized variants of localized thinned tubes with geometries that could realistically occur in practical scenarios were modelled. Previous FEA studies on boiler tubes were performed with less precise flaw geometries. Also, the insights gained from the explicit investigations on these factors are useful in providing some guidance in categorizing detected flaws on tubes while in use from most severe to least severe. This enables proper planning of which flawed tubes should be repaired or replaced before the next scheduled shut down of the plant. Consequently, this will help to optimize the available budget and maintenance resources, and also focus attention where absolutely necessary.

A new, easy-to-use and efficient failure assessment methodology framework was developed from extensive NLFEA investigations carried out on real failed tubes obtained from the power plant. The failure assessment was conducted by treating the tubes as an inverse problem and using an optimization technique to obtain the flaw geometric properties of the real tubes so as to effectively replicate them on the developed conceptualized models. MPC material models that enabled the effect of strain hardening to be properly captured in the tubes as they deform were used for the analysis. The developed methodology is distinctive, as previous proposed methods did not use this approach before nor captured the effect of strain hardening in the tubes in this reported manner. The assessment outcome led to the establishment of a plastic strain and stress limit criteria that can be employed to heat resistant seamless tubes to ensure they remain safe for continued operation, while avoiding their early replacement. The methodology proposed mainly require a minimum remaining thickness for a specific tube grade, the operating pressure and temperature to perform a localized external erosion failure assessment on the fitness-for-service of any tube in operation. The methodology was checked and compared with the API-ASME fitness-for-service assessment and found to be in good correlation with it, also easy to use, more efficient and with reduced conservatism.

Sensitivity studies were also conducted based on the developed methodology to examine how the combination of the flaw geometry and material factors could possibly influence the failure of the tubes while in use. The study outcome shows that there were no appreciable changes in the normalized Von-Mises stress ratios and the plastic strain response for the normalized remaining thickness of the tubes. The proposed $P_{5\%}$ and 0.8 σ_{uts} limits accurately predicted the failure for all the tubes and were reasonably safe limit for the tubes. Insights gained from the strain hardenability of the tubes studied will also help with making timely and suitable decisions on the maintenance of the tubes.

Finally, the technique that has been developed in this thesis will help to rank detected flaws from most severe to least severe. So in a constrained economic climate, whatever the maintenance budget permits, the technique will enable the most severe flaws to be repaired first. This will hopefully enable the plant to operate until the next planned outage, or at least maximize the time to failure.

8.3 Recommendations

For further implementation of this research, especially for the interest of the power generation industry, it would be recommended that the developed methodology framework presented in this thesis be configured into an app or a graphical user interface. So that by inputting the tube and measured flaw geometry, as well as the material properties and operating conditions of the tubes, the user can get a prompt feedback if the tube can be safe for continued operation or not.

Since this research was focused on providing a rapid decision making tool to aid in prioritizing the repair and replacement to one of the prevalent problems associated with boiler tubes, there are still other failures that should be attended to (such as, cracks, corrosion, fatigue, creep, etc.). Further studies are needed to gain more insights on managing them effectively and also develop easy-to-use and improved failure assessment methodology for them, just as it has been done with localized external erosion.

References

[1] S. Chaudhuri, Some aspects of metallurgical assessment of boiler tubes — Basic principles and case studies, Materials Science and Engineering A. 432 (2006) 90–99.

[2] Cleaver-Brooks Inc., Boiler Room Guide, 2013.

[3] A. ZG, Boiler and Vessels; Steam bolier manufacturers in Czech, ZG. (2015). https://www.zgsteamboiler.com/project/steam-boiler-manufacturer-in-czech.html (accessed September 14, 2018).

[4] C.B. Clifford, T.P.S. University, EGEE 439 Alternative Fuels from Biomass Sources: Production of Steam - Fuel, Penn State College of Earth and Mineral Sciences, The J A Dutton e-Educational Institute. (2018). https://www.e-education.psu.edu/egee439/node/584 (accessed September 14, 2018).

[5] M.M. Rahman, J. Purbolaksono, J. Ahmad, Root cause failure analysis of a division wall superheater tube of a coal-fired power station, Engineering Failure Analysis. 17 (2010) 1490–1494.

[6] D.N. French, Metallurgical failures in fossil fired boilers, John Wiley and Sons, Inc. (1993).

[7] B. Dooley, P.S. Chang, The current state of boiler tube failures in fossil plants, PowerPlant Chemistry. 2 (2000) 197–203.

[8] S.R. Bamrotwar, V.S. Deshpande, Root cause analysis and economic implication of boiler tube failures in 210 MW thermal power plant, IOSR Journal of Mechanical and Civil Engineering. (2014) 6–10.

[9] S.R.K. Dhamangaonkar, M.R. Nandgaonkar, A. Deshmukh, A. Deshmukh, S. Thakur, Use of cold air velocity test (CAVT) to locate erosion prone zones in pulverized coal fired utility boiler, in: Proceedings of the World Congress on Engineering, 2011.

[10] K. Zarrabi, Estimation of boiler tube life in presence of corrosion and erosion processes, International Journal of Pressure Vessels & Piping. 53 (1993) 351–358.

[11] K. Zarrabi, H. Zhang, Creep and plastic collapse lives of scarred boiler tubes, Materials at High Temperatures. 15 (1998) 389–393.

[12] ASM Handbook Committee, Failure Analysis and Prevention, 2002.

[13] J.F. Drennen, P. Kratina, Guidelines for control and prevention of fly ash erosion in fossil fired power plants. Final report by EPRI, USA., 1994.

[14] J. Roy-Aikins, Challenges in meeting the electricity needs of South Africa, in:

Proceedings of the ASME 2016 Power and Energy Conference, 2016: p. V001T05A002.

[15] G.P. Sullivan, R. Pugh, A.P. Melendez, W.D. Hunt, Operations and maintenance best practices: A guide to achieving operational efficiency, 2010.

[16] K. Zarrabi, A comparison of several boiler tube life prediction methods, International Journal of Pressure Vessels & Piping Vessels & Piping. 58 (1994) 197–201.

[17] S.W. Liu, W.Z. Wang, C.J. Liu, Failure analysis of the boiler water-wall tube, Case Studies in Engineering Failure Analysis. 9 (2017) 35–39.

[18] M. Suckling, C. Allen, Critical variables in high temperature erosive wear, Wear. 203–204 (1997) 528–536.

[19] P. Haribhakti, P.B. Joshi, R. Kumar, Failure Investigation of Boiler Tubes: A Comprehensive Approach, ASM International, 2018.

[20] Electric Power Research Institute (EPRI), Guidelines for control and prevention of fly ash erosion, 2011.

[21] K. Zarrabi, H. Zhang, Primary stress in scarred boiler tubes, International Journal of Pressure Vessels and Piping. 65 (1996) 157–161.

[22] M. Suckling, High temperature erosive wear of a boiler tube steel, PhD Thesis, University of Capetown. (1996) 190.

[23] R.D. Port, H.M. Herro, D. Robert, The Nalco Guide to Boiler Failure Analysis by Nalco Chemical Company, 1991.

[24] ESKOM, BTFR mechanism short report: TUT/13/005/UCLF, 2012.

[25] F.-J. Chen, C. Yao, Z. Yang, Failure analysis on abnormal wall thinning of heat-transfer titanium tubes of condensers in nuclear power plant Part II: Erosion and cavitation corrosion, Engineering Failure Analysis. 37 (2014) 42–52.

[26] A.K. Pramanick, G. Das, S.K. Das, M. Ghosh, Failure investigation of super heater tubes of coal fired power plant, Case Studies in Engineering Failure Analysis. 9 (2017) 17–26.

[27] J. Ahmad, J. Purbolaksono, L.C. Beng, A.Z. Rashid, A. Khinani, A.A. Ali, Failure investigation on rear water wall tube of boiler, Engineering Failure Analysis. 16 (2009) 2325–2332.

[28] S.K. Dhua, Metallurgical investigation of failed boiler water-wall tubes received from a thermal power station, Engineering Failure Analysis. 17 (2010) 1572–1579.

[29] N. Lee, S. Kim, B. Choe, K. Yoon, D. Kwon, Failure analysis of a boiler tube in USC coal power plant, Engineering Failure Analysis. 16 (2009) 2031–2035.

[30] Y. Gong, Z. Yang, J. Yuan, Failure analysis of leakage on titanium tubes within heat exchangers in a nuclear power plant. Part II : Mechanical degradation, Materials and Corrosion. 63 (2012) 18–28.

[31] I. Klevtsov, H. Tallermo, T. Bojarinova, A. Dedov, Assessment of remaining life of superheater austenitic steel tubes in oil shale PF boilers, Oil Shale. 23 (2006) 267–274.

[32] O. Nau, N.I. Rad, G. Baki, B. Raji, B. An, Prediction and prevention of boiler tubing systems erosion in thermal plant, Tehnicka Dijagnostika. (2010) 3–9.

[33] American Petroleum Institute (API) and the American Society of Mechanical Engineers (ASME), Fitness-For-Service API 579-1/ASME FFS-1, 2016.

[34] American Society of Mechanical Engineers (ASME), ASME Boiler and Pressure Vessel Code, Division 2, Section VIII Rules for Construction of Pressure Vessels, 2015.

[35] M.S. Attia, M.M. Megahed, M.A. Darwish, S. Sundram, Assessment of corrosion damage acceptance criteria in API579-ASME/1 code, International Journal of Mechanics and Materials in Design. 12 (2016) 141–151.

[36] R. Peters, P. Kuhn, Burst strength of unstiffened pressure cylinders with slits, NACA TN. 3993 (1957).

[37] E.S. Folias, The stresses in a cylindrical shell containing an axial crack, 1964.

[38] E.S. Folias, An axial crack in a pressurized cylindrical shell, International Journal of Fracture Mechanics. 1 (1965) 104–113.

[39] A. Duffy, Studies of hydrostatic test levels and defect behavior, Proceedings of Symposium on Line Pipe Research, AGA. (1965).

[40] R.B. Anderson, T.L. Sullivan, Fracture mechanics of through-cracked cylindrical pressure vessels, NACA TN. D-3252 (1966).

[41] H. Kihara, K. Ikeda, H. Iwanaga, Brittle fracture initiation of line pipe, Presented at International Institute of Welding, Delft. (1966).

[42] W. Crichlow, R. Wells, Crack propagation and residual static strength of fatigue-cracked titanium and steel cylinders, ASTM STP 415, American Society for Testing and Materials. (1967) 25.

[43] G.T. Hahn, M. Sarrate, A.R. Rosenfield, Criteria for crack extension in cylindrical pressure vessels, International Journal of Fracture Mechanics. 5 (1969) 187–210.

[44] M. Muscat, D. Mackenzie, R. Hamilton, A work criterion for plastic collapse, 80 (2003) 49–58.

[45] P.M.A. Mackenzie, C.A. Walker, J. Mckelvie, A method for evaluating the mechanical

performance of thin-walled titanium tubes, Thin-Walled Structures. 45 (2007) 400–406.

[46] C.H.A. Townley, G.E. Findlay, M.A. Goodman, P. Stanley, Elastic-Plastic computations as a basis for design charts for torispherical pressure vessel ends, Proceedings of the Institution of Mechanical Engineers. 185 63/71 (1971) 869–877.

[47] M. Save, Experimental verification of plastic limit analysis of torispherical and toriconical heads, Pressure Vessels and Piping: Design Analysis. ASME Vol 1 (1972) 382–416.

[48] The American Society of Mechanical Engineers (ASME), American Society Mechanical Engineers, New York, NY, USA, ASME Boiler and Pressure Vessel Code; Section III. Division 1. (1971).

[49] The American Society of Mechanical Engineers (ASME), American Society of Mechanical Engineers, New York, NY, USA, ASME Boiler and Pressure Vessel Code; Section III. Division 1. (1974).

[50] ASME, American Society Mechanical Engineers, New York, NY, USA, ASME Boiler and Pressure Vessel Code; Section III. Division 1. (2007).

[51] J.C. Gerdeen, A critical evaluation of plastic behaviour data and a united definition of plastic loads for pressure components., WRC Bulletin. 254 (1979).

[52] ANSI-ASME B31G-1984, Manual for determining the remaining strength of corroded pipelines, American Society of Mechanical Engineers, New York, NY, USA. (1984).

[53] J.F. Kiefner, P.H. Vieth, A modified criterion for evaluating the remaining strength of corroded pipe, American Gas Association, PR-3-805, 1989.

[54] ANSI-ASME B31G-1991:, Manual for determining the remaining strength of corroded pipelines, American Society of Mechanical Engineers, New York, NY, USA. (1991).

[55] D.R. Stephens, P. Krishnaswamy, R. Mohan, D. Osage, G.M. Wilkowski, A review of analysis methods and acceptance criteria for local thinned areas in piping and piping components, in: Fitness for Adverse Environments in Petroleum and Power Equipment ASME PVP-Vol. 359, 1997: pp. 55–65.

[56] B.N. Leis, D.R. Stephens, An alternative approach to assess the integrity of corroded line pipe - Part I : Current status, Proc. of the 7th International Offshore & Polar Eng. Conf. IV (1997) 624–634.

[57] B.N. Leis, D.R. Stephens, An alternative approach to assess the integrity of corroded line pipe - Part II : Alternative criterion, Proc. of the 7th International Offshore & Polar Eng. Conf. IV (1997) 635–641.

[58] D.R. Stephens, B.N. Leis, Material and geometry factors controlling failure of corrosion defects in piping, in: International Pressure Vessels and Piping Conference, 1997.

[59] Recommended Practice, DET NORSKE VERITAS, DNV-RP-F101, Corroded Pipelines. (2004).

[60] E.Q. Andrade, A.C. Benjamin, Modified method for the assessment of the remaining strength of corroded pipelines, IBP413-03, Rio Pipeline Conference & Exposition. (2003).

[61] G. Chell, Application of the CEGB Failure Assessment Procedure, R6, to Surface Flaws, Fracture Mechanics: Twenty-First Symposium. (2009) 525-525–20. doi:10.1520/stp19012s.

[62] M. Kanninen, K. Pagalthivarthi, A theoretical analysis for the residual strength of corroded gas and oil transmission pipelines, in: Proceedings of Symposium on Corrosion Forms and Control for Infrastructure, 1991.

[63] D. Ritchie, S. Last, Burst criteria of corroded pipelines-defect acceptance criteria, Proceedings of the EPRG/PRC 10th Biennial Joint Conference. (1995).

[64] J.R. Sims, B.F. Hantz, K.E. Kuehn, A basis for the fitness for service evaluation, Pressure Vessel Fracture, Fatigue, and Life Managment, ASME PVP. 233 (1992) 51–58.

[65] B.F. Hantz, J.R. Sims, C.T. Kenyon, T.A. Turbak, Fitness for service: Groove-like local thin-areas on pressure vessels and storage tanks, Plant Systems/Components Aging Management, ASME PVP. 252 (1993).

[66] D.-J. Shim, J. Choi, Y. Kim, Failure strength assessment of pipes with local wall thinning under combined loading based on finite element analyses, Journal of Pressure Vesssel Technology. 126 (2004) 179–183.

[67] D.-J. Shim, Y.-J. Kim, Y.-J. Kim, Reference stress based approach to predict failure strength of pipes with local wall thinning under combined loading, Transactions of the ASME. 127 (2005) 76–83.

[68] G. Fekete, L. Varga, The effect of the width to length ratios of corrosion defects on the burst pressures of transmission pipelines, Engineering Failure Analysis. 21 (2012) 21–30.

[69] J.E. Abdalla Filho, R.D. Machado, R.J. Bertin, M.D. Valentini, On the failure pressure of pipelines containing wall reduction and isolated pit corrosion defects, Computers and Structures. 132 (2014) 22–33.

[70] K.J. Yeom, Y.-K. Lee, K.-H. Oh, W.-S. Kim, Integrity assessment of a corroded API X70 pipe with a single defect by burst pressure analysis, Engineering Failure Analysis. 57 (2015) 553–561.

[71] J.W. Kim, C.Y. Park, S.H. Lee, Local failure criteria for wall-thinning defect in piping components based on simulated specimen and real-scale pipe tests, in: 20th International Conference on Structural Mechanics in Reactor Technology (SMiRT 20), 2009: pp. 1–14.

[72] B. Ma, J. Shuai, D. Liu, K. Xu, Assessment on failure pressure of high strength pipeline with corrosion defects, Engineering Failure Analysis. 32 (2013) 209–219.

[73] Y. Kim, Y. Lee, W. Kim, K. Oh, The evaluation of failure pressure for corrosion defects within girth or seam weld in transmission pipelines, in: Proceedings of the Intenational Pipeline Conf IPC2004-216, 2004: pp. 1–9.

[74] M. Kamaya, T. Suzuki, T. Meshii, Failure pressure of straight pipe with wall thinning under internal pressure, International Journal of Pressure Vessels and Piping. 85 (2008) 628–634. doi:10.1016/j.ijpvp.2007.11.005.

[75] M. Kamaya, T. Suzuki, T. Meshii, Normalizing the influence of flaw length on failure pressure of straight pipe with wall-thinning, Nuclear Engineering and Design. 238 (2008) 8–15.

[76] J.B. Choi, B.K. Goo, J.C. Kim, Y.J. Kim, W.S. Kim, Development of limit load solutions for corroded gas pipelines, International Journal of Pressure Vessels and Piping. 80 (2003) 121–128.

[77] J. Kiefner, A. Duffy, Summary of research to determine the strength of corroded areas in line pipe, Public Hearing, US Dept of Transportation. (1971).

[78] M. Ahammed, Prediction of remaining strength of corroded pressurised pipelines, International Journal of Pressure Vessels & Piping. (1997) 213–217.

[79] M.S.G. Chiodo, C. Ruggieri, Failure assessments of corroded pipelines with axial defects using stress-based criteria: Numerical studies and verification analyses, International Journal of Pressure Vessels and Piping. 86 (2009) 164–176.

[80] B. Ma, J. Shuai, J. Wang, K. Han, Analysis on the latest assessment criteria of ASME B31G-2009 for the remaining strength of corroded pipelines, Journal of Failure Analysis and Prevention. 11 (2011) 666–671.

[81] K. Zarrabi, Plastic collapse pressures for defected cylindrical vessels, International Journal of Pressure Vessels & Piping. 60 (1994) 65–69.

[82] T.A. DePadova, J.R. Sims, Fitness for Service - Local thin areas comparison of finite

element analysis to physical test results, Fitness-for-Service and Decisions for Petroleum and Chemical Equipment, ASME PVP. 315 (1995).

[83] J. Kim, Y. Kim, B. Kang, S. Hwang, Finite element analysis for bursting failure prediction in bulge forming of a seamed tube, Finite Elements in Analysis and Design. 40 (2004) 953–966.

[84] H. Othman, J. Purbolaksono, B. Ahmad, Failure investigation on deformed superheater tubes, Engineering Failure Analysis. 16 (2009) 329–339.

[85] G. Dini, S. Mahmoud, M. Vaghefi, M. Lotfiani, Computational and experimental failure analysis of continuous-annealing furnace radiant tubes exposed to excessive temperature, Engineering Failure Analysis. 15 (2008) 445–457.

[86] J. Purbolaksono, J. Ahmad, A. Khinani, A.A. Ali, A.Z. Rashid, Failure case studies of SA213-T22 steel tubes of boiler through computer simulations, Journal of Loss Prevention in the Process Industries. 23 (2010) 98–105.

[87] J. Purbolaksono, Y.W. Hong, S.S.M. Nor, H. Othman, B. Ahmad, Evaluation on reheater tube failure, Engineering Failure Analysis. 16 (2009) 533–537.

[88] T.L. Anderson, D.A. Osage, API 579: A comprehensive fitness-for-service guide, International Journal of Pressure Vessels and Piping. 77 (2000) 953–963.

[89] American Petroleum Institute (API), API 579 Recommended practice for Fitness-For-Service, 2000.

[90] American Petroleum Institute (API) and the American Society of Mechanical Engineers (ASME), API 579-1/ASME Fitness-For-Service (API 579 Second Edition), (2007).

[91] American Petroleum Institute (API) and the American Society of Mechanical Engineers (ASME), Fitness-For-Service Example Problem Manual, API 579-2/ASME FFS-2, 2009.

[92] MathWorks, Matlab 2015a 8.5 Version, (2015).

[93] M. Hindley, I. Kalu, H. Inglis, S. Kok, Finite element analysis of boiler tubes under localized thinning, in: Presented at the 10th South African Conference on Computation and Applied Mechanics (SACAM) on 3rd October, 2016 in Northwest University, Potchefstroom, South Africa., 2016.

[94] ANSYS® 2019 R2 Academic Research Version, (2019).

[95] H. Koboyashi, T. Ogawa, Evaluation of corroded and artificially flawed vessels, in: High Presssure Technology at the Dawn of the New Millenium ASME PVP-VOL. 418, 2001: pp. 69–75.

[96] D.-J. Shim, Y.-J. Kim, Y.-J. Kim, Reference stress based approach to predict failure strength of pipes with local wall thinning under combined loading, Journal of Pressure Vessel Technology. 127 (2005) 76. doi:10.1115/1.1849228.

[97] J.E. Bringas, Handbook of comparative world steel standards, 3rd Ed., ASTM, 2002.

[98] D. Gandy, Carbon steel handbook, Electric Power Research Institute (EPRI), 2007.

[99] British Standards Institution (BSI), BS 3059: Part 2 British Standard on Steel boiler and superheater tubes, 1990.

[100] British Standards Institution (BSI), Specification for design and manufacture of water-tube steam generating plant (including superheaters, reheaters and steel tube economizers) - BS 1113-1999, British Standards Institution, 2000.

[101] British Standards Institution (BSI), BS-EN-10216-Seamless steel tube for pressure purposes - Part 2, 2002.

[102] American Society of Mechanical Engineers (ASME), ASME Boiler and Pressure Vessel Code, Section II, Part D: Materials Properties, 2015.

[103] Deutsche Normen, DIN-17175 Seamless tubes of heat-resistant steels, 1979.

[104] TPS Technitube, Boiler tubes, furnace tubes and heat exchanger tubes, TPS Technitube Rohrenwerke GMBH. (2017).

[105] American Petroleum Institute (API), API STD 530 Calculation of Heater-Tube Thickness in Petroleum Refineries, 1996.

[106] T.A. Turbak, J.R. Sims, Comparison of local thin area sssessment methodologies, in: Service Experience and Reliability Improvement: Nuclear, Fossil and Petrochemical Plants, ASME-PVP 288, 1994: pp. 307–314.

Appendix A

To formulate the mathematical expression for the flaw width, f_w, the point of intersection on the x-axis of the circle and ellipse need to be determined, the two simultaneous equations below are considered:

For the circle:

$$x^2 + y^2 = r_o^2 \qquad \text{(E 1)}$$

For the ellipse:

$$\frac{x^2}{a^2} + \frac{(y-z)^2}{b^2} = 1 \qquad \text{(E 2)}$$

From E 2,

$$b^2x^2 + a^2(y-z)^2 = a^2b^2 \qquad \text{(E 3)}$$

$$a^2(y-z)^2 = a^2b^2 - b^2x^2 \qquad \text{(E 4)}$$

$$(y-z)^2 = \frac{b^2(a^2-x^2)}{a^2} \qquad \text{(E 5)}$$

$$\mathrm{y} = \frac{\mathrm{b}\sqrt{(\mathrm{a}^2-\mathrm{x}^2)}}{\mathrm{a}} + \mathrm{z} \qquad \text{(E 6)}$$

Substituting E 6 into E 1;

$$x^2 + \left(\frac{b\sqrt{(a^2-x^2)}}{a} + z\right)^2 = r_o^2 \qquad \text{(E 7)}$$

$$x^2 + \frac{b^2}{a^2}(a^2 - x^2) + z^2 + \frac{2bz}{a}\sqrt{(a^2 - x^2)} = r_o^2 \qquad \text{(E 8)}$$

$$\left(1 - \frac{b^2}{a^2}\right)x^2 + b^2 + z^2 + \frac{2bz}{a}\sqrt{(a^2 - x^2)} = r_o^2 \qquad \text{(E 9)}$$

$$\left(1 - \frac{b^2}{a^2}\right)x^2 + b^2 + z^2 - r_o^2 = -\frac{2bz}{a}\sqrt{(a^2 - x^2)} \qquad \text{(E 10)}$$

$$\left(\left(1 - \frac{b^2}{a^2}\right)x^2 + b^2 + z^2 - r_o^2\right)^2 = \left(-\frac{2bz}{a}\sqrt{(a^2 - x^2)}\right)^2 \qquad \text{(E 11)}$$

$$\left(1 - \frac{b^2}{a^2}\right)^2 x^4 + (b^2 + z^2 - r_o^2)^2 + 2\left(1 - \frac{b^2}{a^2}\right)x^2(b^2 + z^2 - r_o^2) = \frac{4b^2z^2}{a^2}(a^2 - x^2) \qquad \text{(E 12)}$$

$$\left(1-\frac{b^2}{a^2}\right)^2 x^4+\left[\frac{4b^2z^2}{a^2}+2\left(1-\frac{b^2}{a^2}\right)(b^2+z^2-r_o^2)\right]x^2+[(b^2+z^2-r_o^2)^2-4b^2z^2]=0 \quad \text{(E 13)}$$

Let $t = x^2$,

$$At^2+Bt+C=0 \quad \text{(E 14)}$$

$$t=\frac{-B\pm\sqrt{(B^2-4AC)}}{2A} \quad \text{(E 15)}$$

$$x=\sqrt{\frac{-B\pm\sqrt{(B^2-4AC)}}{2A}} \quad \text{(E 16)}$$

$$where\ A=\left(1-\frac{b^2}{a^2}\right)^2;\ B=\frac{4b^2z^2}{a^2}+2\left(1-\frac{b^2}{a^2}\right)(b^2+z^2-r_o^2);\ C=(b^2+z^2-r_o^2)^2-b^2z^2$$

Recall,

$$f_w=2x$$

Therefore,

$$f_w=2.\sqrt{\frac{-\frac{4b^2z^2}{a^2}+2\left(1-\frac{b^2}{a^2}\right)(b^2+z^2-r_o^2)\pm\sqrt{\left(\left(\frac{4b^2z^2}{a^2}+2\left(1-\frac{b^2}{a^2}\right)(b^2+z^2-r_o^2)\right)^2-4\left(1-\frac{b^2}{a^2}\right)^2C=(b^2+z^2-r_o^2)^2-4b^2z^2\right)}}{2\left(1-\frac{b^2}{a^2}\right)^2}}$$

Appendix B

Optimization Technique Program

```
clc;clear global
format long g

[xopt,fopt]=fminsearch ('FitPipeFnx', [916.68 894.43 29 21])

H1=xopt(1,1);
R1=xopt(1,2);
a1=xopt(1,3);
b1=xopt(1,4);

z1=H1-R1-b1;     %% For n-flaws
% z1=H1-R1+b1;     %% For u-flaws

Dimensions of Tubes Investigated (one at a time)
D=75; t=7; t_rem=0.5;      % BS 3059 Grade 360 tube_Fly ash erosion
% D=50.8; t=4.4; t_rem=0.3;  % BS 3059 Grade 360 tube_Fly ash erosion
% D=50.8; t=4.4; t_rem=0.17; % BS 3059 Grade 360 tube_Fly ash erosion
% D=47.5; t=5.4; t_rem=1.2;  % SA 210 A1 tube_Fly ash erosion
% D=50.8; t=6.3; t_rem=0.377; % SA 210 A1 tube_Fly ash erosion
% D=63.5; t=6.6; t_rem=0.8;  % BS 3059 Grade 440 tube_Falling Slag
% D=38; t=3.8; t_rem=0.3;    % BS 3059 Grade 440 tube_Fly ash erosion
% D=38; t=3.8; t_rem=0.3;    % BS 3059 Grade 440 tube_Fly ash erosion
% D=63.5; t=6.1; t_rem=0.63; % BS 3059 Grade 440 tube_Soot blower erosion
% D=63; t=5.4; t_rem=0.42;   % BS 3059 Grade 440 tube_Fly ash erosion
% D=38; t=3.8; t_rem=0.45;   % BS 3059 Grade 440 tube_Fly ash erosion
% D=33; t=3.6; t_rem=0.2;    % 15 Mo3 tube_Soot blower erosion
% D=44.5; t=5.6; t_rem=0.41; % 15 Mo3 tube_Soot blower erosion
% D=33.9; t=6.5; t_rem=0.24; % 15 Mo3 tube_Fly ash erosion
% D=44.5; t=5.2; t_rem=0.5;  % 15 Mo3 tube_Fly ash erosion
% D=34.9; t=4.2; t_rem=0.2;  % BS 3059 620 tube_Fly ash erosion


f_D=t-t_rem;
A1 = (1-(b1.^2./a1.^2)).^2;
B1 = ((4.*b1.^2.*z1.^2)./a1.^2)+(2.*(z1.^2+b1.^2-(D/2).^2).*(1-
(b1.^2./a1.^2)));
C1 = (z1.^2+b1.^2-(D/2).^2).^2 - 4*b1.^2.*z1.^2;

Width = 2*sqrt((-B1-(sqrt(B1.^2-4*A1.*C1)))./(2.*A1))   % Width of the n-
shaped flaw

% Width = 2*sqrt((-B1+(sqrt(B1.^2-4*A1.*C1)))./(2.*A1))   % Width of the u-
shaped flaw

Length = 2*sqrt((2*R1.*f_D)-((f_D).^2))                % Length of the
flaw (NB:Same for both n-and u-shaped flaws)

% Construction of ellipse_circle geometric plots (front view of the tube)
r=D/2;                       % Outer radius of tube
r2=D/2-t;                    % Inner radius of tube
th = linspace(0,2*pi);       % linspace for angles for circle
th2 = linspace(0,pi,50);     % linspace for angles for ellipse
xunit = r * cos(th);      % x coords for points on outer circle
yunit = r * sin(th);      % y coords for points on outer circle
xunit2 = r2 * cos(th);    % x coords for points on inner circle
yunit2 = r2 * sin(th);    % y coords for points on inner circle
```

```
figure(111);
subplot(211)
hold on
plot(xunit, yunit,'k', xunit2, yunit2,'k');
axis equal;
hold on
ellxunit = a1*cos(th2);
ellyunit = b1*sin(th2) + z1;        % For n-flaws
% ellyunit = -b1*sin(th2) + z1;      % For u-flaws
plot(ellxunit, ellyunit,'b', 'linewidth',2);
% axis([-50 50 -100 100])
axis auto;
xlabel('a-axis','FontSize',20)
ylabel('b-axis','FontSize',20)
set(gca,'FontSize',14)
grid on
box on

% Construction of rectangle-circle geometric plots (side view of the tube)
l=1200;                                        % Length of tube
pos=[-l/2 -r l D];
figure(111)
subplot(212)
rectangle('Position',pos)
hold on
pos1=[-l/2 -r2 l, D-(2*t)];
rectangle('Position',pos1,'LineStyle','--')
axis equal
Dp=H1-R1;
Dp_com=f_D+Dp;
th=linspace(0,pi,50);
xunit = Length*cos(th);
yunit = -f_D*sin(th)+Dp_com;
plot(xunit,yunit,'b', 'linewidth',2);
xlabel('Tube Length','FontSize',20)
ylabel('Tube Diameter','FontSize',20)
set(gca,'FontSize',14)
grid on
hold off
```

Fit Pipe Function

```
function[Error]=FitPipeFnx(x)
H=x(1);
R=x(2);
a=x(3);
b=x(4);

% Dimensions of Tubes Investigated (one at a time)
D=75; t=7; t_rem=0.5; fl=600; fw=20; % BS 3059 Grade 360 tube_Fly ash
erosion
% D=50.8; t=4.4; t_rem=0.3; fl=80; fw=25; % BS 3059 Grade 360 tube_Fly ash
erosion
% D=50.8; t=4.4; t_rem=0.17; fl=70; fw=40; % BS 3059 Grade 360 tube_Fly
ash erosion
% D=47.5; t=5.4; t_rem=1.2; fl=400; fw=45; % SA 210 A1 tube_Fly ash
erosion
% D=50.8; t=6.3; t_rem=0.377; fl=150; fw=50; % SA 210 A1 tube_Fly ash
erosion
```

```
% D=63.5; t=6.6; t_rem=0.8; fl=240; fw=30; % BS 3059 Grade 440
tube_Falling Slag
% D=38; t=3.8; t_rem=0.3; fl=110; fw=28;    % BS 3059 Grade 440 tube_Fly
ash erosion
% D=38; t=3.8; t_rem=0.3; fl=155; fw=32;    % BS 3059 Grade 440 tube_Fly
ash erosion
% D=63.5; t=6.1; t_rem=0.63; fl=600; fw=50; % BS 3059 Grade 440 tube_Soot
blower erosion
% D=63; t=5.4; t_rem=0.42; fl=310; fw=60;   % BS 3059 Grade 440 tube_Fly
ash erosion
% D=38; t=3.8; t_rem=0.45; fl=500; fw=35;   % BS 3059 Grade 440 tube_Fly
ash erosion
% D=33; t=3.6; t_rem=0.2; fl=20; fw=15;    % 15 Mo3 tube_Soot blower
erosion
% D=44.5; t=5.6; t_rem=0.41; fl=225; fw=35; % 15 Mo3 tube_Soot blower
erosion
% D=33.9; t=6.5; t_rem=0.24; fl=300; fw=30; % 15 Mo3 tube_Fly ash erosion
% D=44.5; t=5.2; t_rem=0.5; fl=140; fw=44; % 15 Mo3 tube_Fly ash erosion
% D=34.9; t=4.2; t_rem=0.2; fl=300; fw=30; % BS 3059 620 tube_Fly ash
erosion

%%% For the n-shaped FEM
% R = H-(z+b);                % Sweeping Radius
F_D = (D/2)-(H-R);            % Flaw Depth
% F_D = (D/2)-(z+b);          % Flaw Depth

z=H-R-b;
A = (1-(b.^2./a.^2)).^2;
B = ((4.*b.^2.*z.^2)./a.^2)+(2.*(z.^2+b.^2-(D/2).^2).*(1-(b.^2./a.^2)));
C = (z.^2+b.^2-(D/2).^2).^2 - 4*b.^2.*z.^2;
F_W_n = 2*sqrt((-B-(sqrt(B.^2-4*A.*C)))./(2.*A));       % Width of the n-
shaped flaw

F_L = 2*sqrt((2*R.*F_D)-((F_D).^2));                     % Length of the
flaw (NB:Same for both n-and u-shaped flaws)

%%% For the u-shaped FEM
% R = H-(z-b);                 % Sweeping Radius
% F_D = (D/2)-(H-R);           % Flaw Depth
% % F_D = (D/2)-(z-b);         % Flaw Depth

% z=H-R+b;
% A2 =  (1-(b.^2./a.^2)).^2;
% B2 = ((4.*b.^2.*z.^2)./a.^2)+(2.*(z.^2+b.^2-(D/2).^2).*(1-
(b.^2./a.^2)));
% C2 = (z.^2+b.^2-(D/2).^2).^2 - 4*b.^2.*z.^2;
% F_W_u = 2*sqrt((-B2+(sqrt(B2.^2-4*A2.*C2)))./(2.*A2));  % Width of the
u-shaped flaw

Error=(F_L-fl).^2+(F_W_n-fw).^2+(F_D-(t-t_rem)).^2;      %% n-flaw
% Error=(F_L-fl).^2+(F_W_u-fw).^2+(F_D-(t-t_rem)).^2;      %% u-flaw
End
```

Appendix C

Coefficient values obtained from the FFS Standard used for the Second Approach computation of the minimum specific yield strength (*MSYS*) values for different steel grades

For Carbon steels (having yield strength <275.9 MPa), which applies for Carbon and Medium Carbon Steels as described in this paper, the coefficient values to be used are as follows:

T (Min) °C	T (Max) °C	C_0	C_1	C_2	C_3	C_4	C_5
21	593	3.79335351E-2	-1.86385965E-3	6.69470079E-6	-1.82518378E-8	2.31521177E-11	-1.22947065E-14

For Steel type with C-1/2Mo (Carbon-Molybdenum Alloy Steel), the coefficient values to be used are as follows:

T (Min) °C	T (Max) °C	C_0	C_1	C_2	C_3	C_4	C_5
21	593	3.38037095E-2	-1.73554380E-3	8.32638097E-6	-2.11471664E-8	3.29874954E-11	-2.69329508E-14

For Steel type with 1-1/4Cr-1/2Mo (Chromium-Molybdenum Alloy Steel), the coefficient values to be used are as follows:

T (Min) °C	T (Max) °C	C_0	C_1	C_2	C_3	C_4	C_5
21	593	4.38110535E-2	-2.17153985E-3	1.21747825E-5	-3.89315704E-8	6.43532344E-11	-4.71714972E-14

Appendix D

Coefficient values obtained from the FFS Standard used for the Second Approach computation of the minimum specific ultimate tensile strength (*MSUTS*) values for different steel grades.

For Carbon steels (having yield strength <275.9 MPa), which applies for Carbon and Medium Carbon Steels as described in this paper, the coefficient values to be used are as follows:

T (Min) ℃	T (Max) ℃	C_0	C_1	C_2	C_3	C_4	C_5
21	593	3.55835868E-2	-8.87531986E-4	-4.52108819E-6	4.67964163E-8	-1.07882077E-10	6.38793289E-14

For Steel type with C-1/2Mo (Carbon-Molybdenum Alloy Steel), the coefficient values to be used are as follows:

T (Min) ℃	T (Max) ℃	C_0	C_1	C_2	C_3	C_4	C_5
21	593	5.63401650E-2	-2.54673855E-3	4.83029306E-6	1.40154694E-8	-3.85657189E-11	1.47716803E-14

For Steel type with 1-1/4Cr-1/2Mo (Chromium-Molybdenum Alloy Steel), the coefficient values to be used are as follows:

T (Min) ℃	T (Max) ℃	C_0	C_1	C_2	C_3	C_4	C_5
21	593	3.35950169E-2	-1.59542267E-3	4.19028077E-6	3.21310030E-9	-2.14741795E-11	9.85350689E-15

Appendix E

Table of values from API STD 530 used for the Third Approach computation of the minimum yield and tensile strengths as documented in the FFS Standard.

Steel Type	Temperature Limits and Strength Values at the given Minimum Temperature	For Computing Yield Strength (MPa), σ_y		For Computing Tensile Strength (MPa), σ_{uts}	
Carbon Steel (Figure 4A in API STD 530) A 161 A192	$T_{min} = 149$°C $T_{max} = 621$°C $\sigma_y^{T_{min}} = 157$ MPa $\sigma_{uts}^{T_{min}} = 298$ MPa	A_0	1.6251089	B_0	1.1720989
		A_1	-3.3124966E-3	B_1	-2.0580032E-3
		A_2	5.0904910E-6	B_2	7.6239020E-6
		A_3	-3.3374441E-9	B_3	-9.9459690E-9
		A_4	4.9690402E-13	B_4	3.7189699E-12
		A_5	0	B_5	0
Medium Carbon Steel (Figure 4B in API STD 530) A 53 Gr. B A 106 Gr. B A 210 Gr. A1	$T_{min} = 149$°C $T_{max} = 621$°C $\sigma_y^{T_{min}} = 210$ MPa $\sigma_{uts}^{T_{min}} = 379$ MPa	A_0	1.6434698	B_0	1.1872106
		A_1	-3.5201715E-3	B_1	-2.2083065E-3
		A_2	5.8080277E-6	B_2	8.0934859E-6
		A_3	-4.2398160E-9	B_3	-1.0510434E-8
		A_4	8.7536764E-13	B_4	3.9529036E-12
		A_5	0	B_5	0
C-0.5Mo (Figure 4C in API STD 530) A 161 Gr. T1 A 209 Gr. T1 A 335 Gr. P1	$T_{min} = 149$°C $T_{max} = 621$°C $\sigma_y^{T_{min}} = 186$ MPa $\sigma_{uts}^{T_{min}} = 395$ MPa	A_0	1.0875314	B_0	-8.3107781E-2
		A_1	-2.1270293E-4	B_1	6.7591546E-3
		A_2	-4.4780776E-7	B_2	-1.3556423E-5
		A_3	8.4688943E-10	B_3	1.1122871E-8
		A_4	-5.6614129E-13	B_4	-3.5429684E-12
		A_5	0	B_5	0
1.25Cr-0.5Mo (Figure 4D in API STD 530) A 213 Gr. T11 A 335 Gr. P11 A 200 Gr. T11	$T_{min} = 149$°C $T_{max} = 621$°C $\sigma_y^{T_{min}} = 183$ MPa $\sigma_{uts}^{T_{min}} = 379$ MPa	A_0	1.1345901	B_0	1.7526113
		A_1	-4.8648764E-4	B_1	-7.0066393E-3
		A_2	3.9401132E-8	B_2	2.3037863E-5
		A_3	4.2209296E-10	B_3	-3.2685799E-8
		A_4	-3.8709072E-13	B_4	2.0963053E-11
		A_5	0	B_5	-5.2442438E-15

Appendix F

The Material Properties Council (MPC) stress-strain curve model used to produce a true stress-strain hardening curve for the simulation is described as follows:

$$\varepsilon_t = \frac{\sigma_t}{E} + \gamma_1 + \gamma_2 \tag{D 1}$$

where, ε_t is the total true strain (elastic plus plastic); E is the Young's modulus; σ_t is the true stress

$$\gamma_1 = \frac{\varepsilon_1}{2}(1 - tanh[H]) \tag{D 2}$$

$$\gamma_2 = \frac{\varepsilon_2}{2}(1 + tanh[H]) \tag{D 3}$$

$$\varepsilon_1 = \left(\frac{\sigma_t}{A_1}\right)^{\frac{1}{m_1}} \tag{D 4}$$

$$A_1 = \frac{\sigma_y(1+\varepsilon_y)}{(ln[1+\varepsilon_y])^{m_1}} \tag{D 5}$$

$$m_1 = \frac{ln[R_o]+(\varepsilon_p+\varepsilon_y)}{\left(ln\left[\frac{ln[1+\varepsilon_p]}{ln[1+\varepsilon_y]}\right]\right)} \tag{D 6}$$

$$\varepsilon_2 = \left(\frac{\sigma_t}{A_2}\right)^{\frac{1}{m_2}} \tag{D 7}$$

$$A_2 = \frac{\sigma_{uts} exp[m_2]}{{m_2}^{m_2}} \tag{D 8}$$

$$H_o = \frac{2[\sigma_t-(\sigma_y+K\{\sigma_{uts}-\sigma_y\})]}{K(\sigma_{uts}-\sigma_y)} \tag{D 9}$$

$$R_o = \frac{\sigma_y}{\sigma_{uts}} \tag{D 10}$$

$$\varepsilon_y = 0.002 \tag{D 11}$$

$$K = 1.5{R_o}^{1.5} - 0.5{R_o}^{2.5} - {R_o}^{3.5} \tag{D 12}$$

Where γ_1 is the true strain in the micro-strain region of the stress-strain curve

γ_2 is the true strain in the macro-strain region of the stress-strain curve

ε_1 is the true plastic strain in the micro-strain region of the stress-strain curve

ε_2 is the true plastic strain in the macro-strain region of the stress-strain curve

ε_p is the stress-strain curve fitting parameter

ε_y is the 0.2% engineering offset strain

R_o is the ratio of the engineering yield stress to the engineering tensile stress

A_1 is the curve fitting constant for the elastic region of the stress-strain curve

A_2 is the curve fitting constant for the plastic region of the stress-strain curve

m_1 is the curve fitting exponent for the stress-strain curve equal to the true strain at the proportional limit and the strain hardening coefficient in the large strain region

m_2 is the curve fitting exponent for the stress-strain curve equal to the true strain at the true ultimate stress

H_o is the stress-strain curve fitting parameter

σ_y is the yield stress at temperature of interest

σ_{uts} is the engineering ultimate tensile stress at temperature of interest

K is the material parameter for the stress-strain curve model

σ_t is to be evaluated using:

$$\sigma_t = (1 + \varepsilon)\sigma \qquad \text{(D 13)}$$

Where ε is the engineering strain and σ is the engineering stress

The values of m_2 and ε_p are obtained from the FFS standard. For ferritic steel (which the heat resistant steels studied in this work fall under), at temperature limit of 480^oC, these are given as:

$$m_2 = 0.60(1 - R_o) \qquad \text{(D 14)}$$

$$\varepsilon_p = 2.0E - 5 \qquad \text{(D 15)}$$

Appendix G

Parameterized models with remaining tube thicknesses evenly divided from initial t_r to t_{min} for each tube used for the study.

Group	Tubes	Tube remaining thicknesses (mm)		H (mm)	R (mm)	a (mm)	b (mm)
*1.	BS 3059 Grade 360	Initial t_r	0.50	6957.333	6926.333	30.013	89.990
	BS 3059 Grade 360	t_{r_2}	0.69	7165.882	7134.692	40.806	162.400
	BS 3059 Grade 360	t_{r_3}	0.87	7375.141	7343.771	44.935	190.290
	BS 3059 Grade 360	t_{r_4}	1.06	7610.333	7578.773	35.096	110.535
	BS 3059 Grade 360	t_{r_5}	1.24	7847.040	7815.300	40.138	139.600
	BS 3059 Grade 360	t_{r_6}	1.43	8113.680	8081.750	35.095	101.603
	BS 3059 Grade 360	t_{r_7}	1.61	8383.600	8351.490	30.035	70.669
	BS 3059 Grade 360	t_{r_8}	1.98	8999.133	8966.653	38.944	109.216
	BS 3059 Grade 360	t_{r_9}	3.66	13508.883	13474.723	60.927	146.145
	BS 3059 Grade 360	t_{min}	5.34	27145.103	27109.263	169.450	173.248
*2.	BS 3059 Grade 360	Initial t_r	0.30	218.477	197.177	105.101	114.305
	BS 3059 Grade 360	t_{r_2}	0.43	224.935	203.505	120.025	125.289
	BS 3059 Grade 360	t_{r_3}	0.56	231.811	210.251	145.510	149.130
	BS 3059 Grade 360	t_{r_4}	0.69	239.178	217.488	189.946	194.358
	BS 3059 Grade 360	t_{r_5}	0.82	247.077	225.257	190.580	135.285
	BS 3059 Grade 360	t_{r_6}	0.95	255.566	233.616	334.379	230.778
	BS 3059 Grade 360	t_{r_7}	1.08	264.704	242.624	740.554	219.769
	+BS 3059 Grade 360	t_{r_8}	1.34	285.31	262.970	57.912	9.702
	+BS 3059 Grade 360	t_{r_9}	2.39	422.404	399.014	25.548	10.000
	+BS 3059 Grade 360	t_{min}	3.43	849.657	825.227	24.105	15.995
3.	BS 3059 Grade 360	Initial t_r	0.17	168.088	146.911	25.191	14.062
	BS 3059 Grade 360	t_{r_2}	0.29	172.372	151.082	25.637	15.045
	BS 3059 Grade 360	t_{r_3}	0.41	176.914	155.504	25.376	14.961
	BS 3059 Grade 360	t_{r_4}	0.53	181.730	160.200	25.145	14.909
	BS 3059 Grade 360	t_{r_5}	0.74	190.920	169.180	25.151	15.451
	BS 3059 Grade 360	t_{r_6}	0.88	197.650	175.770	25.011	15.574
	BS 3059 Grade 360	t_{r_7}	1.02	204.937	182.917	25.478	16.722
	BS 3059 Grade 360	t_{r_8}	1.30	221.430	199.130	25.153	16.877
	BS 3059 Grade 360	t_{r_9}	2.32	318.831	295.511	25.258	19.685
	BS 3059 Grade 360	t_{min}	3.33	597.294	572.964	25.473	22.781
4.	SA 210 A1	Initial t_r	1.20	4783.560	4764.010	24.339	19.308
	SA 210 A1	t_{r_2}	1.28	4876.052	4856.422	24.355	19.485
	SA 210 A1	t_{r_3}	1.36	4972.222	4952.512	24.319	19.510
	SA 210 A1	t_{r_4}	1.44	5072.277	5052.487	24.275	19.509
	SA 210 A1	t_{r_5}	1.51	5163.199	5143.339	24.244	19.530
	SA 210 A1	t_{r_6}	1.59	5271.180	5251.240	24.208	19.550
	SA 210 A1	t_{r_7}	1.67	5383.810	5363.790	24.238	19.767
	SA 210 A1	t_{r_8}	1.82	5608.555	5588.385	24.264	20.085
	SA 210 A1	t_{r_9}	3.27	9412.356	9390.736	24.018	21.649
	SA 210 A1	t_{min}	4.71	29008.912	28985.852	23.827	23.071
5.	SA 210 A1	Initial t_r	0.377	497.282	477.805	25.692	19.475
	SA 210 A1	t_{r_2}	0.53	509.955	490.325	25.602	19.842

	SA 210 A1	t_{r_3}	0.68	523.035	503.255	25.669	19.773
	SA 210 A1	t_{r_4}	0.87	540.644	520.674	25.655	19.961
	SA 210 A1	t_{r_5}	1.06	559.522	539.362	25.641	20.146
	SA 210 A1	t_{r_6}	1.23	577.600	557.270	25.569	20.518
	SA 210 A1	t_{r_7}	1.40	596.933	576.433	25.622	20.496
	SA 210 A1	t_{r_8}	1.74	639.900	619.060	25.601	20.839
	SA 210 A1	t_{r_9}	3.15	916.682	894.432	25.524	22.245
	SA 210 A1	t_{min}	4.27	1409.852	1386.482	25.474	23.372
*6.	BS 3059 Grade 440	Initial t_r	0.80	1270.222	1244.272	65.505	76.520
	BS 3059 Grade 440	t_{r_2}	1.05	1326.300	1300.100	70.027	76.827
	BS 3059 Grade 440	t_{r_3}	1.29	1385.030	1358.590	101.015	139.202
	BS 3059 Grade 440	t_{r_4}	1.54	1452.145	1425.455	116.735	156.002
	BS 3059 Grade 440	t_{r_5}	1.78	1523.116	1496.186	135.675	171.809
	BS 3059 Grade 440	t_{r_6}	2.03	1604.957	1577.777	150.673	161.694
	BS 3059 Grade 440	t_{r_7}	2.27	1692.400	1664.980	218.230	238.160
	BS 3059 Grade 440	t_{r_8}	2.75	1900.000	1872.100	390.189	112.627
	+BS 3059 Grade 440	t_{r_9}	4.30	3161.034	3131.584	44.804	25.415
	+BS 3059 Grade 440	t_{min}	5.85	9631.375	9600.375	32.761	27.184
7.	BS 3059 Grade 440	Initial t_r	0.30	449.399	433.899	20.283	9.604
	BS 3059 Grade 440	t_{r_2}	0.47	471.555	455.885	20.997	11.089
	BS 3059 Grade 440	t_{r_3}	0.64	496.055	480.215	20.418	11.007
	BS 3059 Grade 440	t_{r_4}	0.81	523.355	507.345	19.981	11.046
	BS 3059 Grade 440	t_{r_5}	0.97	552.030	535.860	19.549	11.007
	BS 3059 Grade 440	t_{r_6}	1.14	586.258	569.918	19.155	11.007
	BS 3059 Grade 440	t_{r_7}	1.30	622.766	606.266	19.003	11.287
	BS 3059 Grade 440	t_{r_8}	1.63	714.922	698.092	20.627	15.003
	BS 3059 Grade 440	t_{r_9}	2.50	1181.811	1164.111	19.515	16.005
	BS 3059 Grade 440	t_{min}	3.36	3456.282	3437.722	19.373	18.504
8.	BS 3059 Grade 440	Initial t_r	0.30	875.290	859.790	18.336	10.269
	BS 3059 Grade 440	t_{r_2}	0.47	919.160	903.490	20.791	15.004
	BS 3059 Grade 440	t_{r_3}	0.64	967.777	951.937	20.543	15.0025
	BS 3059 Grade 440	t_{r_4}	0.81	1021.907	1005.897	20.311	15.007
	BS 3059 Grade 440	t_{r_5}	0.97	1078.785	1062.615	20.075	14.956
	BS 3059 Grade 440	t_{r_6}	1.14	1146.633	1130.293	20.068	15.371
	BS 3059 Grade 440	t_{r_7}	1.30	1219.000	1202.500	20	15.632
	BS 3059 Grade 440	t_{r_8}	1.63	1401.840	1385.010	19.855	16.1405
	BS 3059 Grade 440	t_{r_9}	2.50	2328.446	2310.746	19.223	16.721
	BS 3059 Grade 440	t_{min}	3.36	6844.064	6825.504	19.031	18.129
9.	BS 3059 Grade 440	Initial t_r	0.63	8255.710	8229.430	32.090	17.982
	BS 3059 Grade 440	t_{r_2}	0.75	8440.330	8413.930	31.524	17.470
	BS 3059 Grade 440	t_{r_3}	0.87	8633.283	8606.763	29.969	15.491
	BS 3059 Grade 440	t_{r_4}	0.99	8835.399	8808.759	29.969	15.758
	BS 3059 Grade 440	t_{r_5}	1.10	9029.275	9002.525	30.060	16.140
	BS 3059 Grade 440	t_{r_6}	1.22	9250.681	9223.811	30.120	16.502
	BS 3059 Grade 440	t_{r_7}	1.34	9483.205	9456.215	30.011	16.604
	BS 3059 Grade 440	t_{r_8}	1.57	9963.253	9936.033	31.939	20.251
	BS 3059 Grade 440	t_{r_9}	2.44	12325.001	12296.911	31.148	21.110

	BS 3059 Grade 440	t_{min}	3.30	16101.778	16072.828	31.496	23.938
10.	BS 3059 Grade 440	Initial t_r	0.42	2441.160	2414.640	32.179	26.529
	BS 3059 Grade 440	t_{r_2}	0.55	2505.883	2479.233	32.082	26.769
	BS 3059 Grade 440	t_{r_3}	0.68	2574.168	2547.388	32.043	26.925
	BS 3059 Grade 440	t_{r_4}	0.81	2646.307	2619.397	32.025	27.049
	BS 3059 Grade 440	t_{r_5}	0.93	2716.625	2689.595	32.006	27.168
	BS 3059 Grade 440	t_{r_6}	1.06	2797.187	2770.027	32.058	27.182
	BS 3059 Grade 440	t_{r_7}	1.19	2882.722	2855.432	31.884	27.561
	BS 3059 Grade 440	t_{r_8}	1.44	3062.973	3035.433	31.980	27.588
	BS 3059 Grade 440	t_{r_9}	2.30	3904.955	3876.555	31.871	28.413
	BS 3059 Grade 440	t_{min}	3.16	5393.103	5363.843	31.756	29.267
11.	BS 3059 Grade 440	Initial t_r	0.45	9345.680	9330.030	19.193	14.000
	BS 3059 Grade 440	t_{r_2}	0.59	9752.580	9736.790	19.506	15.029
	BS 3059 Grade 440	t_{r_3}	0.73	10196.861	10180.931	19.485	15.2265
	BS 3059 Grade 440	t_{r_4}	0.87	10683.384	10667.314	19.463	15.4185
	BS 3059 Grade 440	t_{r_5}	1.01	11217.530	11201.320	19.357	15.387
	BS 3059 Grade 440	t_{r_6}	1.15	11811.245	11794.895	19.247	15.335
	BS 3059 Grade 440	t_{r_7}	1.29	12467.944	12451.454	19.198	15.439
	BS 3059 Grade 440	t_{r_8}	1.55	13906.760	13890.010	19.218	15.937
	BS 3059 Grade 440	t_{r_9}	2.10	18400.502	18383.202	19.140	16.640
	BS 3059 Grade 440	t_{min}	2.64	26958.075	26940.235	19.229	17.830
*12.	DIN 17175 15Mo3	Initial t_r	0.20	29.506	16.406	10.789	14.325
	DIN 17175 15Mo3	t_{r_2}	0.34	30.207	16.967	10.613	14.8315
	DIN 17175 15Mo3	t_{r_3}	0.47	30.909	17.539	10.054	15.105
	DIN 17175 15Mo3	t_{r_4}	0.61	31.727	18.217	9.915	15.808
	DIN 17175 15Mo3	t_{r_5}	0.74	32.553	18.913	9.731	16.547
	DIN 17175 15Mo3	t_{r_6}	0.88	33.522	19.742	9.061	17.1095
	DIN 17175 15Mo3	t_{r_7}	1.01	34.512	20.600	8.814	18.1585
	DIN 17175 15Mo3	t_{r_8}	1.28	36.892	22.712	7.242	20.214
	+DIN 17175 15Mo3	t_{r_9}	2.00	46.950	32.050	37.364	9.977
	+DIN 17175 15Mo3	t_{min}	2.72	72.878	57.258	18.013	10.165
13.	DIN 17175 15Mo3	Initial t_r	0.41	1238.950	1221.890	25.593	12.279
	DIN 17175 15Mo3	t_{r_2}	0.58	1280.320	1263.090	24.706	11.863
	DIN 17175 15Mo3	t_{r_3}	0.76	1327.294	1309.884	25.165	13.039
	DIN 17175 15Mo3	t_{r_4}	0.94	1377.870	1360.280	26.156	14.989
	DIN 17175 15Mo3	t_{r_5}	1.11	1429.357	1411.597	25.730	15.057
	DIN 17175 15Mo3	t_{r_6}	1.28	1484.830	1466.900	25.270	15.035
	DIN 17175 15Mo3	t_{r_7}	1.46	1548.678	1530.568	24.987	15.264
	DIN 17175 15Mo3	t_{r_8}	1.80	1685.640	1667.190	24.649	15.921
	DIN 17175 15Mo3	t_{r_9}	2.77	2256.921	2237.501	23.586	17.232
	DIN 17175 15Mo3	t_{min}	3.74	3423.537	3403.147	22.812	18.546
14.	DIN 17175 15Mo3	Initial t_r	0.24	1810.950	1800.260	22.227	10.672
	DIN 17175 15Mo3	t_{r_2}	0.36	1846.058	1835.248	21.172	9.912
	DIN 17175 15Mo3	t_{r_3}	0.48	1882.680	1871.750	20.914	10.016
	DIN 17175 15Mo3	t_{r_4}	0.61	1924.020	1912.960	20.580	10.042
	DIN 17175 15Mo3	t_{r_5}	0.73	1963.805	1952.625	18.624	8.071
	DIN 17175 15Mo3	t_{r_6}	0.85	2005.275	1993.975	19.593	9.552

	DIN 17175 15Mo3	t_{r_7}	0.98	2052.233	2040.803	20.445	11.036
	DIN 17175 15Mo3	t_{r_8}	1.22	2144.990	2133.320	18.926	9.6775
	DIN 17175 15Mo3	t_{r_9}	1.91	2465.635	2453.275	18.106	10.153
	DIN 17175 15Mo3	t_{min}	2.60	2899.615	2886.565	18.560	12.544
15.	DIN 17175 15Mo3	Initial t_r	0.50	541.180	523.630	22.403	17.561
	DIN 17175 15Mo3	t_{r_2}	0.64	557.256	539.566	22.378	17.766
	DIN 17175 15Mo3	t_{r_3}	0.77	573.088	555.268	22.363	17.929
	DIN 17175 15Mo3	t_{r_4}	0.91	591.204	573.244	22.365	18.041
	DIN 17175 15Mo3	t_{r_5}	1.04	609.111	591.021	22.378	18.102
	DIN 17175 15Mo3	t_{r_6}	1.18	629.699	611.469	22.371	18.249
	DIN 17175 15Mo3	t_{r_7}	1.32	651.750	633.380	22.364	18.391
	DIN 17175 15Mo3	t_{r_8}	1.57	695.360	676.740	22.360	18.620
	DIN 17175 15Mo3	t_{r_9}	2.46	915.040	895.530	22.326	19.505
	DIN 17175 15Mo3	t_{min}	2.80	1041.883	1022.033	22.315	19.847
16.	BS 3059 Grade 620	Initial t_r	0.20	2827.950	2814.500	18.623	11.129
	BS 3059 Grade 620	t_{r_2}	0.32	2914.990	2901.420	19.871	11.129
	BS 3059 Grade 620	t_{r_3}	0.45	3015.590	3001.890	19.032	13.580
	BS 3059 Grade 620	t_{r_4}	0.57	3114.790	3100.970	19.155	14.000
	BS 3059 Grade 620	t_{r_5}	0.69	3220.830	3206.890	19.307	14.018
	BS 3059 Grade 620	t_{r_6}	0.81	3334.320	3320.260	19.123	14.026
	BS 3059 Grade 620	t_{r_7}	0.93	3456.200	3442.020	18.653	13.545
	BS 3059 Grade 620	t_{r_8}	1.17	3728.800	3714.380	18.360	12.979
	BS 3059 Grade 620	t_{r_9}	1.44	4092.150	4077.460	18.039	12.999
	BS 3059 Grade 620	t_{min}	1.71	4534.277	4519.317	18.211	12.988

*These are the u-shaped flawed tubes, while others are the n-shaped flawed tubes

+These u-shaped flawed tubes initially had n-shaped geometry from t_{min} to the marked t_{rs} but later transitioned to a u-shaped configuration for the other unmarked t_{rs}.